SPATIAL CURRENT STRUCTURE OBSERVED WITH A CALIBRATED HF RADAR SYSTEM: THE INFLUNECE OF LOCAL FORCING, STRATIFICATION, AND TOPOGRAPHY ON THE INNER SHELF

by

JOSHUA TODD KOHUT

A Dissertation submitted to the

Graduate School-New Brunswick

Rutgers, The State University of New Jersey

in partial fulfillment of the requirements

for the degree of

Doctor of Philosophy

Graduate Program in Oceanography

written under the direction of

Scott M. Glenn

and approved by

_____

_____

_____

_____

New Brunswick, New Jersey

October, 2002

ABSTRACT OF THE DISSERTATION

Spatial Current Structure Observed With a

Calibrated HF Radar System:

The Influence of Local Forcing, Stratification, and Topography

on the Inner Shelf

by

JOSHUA TODD KOHUT

Dissertation Director:

Scott M. Glenn

Ocean current variability over the inner shelf is presented here using an HF radar system. The system uses radio waves scattered off the ocean to measure the range, bearing and radial velocity of the scattering surface. For this particular system, the signal bearing is determined using the patterns of three independent antennas. A series of antenna measurements show that these patterns are often distorted when an antenna is deployed in the field. Based on these measured patterns, the local environment is identified as a significant contributor to the distortion. ADCP correlation indicates that data calibrated with the measured pattern are more accurate than the uncalibrated data. It is also shown that the error associated with the distorted patterns is due to incorrect estimates of the bearing toward the scattering surface.

The calibrated spatial time series data of the HF radar system is then applied to the inner-shelf circulation. The hydrographic variability of the inner shelf off New Jersey

is largely bimodal between summer stratification and winter mixing. An annual oceanographic and atmospheric dataset was separated into these two regimes. The influence of stratification is evident through a relatively steady current response strongly correlated with the wind during the stratified season, and a more variable response less correlated with the wind during the mixed season. When the water column is mixed, topography orients the unstratified variability along the coast with spatial structure related to the local topographic slope.

The passing of tropical storm Floyd through the HF radar field offers a unique dataset for characterizing the inner shelf response to shorter time-scale forcing. Prior to the tropical storm, the water column was mixed leading to a barotropic response. This response is rectilinear in the along-shore direction and driven by a sea surface perturbation. This perturbation, setup by the storm surge and cross-shore winds, propagates through the study site, driving an oscillating along-shore response. Bottom friction is shown to quickly dissipate the energy associated with the episodic event.

ACKNOWLEDGEMENTS

The work presented in this dissertation was funded by the Office of Naval Research (N00014-97-1-0797, N00014-99-1-0196, N00014-00-1-0724), the National Ocean Partnership Program (N00014-97-1-1019, N000-14-98-1-0815), and the great state of New Jersey. ADCP data provided by the Mid-Atlantic Bight National Undersea Research Center with additional support from the National Science Foundation.

I would like to thank my committee members Drs. Jeff Paduan, Robert Chant, and Dale Haidvogel for the advice they offered throughout my graduate career. They continually made themselves available for my questions and comments and provided an objective review of my research.

I would also like to acknowledge all the support I had from the Institute of Marine and Coastal Sciences. Especially those in computing services (Charles Belmonte, Rob Sharry, Adam Porter, and John Wiggins), the front office (Laina Borwegen, Susan Keller, and Marge Piechota), and all other faculty and staff who offered their time and advice whenever I needed it.

I would like to thank the staff of the Rutgers University Marine Field Station, especially Rose Petrecca for arranging the boat time necessary for the antenna calibration runs.

I would like to thank my fellow graduate students, especially Trish Bergmann and Matt Oliver for all their continuing advice and support.

I appreciate all of the guidance and hardware support provided by everyone at Codar Ocean Sensors, Ltd., especially Don Barrick, Pete Lilleboe, Belinda Lipa, Laura Pederson, Bill Rector, and Chad Whelen.

I would also like to acknowledge all the support, guidance, and comic relief provided by the members of the Rutgers University Coastal Ocean Observation Lab (R.U.C.O.O.L), especially Kristie Andresen, Louis Bowers, Liz Creed, Mike Crowley, John Fracassi, Clinton "Chip" Haldeman III, Chhaya Mudgal, and Chuck "Sagé" Lichtenwalner.

I would like to acknowledge my advisor and friend, Scott Glenn. Ever since I first met him as an undergraduate he has always made himself available for any questions or comments I have, both related and unrelated to my graduate career. His unselfish advice is always sincere and has provided me with the tools necessary to succeed in oceanographic research. The future success of my career will always be attributed, in part, to Scott.

I could not have successfully completed my graduate work without the amazing support of my family. My mother, father and sister have instilled in me the personal traits and skills necessary to succeed.

My wife Courtney cannot be thanked enough for the sacrifices she has made to support me throughout my research. Without her emotional support I never would have completed the research presented in this dissertation.

TABLE OF CONTENTS

LIST OF TABLES

LIST OF ILLUSTRATIONS

1.0 INTRODUCTION

The coastal ocean is an intricate system that forms the boundary between the land and the deep ocean. This environment consists of tightly linked chemical and biological processes that coexist in a causal relationship with complicated flow dynamics. As the water depth decreases, physical forcing shifts from density gradients to turbulent mixing and frictional forcing along surface, bottom, offshore and inshore boundaries (Robinson and Glenn, 1999). While the deep ocean experiences independent air-ocean and ocean-benthos interactions, the benthos of the shallow ocean affects the surface layer and in turn alters exchange processes with the atmosphere (Geernaert and Larsen, 1998). Since the system is so shallow, surface and bottom boundary layers overlap. According to Brink (1997), "Shelf water deeper than 3 m and shallower than 30 m have often been ignored in the past because of very difficult operating conditions and complex dynamics, where the water is filled with turbulent boundary layers." In this region, surface gravity waves influence bottom roughness through ripple formation and degradation and increase sediment transport through resuspension. Interactions between wave boundary layers and low frequency fluctuations further influence the bottom stress and current shear. In addition, tidal oscillations interacting with low frequency features along the offshore boundary influence cross-shelf exchange with the deep ocean (Magnell et al. 1980). The nearshore boundary is subject to freshwater outflow that produces time-dependent buoyant flows and coastal fronts (Robinson and Glenn, 1999). Wind forcing is critical to coastal ocean flow and can quickly change the dynamics resulting in the generation of large wave disturbances greater than or of the same magnitude as the underlying low frequency current.

The purpose of the Longterm Ecosystem Observatory located in 15m of water (LEO-15) off the New Jersey coast is to monitor long-term trends and capture episodic events within the inner shelf. In a well-sampled ocean, "... experiments are more efficient, since the timing and location of the processes of interest are known" (Glenn et al., 2000a). Using an array of instrumentation, LEO-15 samples the physical, biological and chemical properties of the inner shelf waters off the New Jersey coast. Therefore both episodic and long-term processes are simultaneously monitored and compared. Remote systems used at LEO-15 consist of multiple satellite-mounted sensors including Advanced Very High Resolution Radiometer (AVHRR) that provides continuous spatial coverage of sea surface temperature over the region. In addition to temperature, a High Frequency (HF) radar system simultaneously measures surface currents over a fixed grid. A cabled observatory samples subsurface properties including temperature, salinity and pressure. These nodes are also equipped with multiple guest ports so that additional instruments like moored Acoustic Doppler Current Profilers (ADCP's) can be linked to the shore allowing real-time data processing and longer deployments. A meteorological station at the Rutgers University Marine Field Station compliments the ocean observations providing time series data of wind speed and direction, atmospheric pressure, air temperature, and relative humidity. This data rich environment combines spatial remote sensing surface data with subsurface point measurements to provide a well-sampled three-dimensional platform for coastal ocean research.

HF radar is a major component of this multi-system observatory. A single HF radar system consists of at least two remote beach sites each with a transmit and receive antenna. The transmit antenna illuminates a region with radio waves, and the receive

antenna measures the backscatter. HF Radar systems use Bragg peaks within a signal (3 ~ 30 MHz) scattered off the ocean surface to calculate radial components of the total surface velocity at a given location (Barrick, 1977). Crombie (1955) recognized that these peaks were the result of an amplification of a transmitted wave by surface gravity waves with a wavelength equal to half that of the transmitted signal. A signal scattered off a wave and back toward the antenna will be in phase with a signal that traveled to the next surface wave (1/2 transmit wavelength further) and returned to the original wave (another 1/2 transmit wavelength). The frequency of the backscattered signal will be shifted depending on the velocity of the scattering surface. Using linear wave theory the phase speed of the surface waves can be separated from the total frequency shift, leaving only that shift due to the surface current. Since the Doppler shift can only resolve the component of the current moving toward or away from the site, information from at least two sites is geometrically combined to generate total surface current maps.

Numerous HF Radar deployments have been used to study coastal surface dynamics. Monterey Bay has been a test bed for many different HF radar systems including Coastal Ocean Dynamics Applications Radar (CODAR) and Multi-frequency Coastal Radar (MCR). Researchers in Monterey Bay have looked at the low frequency component of CODAR derived velocities to identify cyclonic flow within the bay accompanied by anticyclonic flow offshore. They have identified strong correlation between the low frequency flow and the overlaying wind fields (Paduan and Rosenfeld, 1996; Paduan and Cook, 1997). Ocean Surface Current Radar (OSCR) systems have been used to sample Gulf Stream frontal features and mesoscale eddies off the Florida Keys as well as the propagation of a buoyant Chesapeake Bay plume south along the

continental shelf (Haus et al., 1997). Surface current structure has also been characterized on the continental shelf off the coast of Oregon using a CODAR-type HF radar system. Using a time series of two-dimensional surface current fields, the spatial and temporal variability of the formation of a coastal jet associated with upwelling favorable winds is studied (Kosro et al., 1997). Higher frequency components, including tides, can also be identified using HF radar fields. For example, David Prandle (1997) looks at the propagation of tidal energy form the deep ocean onto the English continental shelf and into shelf seas. Interdisciplinary work has also incorporated surface current maps to link larval distributions with mesoscale current features (Garber and Limouzy-Paris, 1997; Bjorkstedt and Roughgarden, 1997). As a crucial component of the LEO-15 observatory, HF radar has contributed to adaptive sampling and improving numerical model predictions during month-long Coastal Predictive Skill Experiments (Kohut et al., 1999).

The CODAR-type HF radar system at LEO-15 was first deployed in May, 1998 as part of a coastal predictive skill experiment. After this successful summertime test, the system was redeployed in May of 1999 for continuous operation. In addition to the modeling and real-time applications of the data, the long continuous spatial time series captures episodic events within the context of the longer scale current regimes. Therefore, a validated HF radar system is an excellent tool for characterizing the structure of both episodic and seasonal scale responses to local forcing.

1.1 Objective of present study

The objective of this study is to validate and calibrate HF radar data from each site and use the spatial time series data to characterize seasonal and episodic current responses to local forcing. Since HF radar systems depend on antenna patterns in the data processing, factors that contribute to pattern distortion are explored. The sensitivity of the surface current measurement to this distortion is then quantified with a moored ADCP. Each remote site is then calibrated with the known antenna pattern distortion for more accurate spatial time series data.

A yearlong calibrated dataset is then used to characterize the observed seasonal scale variability off the coast of New Jersey. This analysis focuses on the current response to local forcing during the summer stratified season compared to the winter mixed season. During the summer the most significant source of variability in the response is associated with upwelling/downwelling events. The horizontal and vertical structure of the stratified response is then compared to the single layer response of the mixed winter season.

Frequent storms propagate through the study area particularly during the fall and winter months. In September 1999, within the mixed regime, tropical storm Floyd moved through the study site. The short-lived, strong wind forcing associated with the storm and its proximity to the HF radar array offer a unique well-resolved measure of the shallow water response over shorter time scales. This episodic forcing perturbs the seasonal horizontal and vertical structure of the current field with a pulse of energy. The timeline of this current response is characterized with both HF radar and ADCP measurements.

Chapter 2 focuses on the role of antenna pattern distortion on system accuracy and calibration. The seasonal scale variability associated with summer stratification and winter mixing is described in Chapter 3. Using observations in conjunction with simple analytical models, the current response to the short, strong forcing associated with tropical storm Floyd is explored in Chapter 4. Finally, Chapter 5 presents some concluding remarks.

2.0 HF RADAR CALIBRATION AND VALIDATION

2.1 Introduction

High Frequency (HF) radar systems have matured to the point where they are now integral components of coastal ocean observation networks and prediction systems (Glenn et al., 2000b; Paduan et al., 1999). HF radar uses scattered radio waves to measure surface currents, wave parameters and surface wind fields (Paduan and Graber, 1997; Wyatt, 1997; Graber and Heron, 1997; Fernandez et al., 1997). Surface currents, the most common product of HF radar systems, are used for real-time applications (Kohut et al., 1999), data assimilation and model validation (Breivik and Sætra, 2001; Oke et al., 2000; Shulman et al., 2000) and dynamical studies (Shay et al. 1995, Kosro et al., 1997; Paduan and Cook, 1997). This expanding HF radar user community necessitates a better understanding of system accuracy and calibration.

There is a thirty-year history of validation studies using *in situ* observations to ground truth HF radar data. Early studies compared total vector current data measured with HF radar and *in situ* current meters, including Acoustic Doppler Current Profilers (ADCPs) and drifters, reporting RMS differences ranging from 9 to 27 cm/s (for a review see Chapman and Graber, 1997). All agree that physical differences between the types of measurements must be considered when validating HF radar data with *in situ* instruments. These differences can be separated into three categories, velocity gradients (vertical and horizontal), time averaging, and geometric error associated with total vector combination.

A HF radar system operating at a typical frequency of 25 MHz uses the scattered signal off of a 6 m long surface gravity wave to infer near surface current velocities. These current measurements are vertically averaged over the depth felt by the wave.

Assuming a linear velocity profile, Stewart and Joy (1974) estimate that for a 6 m long ocean wave, this depth is about 1 m. At this frequency, any velocity shear between the upper 1m of the water column and the depth of the *in situ* measurement will affect the RMS difference. Graber et al. (1997) demonstrate that the contribution of specific upper ocean processes including Ekman fluxes can lead to differences between remote HF radar and *in situ* current measurements. Additional horizontal differences occur since HF radars are calculating currents based on a return signal that, for a typical 25 MHz system, is averaged over a ^{patch} of the ocean surface that can be as large as 3 km^2, while typical *in situ* current meters measure at a single point. Any surface inhomogeniety like fronts or small eddies will contribute to the observed RMS difference.

The second contribution to the difference is the time sampling of the two instruments. A typical 25 MHz system averages the continuous backscattered data into hourly bins. Often *in situ* measurements are burst sampled because of battery power and data storage requirements. High frequency oscillations such as internal waves could contaminate a short burst in the *in situ* measurement and be averaged over in the HF radar data.

The third possible contribution to the RMS difference between HF radar and *in situ* measurements is related to the geometric combination of radial velocity vectors. Since HF radar systems use Doppler theory to extract surface current information, standard backscatter systems can only resolve the radial current component directed toward or away from the antenna site. At least two spatially separated sites are necessary to calculate the total vector currents for the ocean surface. An example of a radial component velocity map is shown for two coastal sites in Figure 2.1. When estimating

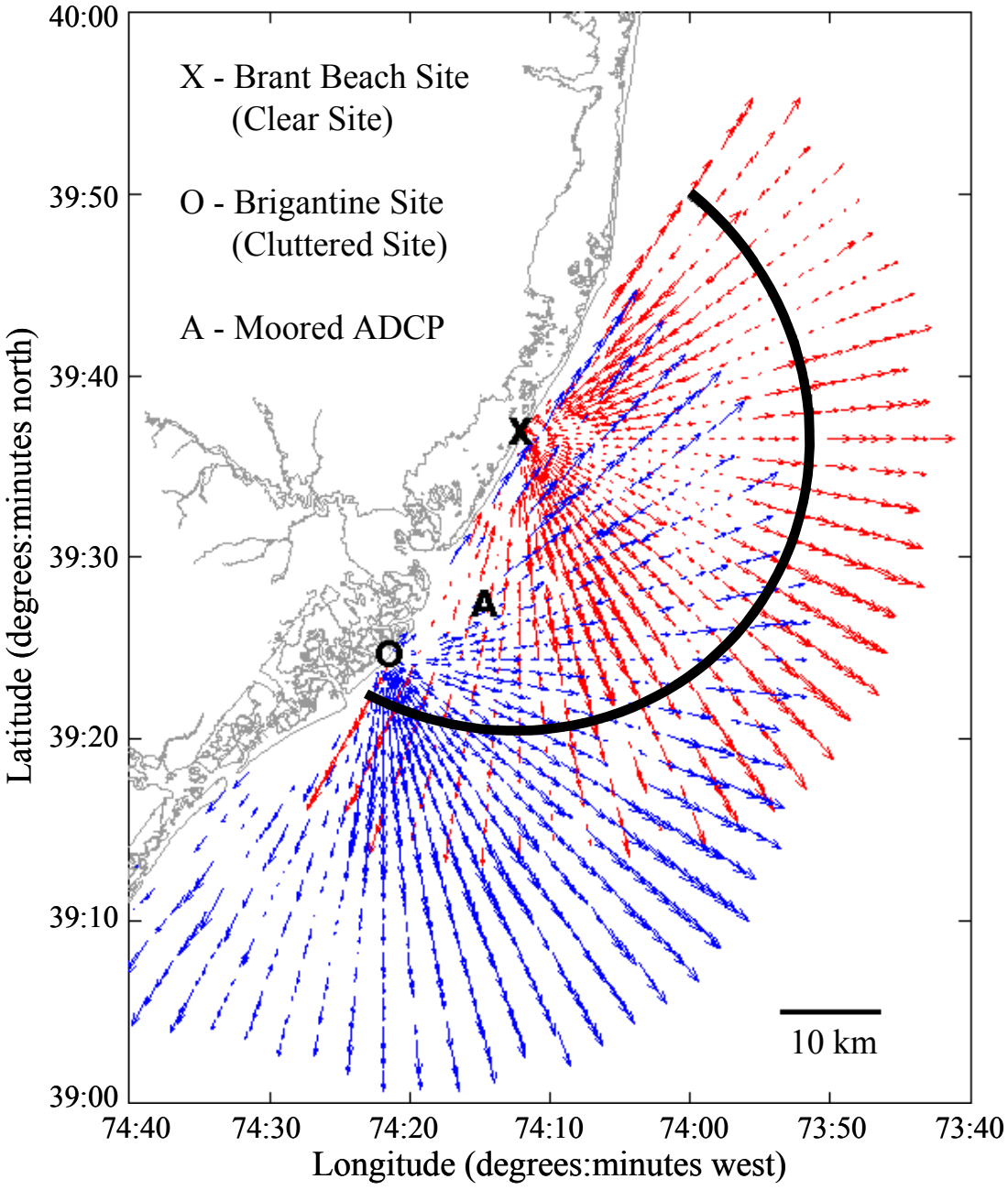

Figure 2.1. Study area off the southern coast of New Jersey including hourly radial maps from the Brant Beach (red) and Brigantine (blue) sites. The solid semicircle highlights a range cell for the Brant Beach Site.

the total current vector from radial components, the further the two radials are from orthogonality, the larger the potential error in the total vector. This is described by Chapman et al. (1997) as the Geometric Dilution Of Precision (GDOP). By using the independent radial velocity measurements from the two remote sites, this study eliminates this error seen exclusively in the total vector calculations.

More recently, the role of receive antenna patterns on system accuracy has been the focus of HF radar calibration. Barrick and Lipa (1986) used an antenna mounted on an offshore oilrig to illustrate that near-field interference can cause significant distortion from ideal patterns. Their study defines this near-field as a circle around the antenna with a radius equal to one wavelength of the broadcast signal. Through simulations, they show that typical pattern distortion can introduce an angular bias as large as 35 degrees if they are not taken into account. Comparisons of radial velocity vectors calculated directly between two HF radar sites located on opposite shores of Monterey Bay, California have also shown an angular bias between the baseline and the best correlation (Fernandez and Paduan, 1996). It is suggested that this bias could be caused by distorted antenna patterns. More recently, Paduan et al. (2001) show that the HF radar correlation with observed currents from an ADCP improves if pattern distortion is taken into account. Kohut et al. (2001) also show the importance of pattern distortion and go on to identify possible sources of this distortion including hardware and the local environment. The HF radar validation results presented in this Chapter will investigate several sources of antenna pattern distortion and quantify how this distortion impacts system accuracy. Section 2.2 briefly describes those features of the operation of HF radar systems relevant to the ensuing discussion. Section 2.3 outlines the specific instrumentation and methods

used in this study. Section 2.4 discusses the source of antenna pattern distortion and the impact of this distortion on system accuracy, and section 2.5 presents some concluding remarks.

2.2 Background

HF radar systems use the return signal scattered off the ocean surface to measure the range, bearing and radial velocity of the scattering surface towards or away from the antenna. The radial velocity is determined using Bragg peaks in the spectra of the backscattered signal (Barrick, 1972; Barrick et al., 1977; Lipa and Barrick, 1986). Crombie (1955) first recognized that these peaks were the result of an amplification of a transmitted signal by surface gravity waves with a wavelength equal to half that of the transmitted signal. The range of the scattering surface is measured using either a time delay or a frequency modulation technique. The methods used to measure the range and radial velocity of the scattering surface are similar for all HF radar systems (Paduan and Graber, 1997). Bearing determination, however, differentiates HF radar systems into two major groups, Beam Forming (BF) and Direction Finding (DF). Both groups illuminate the ocean surface over all angles with a transmitted signal. The difference arises in the reception and interpretation of the backscattered signal. A BF system uses a linear array of vertical elements to steer the receive antenna look angle to different bearings. The bearing of the measured return signal is the look angle of the receive antenna. Some systems mechanically rotate the antenna array (Furukawa and Heron, 1996) and others use the relative phases of the antenna elements to move the receive antenna look angle across the ocean surface. The angular width of the look angle depends on the length of the linear array. A typical 25 MHz system requires an 80 m length to resolve 5 degree

bins. In contrast, a DF system measures the return signal continuously over all angles. The beam patterns of independent antenna elements are used to determine the direction of the incoming signals. The angular resolution, set in the processing, is typically 5 degrees. For a description of the mechanics and operation of these two HF radar systems, the reader is referred to Teague et al. (1997) and Barrick and Lipa (1996).

Coastal Ocean Dynamics Applications Radar (CODAR), a DF system, uses a three element receive antenna mounted on a single post. These elements include two directionally dependent cross-loops and a single omni directional monopole (Lipa and Barrick, 1983; Barrick and Lipa, 1996). Since the monopole is omni directional, the antenna pattern is a circle of constant radius around the antenna post. The theoretical patterns of the two cross-loop elements normalized by the monopole are cosine dependent and oriented orthogonal to each other (Figure 2.2). The peak in Loop 1 coincides with the null of Loop 2 and vice versa. Using a frequency modulation technique (Teague et al., 1997), the continuous data measured by each antenna is separated into distinct range cells. One range cell of a typical radial field is highlighted in Figure 2.1. The Bragg peaks are used to calculate all the radial velocities measured within the range cell. The bearing of each radial velocity is then determined using the frequency spectra from each receive antenna element. Since its inception, the CODAR-type system has used several different algorithms to determine the bearing of a given radial velocity, including a closed form solution and a least-squares fit to the incoming data (Lipa and Barrick, 1983; Barrick and Lipa, 1986). More recently, a much more robust MUltiple SIgnal Classification (MUSIC) algorithm enables the CODAR configuration to resolve more complicated flow fields, including conditions when the

same radial velocity comes from two different directions. MUSIC was first developed by Schmidt (1986) to locate radio signal sources from aircraft. Barrick and Lipa (1999) have modified MUSIC for the specific task of extracting the bearing of a given signal measured by N isolated antenna elements. The algorithm has been evaluated and fine-tuned using simulations to recreate known radial velocity fields (Barrick and Lipa, 1997; Laws et al., 2001). In its present form, MUSIC can use either the ideal or the measured antenna beam pattern of the antenna elements to determine the bearing of a signal scattered off the ocean surface.

The measured antenna pattern differs from the ideal due to distortion caused by coupling with any object other than air within the near-field (about 1 broadcast wavelength). The most significant coupling will occur with objects larger than 1/4 wavelength, especially vertical conductors since the HF radar signals are vertically polarized to enable propagation over the ocean surface. The vertical antenna elements in any HF radar system are more susceptible to beam pattern distortion. For the CODAR-type system the cross-loops are less sensitive since any additional current induced on one side of the loop is approximately balanced by an opposing current induced on the opposite side. Rather than normalizing one cross-loop by the other, measured beam patterns for each loop will be normalized by the monopole (as in Figure 2.2) to maximize our ability to identify distortion. Under ideal conditions, the geometry of a CODAR-type system with a single monopole and two cross-loop elements is such that all current carrying paths of the elements are orthogonal to each other. This orthogonality inhibits any one element from interacting with the other two. When the antenna is mounted in the field, either the local environment or system hardware could induce coupling and change

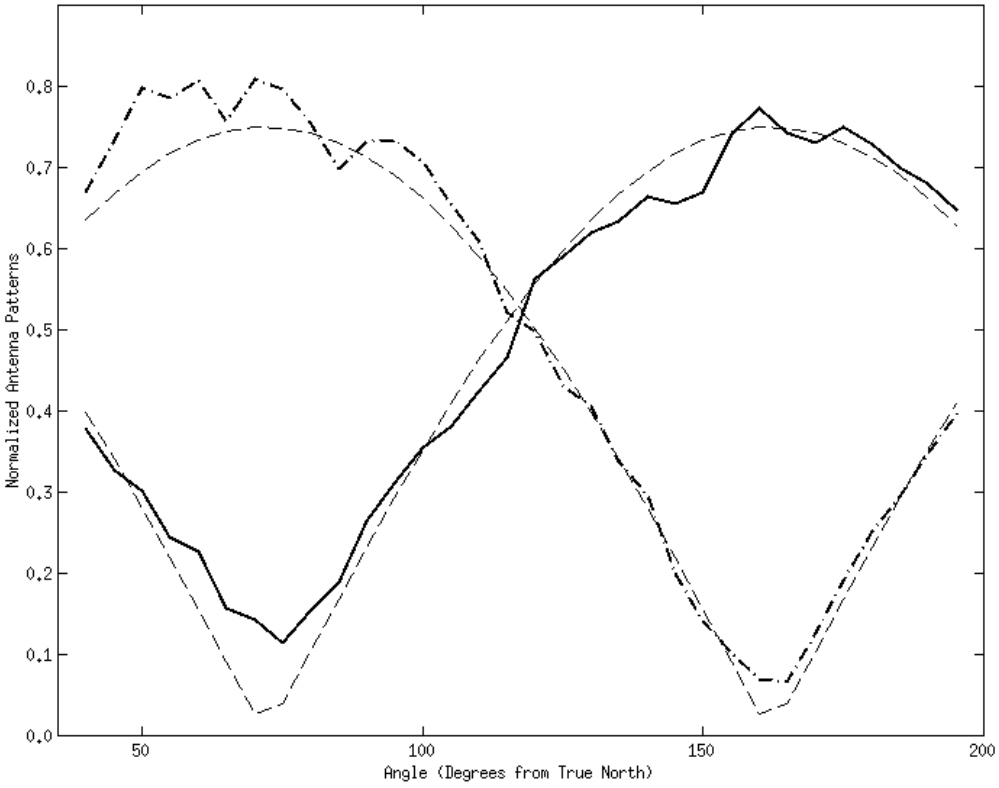

Figure 2.2 Ideal (thin dashed) and measured antenna patterns for loop 1 (thick solid) and loop 2 (thick dash-dot) normalized by the monopole.

this ideal condition. If the geometry breaks down, the antenna elements interact, causing the ideal pattern to distort. This study will examine the effect of system hardware and the local environment on antenna patterns, and compare ocean currents estimated with both the ideal and measured patterns with *in situ* surface current measurements.

2.3 Methods

2.3.1 HF radar setup

The 25 MHz CODAR system used here includes two remote antenna sites separated by 26 km in Brant Beach and Brigantine, New Jersey (Figure 2.1). The first deployment of this system ran from May to August 1998. The success of this first summer test prompted a second continuous deployment that began nine months later in May of 1999 and is continuing to sample in real-time, surviving tropical storm Floyd and many nor'easters. Since the remote sites can only resolve the component of the velocity moving toward or away from the antennas, radial current maps are generated at each site. Each field has a range resolution of 1.5 km and an angular resolution of 5 degrees. The radial velocities are based on hourly averaged backscatter data. The fields are center averaged at the top of the hour. This study uses radial velocities collected between October 16, 1999 and January 24, 2000. By using the radial velocity components from each site, the contribution of GDOP is eliminated from the investigation.

The antenna patterns were measured using a transponder that modifies and re-radiates the transmitted signal (Barrick and Lipa, 1986; Barrick and Lipa, 1996). The small battery operated transponder is mounted on the deck of a boat that tracks along a semi-circle around the receive antenna, maintaining a constant speed and radius. For this particular study, the boat maintained a range of 1 km and a speed of 5 knots. At the

remote site, raw time series data were measured by each receive element. The time series were combined with the boat's GPS data to determine how the transponder signal varied with angle for each antenna element.

Table 2.1 summarizes the pattern runs completed at the two CODAR sites. Each pattern run is the average of two boat transects, one circling north to south and the other

Table 2.1. Antenna Pattern Measurement Runs

Run Number	Ground Plane	Environment	Antenna	Receiver	Date
1	2.4 m	Cluttered	B	B	October, 1999
2	1.2 m	Cluttered	B	B	October, 1999
3	2.4 m	Clear	A	A	October, 1999
4	1.2 m	Clear	A	A	October, 1999
5	1.2 m	Clear	A	A	September, 2000
6	1.2 m	Clear	B	A	September, 2000
7	1.2 m	Clear	B	B	September, 2000
8	1.2 m	Clear	A	A	September, 2000
9	1.2 m	Cluttered	B	B	November, 2000
10	1.2 m	Cluttered	A	B	November, 2000
11	1.2 m	Cluttered	B	B	November, 2000
12*	1.2 m	Cluttered	B	B	November, 2000
13	1.2 m	Cluttered (New)	B	B	October, 2001

* Same as run 11 except different cable location.

circling south to north. The distortion for each run is calculated by subtracting the measured pattern from the ideal pattern. Since the MUSIC algorithm adjusts the pattern amplitude based on measured sea echo, the ideal pattern is taken as the best-fit cosine through the measured pattern (Figure 2.2). The sites in Table 2.1 are labeled according to the characteristics of the near field. Both sites, operating at 25.41 MHz and 24.70 MHz, have a near-field with a radius of about 12 m. The antenna setup in Brant Beach is mounted on a sand dune close to the surf zone where there are no buildings or any other known interference within several wavelengths of the antenna. This site has a clear near-field and will be referred to as the clear site. In Brigantine, the antenna is mounted on a sand dune within one wavelength of a six-story condominium. The presence of this large

building potentially clutters the near-field, so the Brigantine site will be referred to as the cluttered site. The ground plane length referred to in Table 2.1 is the length of the four horizontal fiberglass whips that make up the ground plane of the monopole element. During normal operation, antenna A and receiver A are the receive antenna and receiver setup at the clear site, and antenna B and receiver B are setup in the cluttered site.

The bearing of each radial velocity in a given range cell was calculated once with the ideal pattern and twice with the measured pattern, both with and without outlier elimination, angular interpolation, and smoothing. Outliers were identified using the median of the vectors that fall within 20 degrees of the data point. If the data value is more than 25 cm/s from the median value, it is eliminated from the radial field. The interpolation algorithm then uses a Guassian window with a half power width of 20 degrees to smooth and interpolate the data. Radial velocities that are more than 10 degrees from the interpolated value are weighted significantly less than data within 10 degrees of the interpolated radial velocity (Barrick and Lipa, 1996). This algorithm is used exclusively on the measured pattern data.

2.3.2 ADCP setup

A single bottom-mounted ADCP was deployed at the Longterm Ecosystem Observatory (LEO-15) from July, 1999 to February, 2000 (Grassle et al. 1998; Glenn et al. 2000a; Schofield et al. 2001). Real-time data was sent from the seafloor node through a fiber optic cable to a computer on shore. The location of this ADCP is shown in Figure 2.1. The ADCP operated at 1200 kHz with a bin resolution of one meter. The ADCP continuously sampled in mode-1 at a sample rate of 400 pings per one-minute ensemble.

Since the ADCP was continuously sampled, the potential difference due to burst sampling was eliminated from the dataset. These data were hourly averaged, centered at the top of the hour, to exactly match the sampling of the CODAR systems. The shallowest bin without side lobe interference was used in the comparisons. This bin was determined for each data point using the ADCP pressure record by maintaining a depth of about 2.5 meters below the surface. The resulting ADCP comparison is then as close to the surface as possible throughout the entire record. The north/south and east/west components of the velocity measured in the surface bin were rotated into a radial/cross-radial coordinate system for each site. The radial component of the ADCP data was compared directly to the radial CODAR data, eliminating the error due to GDOP. The contribution of vertical shear to the RMS difference was estimated with the ADCP. The velocities measured at the surface following and 4.5 meter depth bins had a RMS difference of 2.6 cm/s (Figure 2.3). The comparison indicates that the contribution of vertical shear to the RMS difference is on the order of 2.5 cm/s.

2.4 Results and discussion

2.4.1 Antenna pattern distortions

Ground plane. The ground plane of the monopole is made up of four horizontal fiberglass whips at the base of the antenna box. These four orthogonal whips are oriented in the alongshore and cross-shore directions. Pattern measurement runs tested two whip lengths, 1.2 m and 2.4 m, in each environment. Runs 1 and 2, completed approximately thirty minutes apart, measured the pattern of antenna A with the two different ground

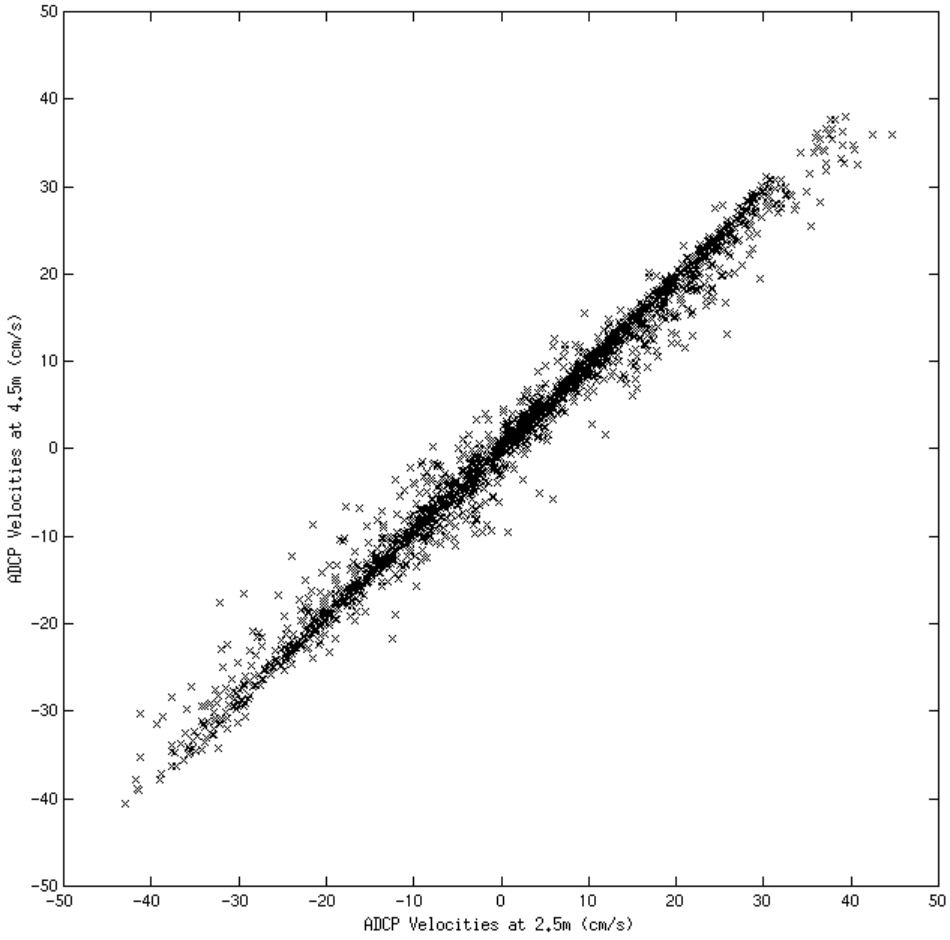

Figure 2.3. Scatter plot of ADCP current measurements at surface following and 4.5 meter depth bins.

planes in the clear environment. The patterns show that the 2.4 m ground plane causes a much larger distortion than the shorter ground plane (Figure 2.4a and 2.4b). The patterns indicate a stronger coupling between the ground plane and the two loops with the longer ground plane. At an operating frequency of 25 MHz, 2.4 m is a quarter wavelength. This quarter wave ground plane is resonant and therefore very efficient. The stronger currents within the ground plane induce strong signals on the two loops resulting in significant pattern distortion. When the whips are reduced to 1.2 m, the efficiency of the ground plane is reduced and the magnitude of the coupling diminishes. The influence of element interaction on antenna pattern distortion has been studied theoretically using an exact industry standard Numerical Electromagnetics Code (NEC) ideally suited for HF (Burke, 1992). These studies have shown that the resonant ground plane will amplify the coupling between antenna elements. The observations measured in the clear environment support the theoretical results of the NEC.

The distortion of the pattern measured with the resonant (2.4 m) ground plane is relatively larger near the endpoints (Figure 2.4a). Since these patterns are measured using a transponder mounted on a boat, the pattern endpoints correspond to the coast on either side of the antenna. As the transponder gets close to the coast, the signal must travel over more of the beach to get to the antenna. When a signal travels over a less conductive surface, like sand, the signal strength quickly drops off. The increased distortion seen near the edges of the pattern is correlated with this weaker transponder signal. Theory suggests that pattern distortions caused by coupling between the individual elements will be relatively larger for angles with relatively weaker signals

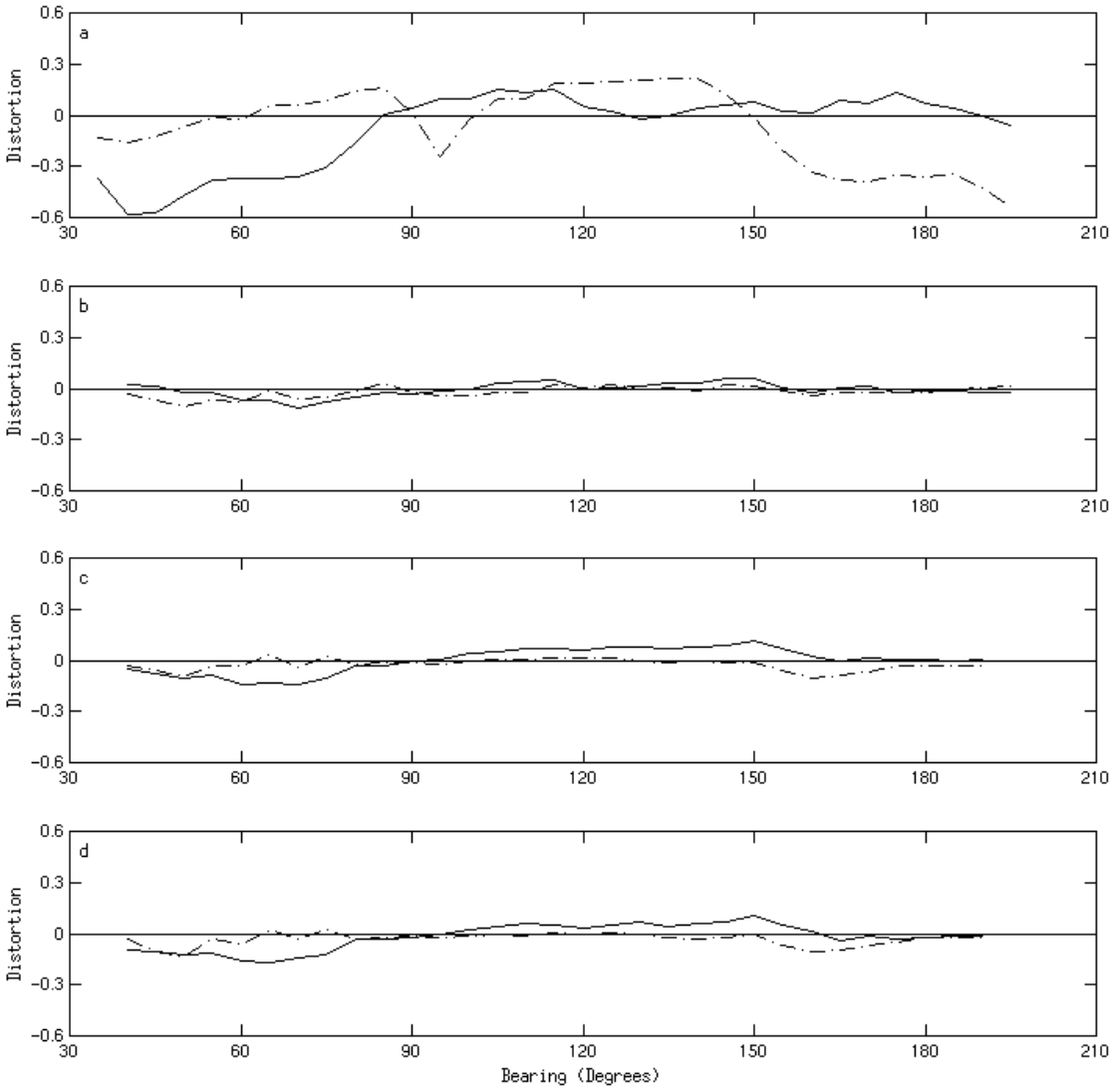

Figure 2.4. Normalized antenna pattern distortion for loop 1 (solid) and loop 2 (dash-dot) measured at the clear Brant Beach site for (a) run 3, (b) run 4, (c) run 6, and (d) run 7.

(Burke, 1992). The larger distortion at the endpoints of the pattern further supports the antenna element interaction seen with the resonant ground plane.

The sensitivity of the antenna pattern to the length of the ground plane was also tested in the cluttered environment. Runs 3 and 4 measured the pattern of antenna B with the resonant and non-resonant ground planes. The pattern measured with the resonant ground plane has significant distortion over all angles (Figure 2.5a). The pattern with the non-resonant ground plane has less distortion, especially near the edges (Figure 2.5b). While changing the ground plane improves the pattern near the edges, the non-resonant pattern remains more distorted than the pattern measured in the clear site with the same setup. The remainder of this section will test and discuss the contribution of several possible sources responsible for this difference, including system hardware and the local environment.

Receiver. The receiver is the interface between the computer, the receive antenna and the transmitter. It houses the hardware components responsible for generating the transmitted signal and receiving the backscattered signal. The three coaxial cables from the antenna elements are attached to the back of the chassis. During these tests beam patterns using receivers A and B were measured in the clear environment. The patterns measured with the different receivers in the same environment show no significant difference (Figure 2.4b and 2.4d). Both patterns show relatively small distortion over all angles. The similarity between these two patterns indicates that the receiver does not account for the difference seen in the patterns measured at the clear and cluttered environments with the non-resonant ground plane.

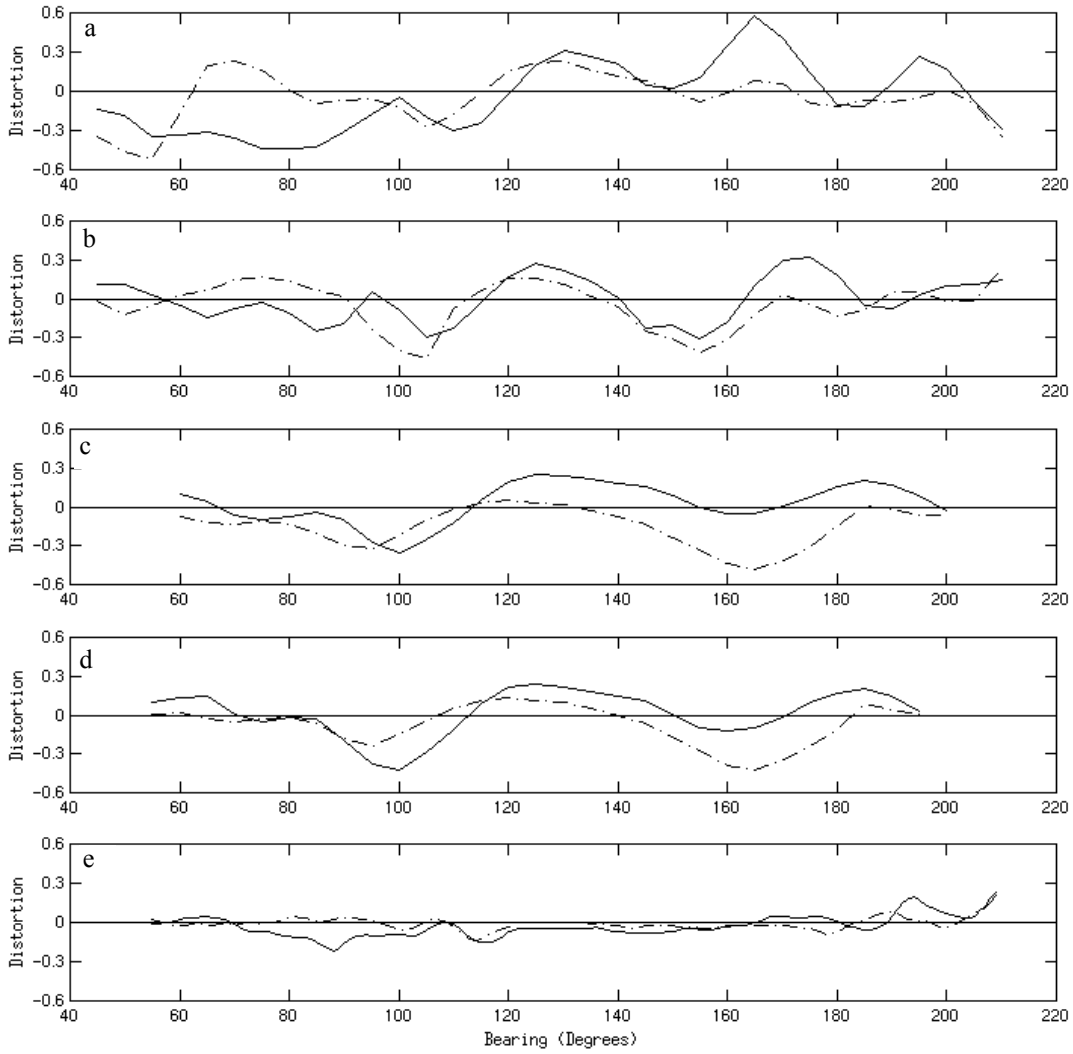

Figure 2.5. Normalized antenna pattern distortion for loop 1 (solid) and loop2 (dash-dot) measured at the cluttered Brigantine site for (a) run 1, (b) run 2, (c) run 12, (d) run 10, and (e) run 13.

Cables. The receive cables run from the receiver to the antenna elements. Electrical currents can build up along the cables and disrupt the ideal geometry discussed previously. If these currents exist, than the location of the cables with respect to the antenna could change the measured pattern. During normal operation these currents are inhibited by a tight loop in the cables near the base of the antenna. To test the effectiveness of this loop, the same system setup was measured with two different cable locations. During run 12, the cables were run as they would be during normal continuous operation. Immediately following this run, the cables were moved closer to the ocean, maintaining the tight loop near the base of the antenna. A comparison between these runs shows that there is no significant difference between the patterns (Figures 2.5b and 2.5c). Based on these results, the loop is an effective way of reduce electrical currents along the receive cables that can lead to pattern distortion.

Receive antenna. The receive antenna consists of three independent antenna elements. Antennas A and B were switched so that beam patterns for both antennas could be measured in each environment. Runs 4 and 6 illustrate the difference between the patterns of antenna A and antenna B in the clear environment. The patterns of the two antennas in the clear environment are not significantly different (Figures 2.4b and 2.4c). There are some small differences, however they are much smaller than those seen in the patterns of the two antennas in different environments. Patterns for the two antennas were also measured in the cluttered environment (Figure 2.5b and 2.5d). Again they are very similar and both show significant distortion across much of the pattern. These results indicate that the antenna hardware does not account for the difference in the patterns measured at each site with the non-resonant ground plane.

Local environment. Patterns measured with the same hardware in the clear and cluttered environments were used to determine the impact of the local environment on antenna pattern distortion. The pattern of antenna B in the cluttered environment is significantly distorted from the theoretical ideal pattern (Figure 2.5b). When this antenna is moved to the clear site these distortions are significantly reduced (Figure 2.4c). The results for antenna A show a similar trend in that the patterns measured at the cluttered site are significantly more distorted than those measured at the clear site (Figures 2.4b and 2.5d). Recently the cluttered site was moved 500 m to the southwest to a more stable beach location. The new location offers a more open near-field on a dune similar in composition to the setup at the clear site. After antenna B was moved the patterns were re-measured. The pattern measured at the new location is much closer to ideal than at the previous location (Figure 2.5e). These observations clearly indicate that interference within the antenna's near-field significantly influences pattern distortion. If either antenna A or B is set up in a clear environment, the patterns are much closer to ideal than if the same antenna is measured in a cluttered environment.

Time dependence. The time dependence of the measured patterns is very important to document since the patterns can be used to calibrate HF radar systems. The time scale of the pattern changes will dictate the frequency of the measurement necessary to accurately calibrate these systems. The time dependencies of these patterns were determined by comparing like runs measured at different times. Both runs 2 and 5 measured the same system hardware in the clear environment 11 months apart. The measurements indicate that while the amplitude of the pattern changed over time, the angular dependence of the pattern did not (Figure 2.2 and 2.6a). These patterns are

normalized by the omnidirectional monopole. If the strength of the monopole decreases, the amplitude of the normalized pattern will increase. Since the change in the pattern is felt equally over all angles, the difference in the normalized pattern can only be attributed to a weaker monopole. During the hardware changes for runs 6 and 7, the cable connecting the receiver to the monopole was disconnected and reconnected. The same hardware was then measured again in run 8. After the cable was reconnected, the pattern amplitude returned to the same order seen 11 months before (Figure 2.6). Again the directional dependence of the pattern did not change. The tighter cable connection strengthened the monopole and decreased the amplitude of the normalized pattern. This indicates that the only change seen in the antenna pattern over the 11 month period is the strength of the monopole.

Similar tests were completed in the cluttered environment. These runs measured the same system setup 13 months apart. Again the amplitude, not the directionality, of the pattern was affected. The amplitude measured in October 1999 is on the order of 0.80. The amplitude of the same system setup measured 13 months later increased to about 1.50. After several hardware changes, the monopole connection was strengthened and the pattern amplitude returned to 0.65, the same order as that measured 13 months before. Through all of these runs the directional dependence of the patterns remained the same. Since the MUSIC algorithm uses measured sea echo to adjust pattern amplitudes, it is only important that the directional dependence of the pattern be maintained. The results from both sites indicate that the directionality of the normalized pattern measured in either environment did not significantly change over annual time scales. Based on

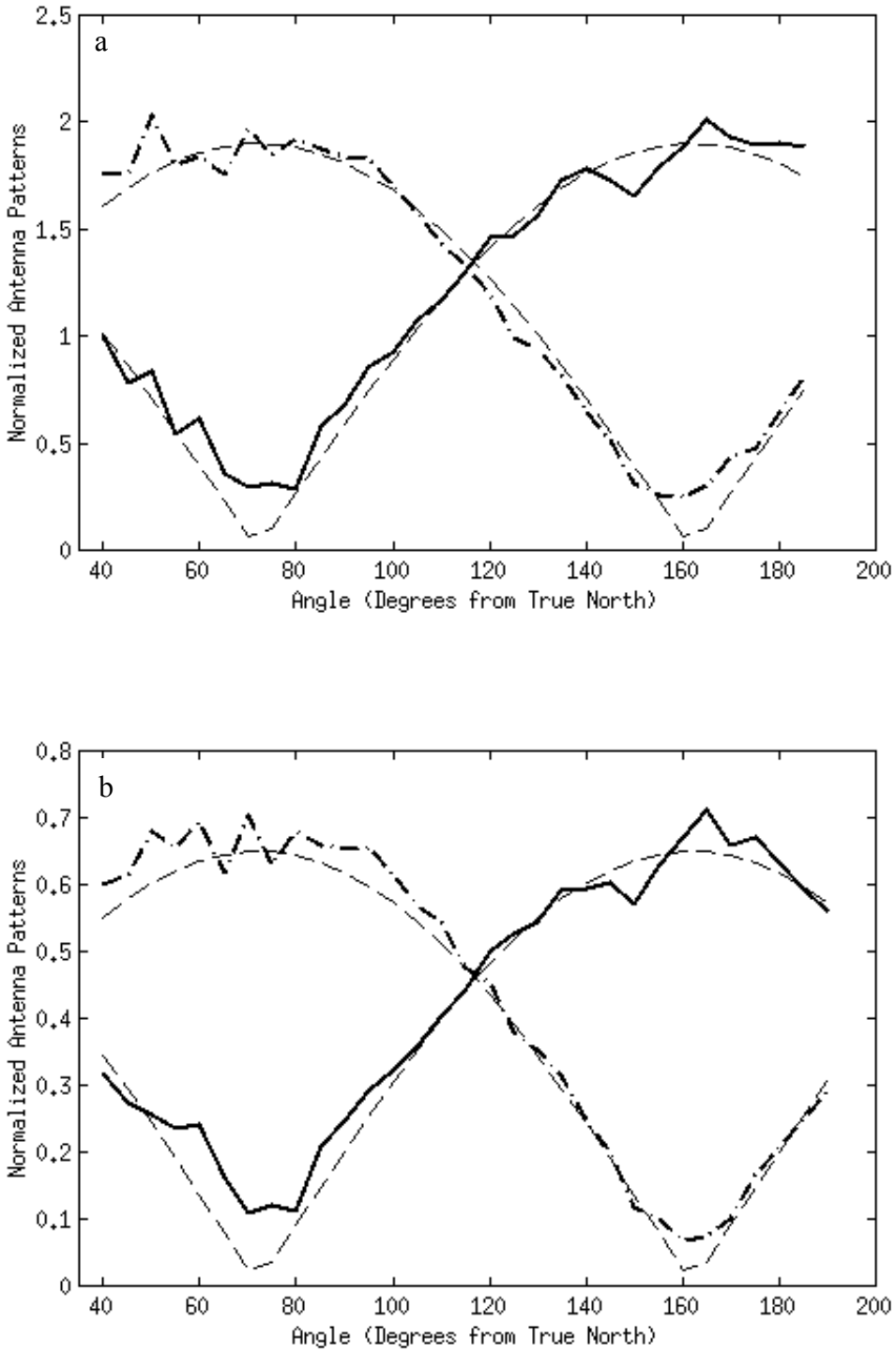

Figure 2.6. Antenna patterns of loop 1 (thick solid) and loop 2 (thick dash-dot) normalized by the monopole in the clear site during (a) run 5 and (b) run 8.

these conclusions, annual calibration runs appear to be sufficient to maintain the calibration of a CODAR site.

The pattern measurements shown here indicate that the length of the monopole ground plane and the local environment play an important role in antenna pattern distortion. If the ground plane is resonant or there is interference within the antennas near-field, the ideal geometry of the antenna breaks down and the elements interact. This breakdown has also been shown theoretically to cause inter-element interaction that distorts the antenna pattern (Burke, 1992).

2.4.2 ADCP comparisons

The MUSIC algorithm can use either the measured or ideal pattern to determine the bearing of a given radial velocity. The processing can also utilize an angular interpolation scheme to fill in radial data gaps. Since the measured pattern results usually have more data gaps than the ideal pattern results (Paduan et al. 2001), the interpolation was used exclusively on these data. The ideal, measured and measured-interpolated CODAR results were each independently validated against a moored ADCP. Between October 16, 1999 and January 24, 2000, the CODAR sampling was separated into two regimes. From October 16, 1999 to December 4, 1999, the antennas were setup with the resonant 2.4 m ground plane. From December 6, 1999 to January 24, 2000, the ground plane was shortened to the non-resonant 1.2 m. These tests take advantage of the amplified distortion observed with the resonant ground plane so that the effect of this distortion on system accuracy is more easily observed. Additionally, the ADCP was moored near the edge of the antenna pattern for each remote site, so these comparisons

also focus on the portion of the pattern most affected by antenna element interaction. Results from the clear site indicate the influence of the pattern distortion on the ADCP

Table 2.2 ADCP Comparison Statistics for the Clear Environment				
Ground Plane	Antenna Pattern	RMS Difference	R^2	Number of Points
2.4 m	Ideal	9.53 cm/s	71%	682
2.4 m	Measured	7.37 cm/s	90%	314
2.4 m	Measured-Interpolated	7.75 cm/s	86%	594
1.2 m	Ideal	8.30 cm/s	81%	99
1.2 m	Measured	8.40 cm/s	83%	224
1.2 m	Measured-Interpolated	7.80 cm/s	88%	549

comparisons (Table 2.2). When the larger ground plane was tested, the ideal results had a RMS difference of 9.53 cm/s and a correlation of 71%. When the large distortion was accounted for in MUSIC by using the measured pattern, the RMS difference improved to 7.37 cm/s with a correlation of 90%. With the non-resonant ground plane, the distortion is significantly reduced and there is only a small difference between the ideal and measured patterns. The ADCP comparisons show that either pattern has RMS differences on the order of 8 cm/s with an average correlation of 82%. With the near ideal pattern, the accuracy of the CODAR measurement is independent of the pattern used in the processing. However, if these patterns are distorted, surface current measurements are more accurate when MUSIC uses the measured pattern.

Table 2.2 also shows the number of concurrent data points from each instrument used in the comparison. One consequence of using the measured pattern in the MUSIC processing is that certain radial directions are favored over others. The number of points used in each comparison indicates this asymmetry in the radial fields. The angular interpolation within a given range cell was used in the processing to fill in these gaps. The interpolated data was compared to the ADCP to assess the validity of the algorithm. With a RMS difference of 7.75 cm/s and a correlation of 86%, the interpolated data

correlation is on the same order as the measured pattern data without interpolation. These results hold true for both the resonant and non-resonant cases. With both ground planes, the interpolated data had similar statistical comparisons as the measured pattern data and proves to be an effective algorithm for filling in radial data gaps.

The same study was repeated in the cluttered environment. This site differs from the clear site in that the patterns are distorted with both the resonant and non-resonant ground planes. The only similarity is that the distortion near the endpoints was reduced

Table 2.3. ADCP Comparison Statistics for the Cluttered Environment

Ground Plane	Antenna Pattern	RMS Difference	R^2	Number of Points
2.4 m	Ideal	7.19 cm/s	84%	699
2.4 m	Measured	6.83 cm/s	94%	190
2.4 m	Measured-Interpolated	7.65 cm/s	82%	722
1.2 m	Ideal	7.76 cm/s	90%	694
1.2 m	Measured	7.68 cm/s	93%	632
1.2 m	Measured-Interpolated	6.70 cm/s	90%	920

with the shorter ground plane. With the resonant ground plane, the results using the measured pattern improved the ADCP correlation from 84% to 94% (Table 2.3). These results are consistent with those found at the clear site. With the non-resonant ground plane, the results did not differ significantly between the measured and ideal patterns. Even with the distortion near the center of the pattern, the reduced distortion near the endpoints is sufficient to equalize the two results. These observations suggest that the distortion near the center of the pattern may not influence the radial data distribution near the edge of the pattern.

Since MUSIC uses the antenna pattern to determine the bearing of each radial velocity observed in a given range cell, comparisons between the ADCP and radial currents from all other angles in the CODAR range cell may indicate why pattern measurements improve system accuracy. The RMS difference between the ADCP and

all CODAR grid points was determined for the ideal, measured and measured-interpolated CODAR data. Since bearing solutions estimated with the ideal pattern are found over 360 degrees and solutions with the measured pattern only occur over the range covered by the boat measurement, solutions over land sometimes are included in the ideal pattern results. Paduan et al. (2001) suggest that the ideal solutions outside the measured pattern domain result from pattern distortion. The angular dependence of the RMS difference between the ADCP and uncalibrated CODAR data estimated with the ideal pattern has a very broad minimum shifted to the right of the ADCP (Figure 2.7a). When the data is calibrated with the measured pattern, the RMS value at the ADCP is lower and the minimum is shifted toward the ADCP. With the non-resonant ground plane, the angular dependence of the RMS comparison does not differ significantly for the two patterns (Figure 2.7b). This is to be expected since the two patterns are almost identical and the CODAR estimates should be similar. If the patterns are distorted, the correlation statistics are improved by more consistently placing radial velocities in the appropriate angular bin.

The angular validation at the cluttered site supports the results found in the clear site. If the pattern is distorted, the lowest RMS difference is closer to the ADCP when the measured pattern is used (Figure 2.7c). Even with the pattern distortion seen with the non-resonant ground plane, the ADCP correlation statistics did not change (Table 2.3). Similarly, the angular dependence of the RMS difference does not change between the ideal and measured pattern estimates (Figure 2.7d). With the ADCP location near the edge of the pattern, these results indicate that pattern distortion may only affect local bearing estimates.

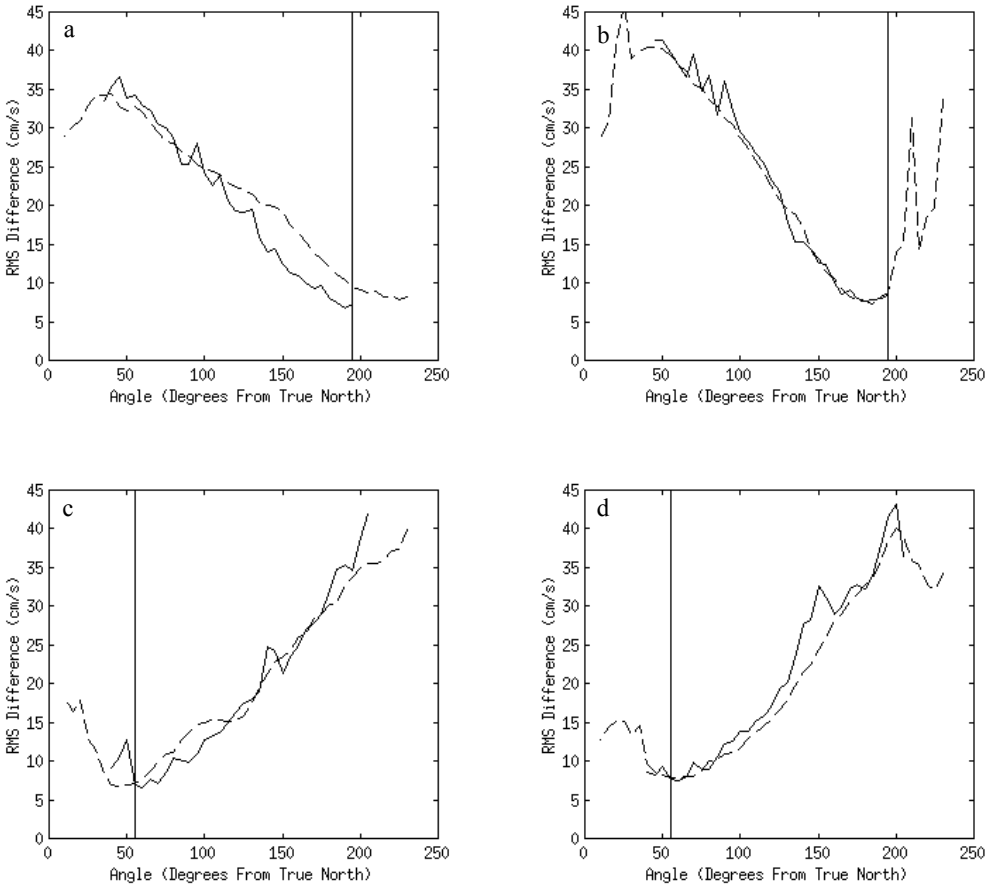

Figure 2.7. RMS difference between the radial velocities of the ADCP and each CODAR angular bin within the range cell passing through the ADCP using the measured (solid) and ideal (dashed) antenna patterns. Comparisons were made at the clear site with the (a) resonant and (b) non-resonant ground plane, and repeated at the cluttered site with both the (c) resonant and (d) non-resonant ground plane. The angular bin containing the ADCP is shown as a vertical black line.

The measured and interpolated data for the entire clear site range cell was also compared to the ADCP. If the interpolation is used, the data gaps or spokes seen in the estimates calibrated with the measured pattern are filled in (Figure 2.8). The RMS curves for the measured and interpolated measured data are nearly identical, indicating that the two datasets compare similarly to the ADCP. Since the algorithm is using a twenty-degree window for interpolation and smoothing, the RMS minimum in the interpolated data is broader than the measured result without interpolation (Figure 2.8). The algorithm used here is an effective method for filling in radial data gaps in the calibrated data. The comparisons with the ADCP show that the CODAR data calibrated with the measured antenna pattern has a higher correlation. These results are especially evident if the patterns are significantly distorted, as is the case with the resonant ground plane. If the measured and ideal patterns do not significantly differ, the correlation remains high regardless of the pattern used in the processing. This study takes advantage of the ADCPs proximity to the endpoint of the pattern, the area most affected by antenna element interaction. The next section will expand these results over all angles by looking at comparisons between calibrated and uncalibrated CODAR data.

2.4.3 Measured vs. ideal

The results of the previous section showed that for the angles looking toward the ADCP, system accuracy improved with the measured pattern if significant distortion exists. To spatially extend the ADCP results, this section discusses comparisons between CODAR currents generated with the ideal and the measured antenna patterns over all angles. In the following analysis, data from the clear site CODAR range cell passing

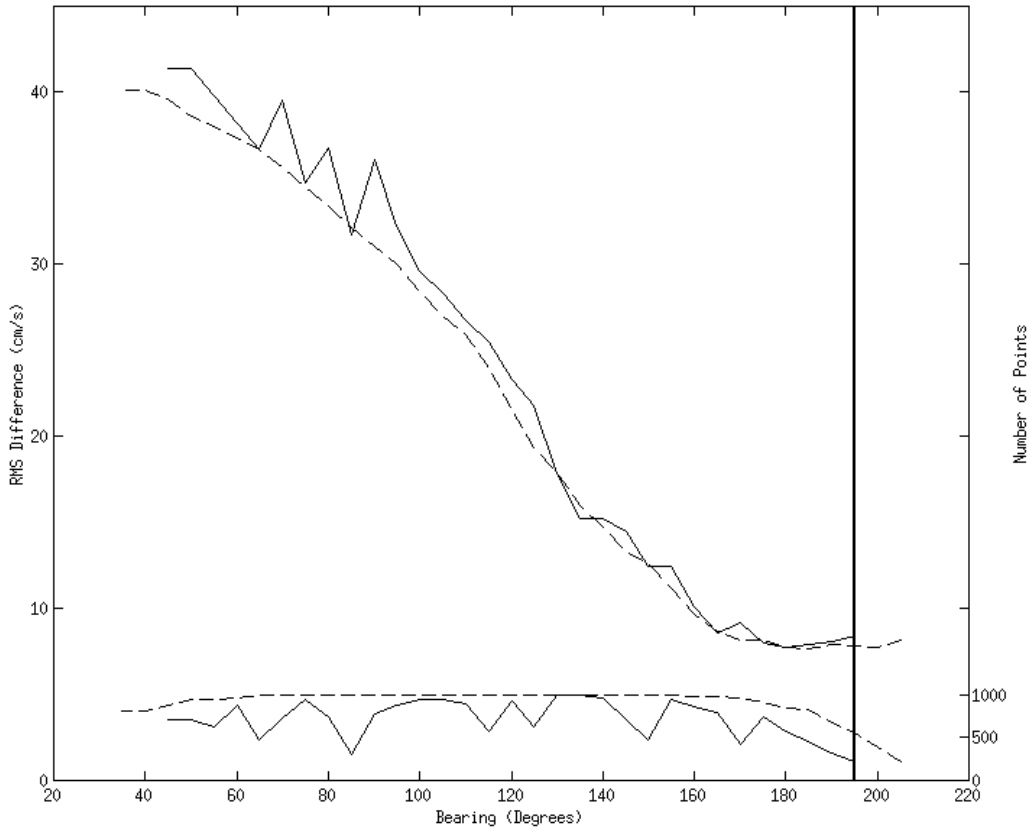

Figure 2.8. RMS difference (upper lines) at the clear site between the radial velocities of the ADCP and each CODAR angular bin within the range cell passing through the ADCP using the measured antenna pattern with (dashed) and without (solid) the interpolation-smoothing algorithm. The number of data points (lower lines) for each angular bin with (dashed) and without (solid) the interpolation-smoothing algorithm.

through the ADCP was used. Measured pattern radial currents from a specific angular bin were compared to the ideal pattern radial currents from all angular bins. The RMS difference calculations were then repeated for each angular bin in the range cell. Figure 2.9 shows contour plots of the RMS difference between the measured and ideal pattern results. The x-axis is the reference angle from true north for each angular bin of the measured pattern. The y-axis is the relative angle between the measured angular bin and the ideal angular bin. Zero relative angle means the measured and ideal angular bins are collocated, and positive relative angles imply that the ideal angular bin is north of the measured angular bin. The dashed line indicates the ideal bin with the lowest RMS difference. When the patterns are distorted, the measured and ideal results of the same angular bin do not have the lowest RMS difference (Figure 2.9a). The dashed line shows that the lowest RMS difference could be with a grid point as far as 50 degrees away. This angular offset is shown to be very dependent on the measured angular bin with a larger offset near the edges. This appears to be related to the increased distortion measured near the coast. If the resonant ground plane is replaced with a shorter non-resonant ground plane, the distortion near the edge of the pattern is reduced. The ideal bin with the best correlation to the calibrated result is much closer to the calibrated data point (Figure 2.9b). This is to be expected since the measured pattern is almost ideal.

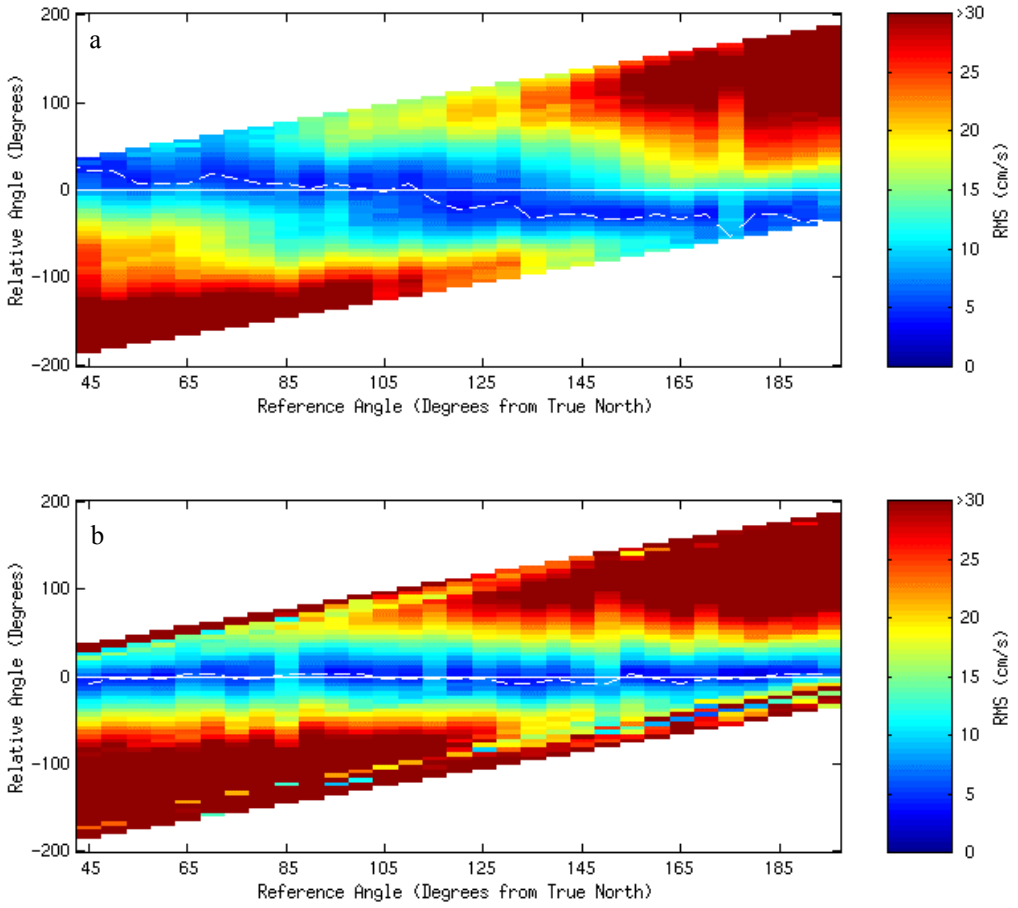

Figure 2.9. RMS difference between the measured and ideal pattern current estimates at the clear site with the (a) resonant and (b) non-resonant ground planes. The lowest RMS difference for each bin is shown as a dashed line.

2.5 Conclusions

As the role of HF radar becomes increasingly more important in coastal observatories and regional modeling efforts, it is imperative to properly calibrate all systems to ensure high data quality. System accuracy is shown to be dependent on the distortion of the measured pattern. This distortion is related to the interaction between the individual elements, whether caused by a resonant ground plane or the local environment. In many cases distortion is unavoidable due to site location constraints. For these instances it is necessary to calibrate the data with the measured pattern. Unless the measured pattern is nearly ideal, ADCP comparisons indicate that the CODAR bearing estimates are more accurate if MUSIC uses the measured pattern. A direct CODAR to CODAR comparison shows that the offset between the measured and ideal angular bins with the lowest RMS difference extends over all angles when the pattern is distorted over all angular bins. To maximize any HF radar's usefulness for scientific and operational applications, the antenna patterns for each site must be measured and, if distorted, these patterns should be used in the processing to calibrate and improve the surface current measurements.

3.0 SEASONAL CURRENT VARIABILITY OVER THE INNER SHELF

3.1 Introduction

The Middle Atlantic Bight (MAB) has been a regional focus of coastal research since the early 1900s. Beardsley and Boicourt (1981) present a literature review of the estuarine and coastal circulation studied from Cape Cod, Massachusetts south to Cape Hatteras, North Carolina. Early observations described by Bigelow (1933) and Bigelow and Sears (1935) show the hydrography of the MAB has a strong seasonal cycle. Typically strong stratification, brought on by warmer temperatures and increased freshwater runoff, exists beginning in the early spring and continuing through the summer. This stratification is broken down in the fall and early winter by strong storms and cooler temperatures. The first dynamical model for the MAB showed a southwest drift of shelf and slope waters from Cape Cod toward Cape Hatteras (Sverdrup et al., 1942). Miller (1952) later showed that there was strong variability about this mean drift in the form of eddies and current filaments. Chapman and Beardsley (1989) suggest that the origin of the shelf water is from glacial melt along the southern Greenland coast that propagates south to the MAB as a buoyant coastal current. Beardsley and Winant (1979) show that the southwest flow of this cold glacial water is primarily driven as a boundary current connected to the larger scale circulation of the western North Atlantic Ocean. Technology allowed more long term measurements of currents, water temperature and salinity, and meteorological forcing in the 1960's. Beardsley and Boicourt (1981) describe much of the work using these longer time series confirming that transient currents modulate the mean southwest drift. The focus of dynamical research in the 1970's shifted from the mean southwest flow to the current variability. Beardsley et al.

(1976) suggest that the current variability of the MAB is mostly wind-driven. Moores et al. (1976) show that the wind forcing driving this variability is predominately from the west/northwest except in the summer months when the wind is typically from the southwest. Ou et al. (1981) go on to show observationally that the variability is composed of a wind forced component and a larger scale free wave component that is not correlated with the wind and propagates downshelf. Using numerical simulations, Beardsley and Haidvogel (1981) confirm that these current fluctuations do have a local and non-local response. The local response is related to local geometry, topography and forcing and the non-local response is due to forcing "distant in time and space".

More recent work in the MAB focused on the locally forced variability, particularly in the summer months when the water column is strongly stratified. The strongest signal typically observed along the New Jersey coast during the summer stratification season is coastal upwelling/downwelling. The theories of coastal upwelling have been studied and tested since Ekman (1905) first solved the equations of motion and successfully explained depth-averaged transport perpendicular to the wind. Ekman theory has very important consequences when applied to the coastal ocean. Unlike the deep ocean, shallow water limits the depth of the Ekman layer. An alongshore wind stress has the potential to force a significant offshore transport of surface waters and an onshore transport of nutrient rich bottom water into the euphotic zone (Brink et al., 1998). Traditional coastal upwelling regions include the Peruvian coast (Brink et al, 1980), coastal waters off California (Narimousa and Maxworthy, 1987) and Oregon (Halpern, 1976) as well as Western Africa (Halpern, 1977). A series of observational and numerical studies of the coastal ocean focused on the region off the Northern California

coast (Beardsley and Lentz, 1987). These Coastal Ocean Dynamics Experiments (CODE) looked at both the local and regional response of the coastal ocean to atmospheric and freshwater forcing. Davis and Bogden (1989) describe the difference seen in the current response over a deep (greater than 60 m) and shallow (less than 60 m) shelf. They suggest that the geostrophic response seen over the deep shelf breaks down over the shallow shelf where frictional surface layers extend all the way to the bottom. More recently, upwelling regions on the eastern continental coasts have been identified. These include the coasts of Nova Scotia (Barth, 1994) and North Carolina (Austin, 1999).

The shelf waters off New Jersey offer a slightly different context to study upwelling. Most of the upwelling research outlined above has focused on regions with narrow continental shelves adjacent to very deep slope waters. The shelf waters off the coast of New Jersey, on the other hand, are characterized by a relatively wide continental shelf with slope waters about 200 km offshore. The strong summer stratification over the inner shelf complimented with generally alongshore winds make this region subject to frequent upwelling/downwelling events. Using 50 years of temperature data from Cape Cod to the Florida Keys, Walford and Wicklund (1968) describe a cold pool of water on the continental shelf. The cell, which is composed of water less than 8°C, is trapped below the thermocline by the highly stratified ocean during the spring and summer (Hicks and Miller, 1980). Hicks and Miller (1980) also observed that meteorological forcing, if persistent, has the potential to move the western boundary of the cell near shore and surface along the New Jersey coast. After the annual cycle, the largest fluctuation in sea surface temperature along the New Jersey coast is due to coastal upwelling/downwelling (Michael F. Crowley, pers. com.). While the upwelling observed

along the New Jersey coast may initially be uniformly distributed, after a period of days the cold water develops into distinct upwelling centers. Along the southern New Jersey coast, three upwelling centers develop about 50 km apart and are collocated with areas of recurrent bottom hypoxia (Glenn et al., 1996). Using numerical simulations, Song et al. (2001) and Glenn et al. (1996) show that these centers are the direct result of the interaction of surface wind forcing and local bathymetry. The centers are found both numerically and observationally to form on the northern side of topographic bumps and are composed of a cold eddy surrounded by an alongshore jet (Glenn et al., 1996; Song et al., 2001). One recurring center forms in our study site offshore of Tuckerton, New Jersey.

Previous research has looked at both the sea level and current response to small wind events in this region. For example, the sea level response resulting from a piling up of water at the New York Bight (NYB) apex propagated to the south in the form of a coastal-trapped wave (Yankovsky and Garvine, 1998). Yankovsky and Garvine (1998) went on to document the smaller scale interaction of the wind forced response and a coastal buoyant jet driven by fresh Hudson River outflow. Additional work by Münchow and Chant (2000) describe the vertical and horizontal variability of the sub-inertial response to an alongshore wind stress. Chant (2001) focuses on the vertical and horizontal structure of the near-inertial response to an alongshore wind stress. Using a High Frequency (HF) radar system, he describes the generation and evolution of energy within the near-inertial band (Chant, 2001).

The work described in this chapter focuses on the local response of the surface current fields to the local forcing. The study uses HF radar and a bottom-mounted ADCP

to describe the structure of the three-dimensional current response to local forcing. Since stratification varies significantly over seasonal scales, differences in the seasonal response reflect the importance of stratification to the local dynamics.

3.2 Methods

3.2.1 Instrumentation

The 25 MHz CODAR-type HF radar system deployed around Tuckerton consists of two remote sites located in Brant Beach and Brigantine, New Jersey (Figure 3.1). Using Doppler theory, each site measures the radial components of the ocean surface velocity directed toward or away from the site (Barrick, 1972; Barrick et al., 1977; Lipa and Barrick, 1996). Since the systems are using surface gravity waves to estimate these velocity components, the measured currents at this frequency are the weighted average of the currents within the upper one meter of the water column (Stewart and Joy, 1974). Radial component velocities measured at the two sites are combined into hourly total surface current maps. The dynamical study discussed here focuses on surface fields measured between May, 1999 and May, 2000. This time span was selected because it includes periods with both strongly stratified and mixed water columns and the stratified period is subject to several upwelling/downwelling events. In addition, the spring and summer of 1999 were anomalously dry, minimizing the freshwater contribution to the local circulation.

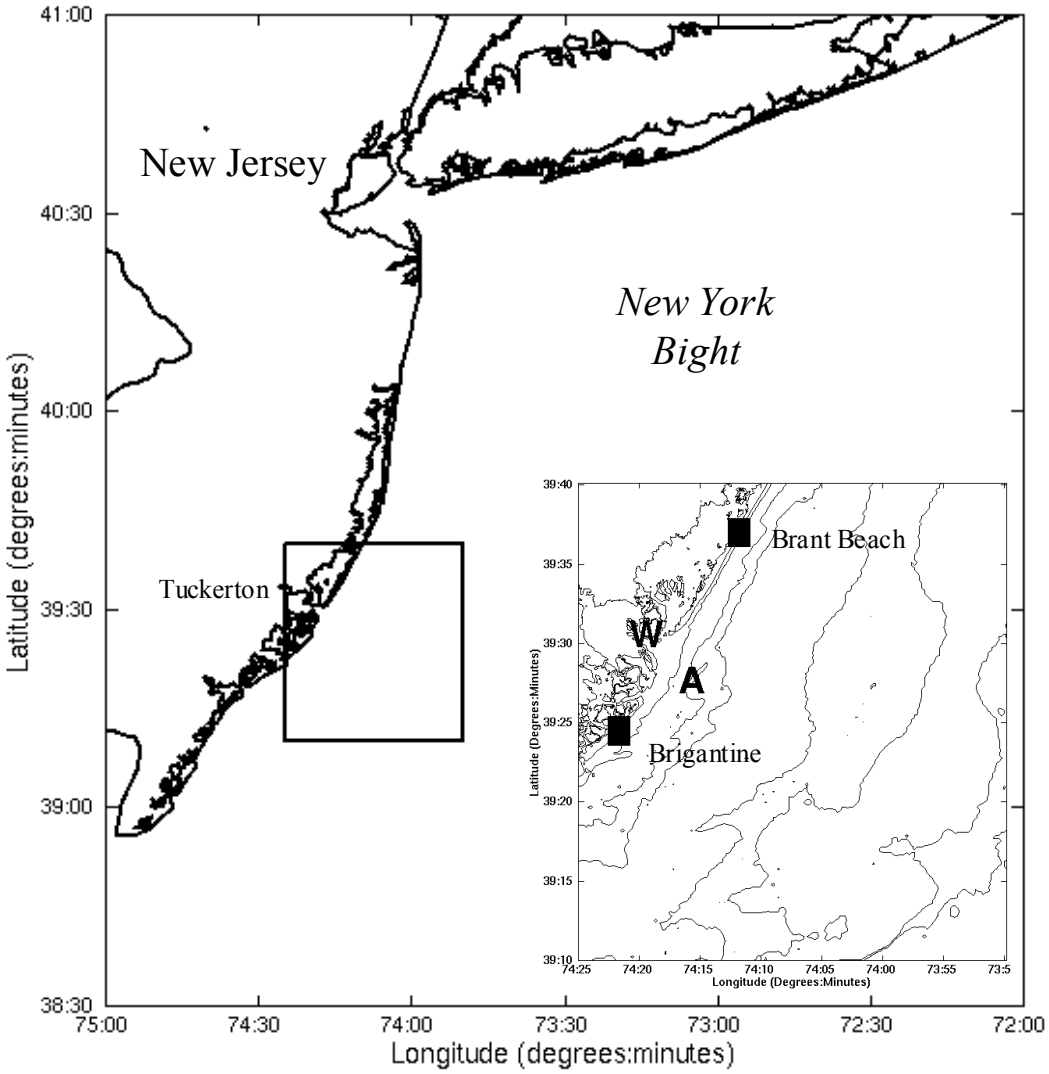

Figure 3.1. Map of the research area. The locations of the HF radar sites (black squares), ADCP (A), and met station (W) are shown in the inset. The 5m depth contours range from 5m nearshore to 35m offshore.

All data were processed by the optimal techniques described in Chapter 2. This includes (a) calibration with measured antenna beam patterns, (b) outlier elimination, and (c) an interpolation/smoothing algorithm. These techniques were demonstrated to produce the best comparison with concurrent *in situ* current meter data. The radial data was combined into hourly averaged total vector maps on a fixed grid. The entire record at each grid point was detided and low-pass filtered with a cutoff period of 30 hours. The surface data used in this study only included grid points that had at least 70% return over the annual record (Figure 3.2). The Geometric Dilution of Precision (GDOP) describes the spatial error associated with the geometric combination of the radial velocity measurements (Chapman et al., 1997). The specific GDOP for this HF radar system indicates that the geometric error increases rapidly toward the northwest and southwest corners of the coverage (Figure 3.2). Therefore the selected 70% coverage area is within GDOP values of 2.5 or less. In addition, tidal estimates were used to further verify the data quality of the selected grid. Since the tides do not vary significantly over the grid, the tidal ellipses calculated at each point should be consistent. The M2 tidal ellipses confirm that the less reliable data is collocated with larger GDOP (Figure 3.2). Since the data within the 70% contour has low GDOP and consistent tides, these data were used in the following analysis.

Complimentary *in situ* data was obtained from the Long-term Ecosystem Observatory (LEO-15) (Grassle et al., 1998; Glenn et al., 2000a; Schofield et al., 2001). Remotely-operated profilers that sample subsurface properties, including temperature, salinity, and pressure, and a bottom mounted Acoustic Doppler Current Profiler (ADCP) are located about 5 km offshore in 12 meters of water (Figure 3.1). A

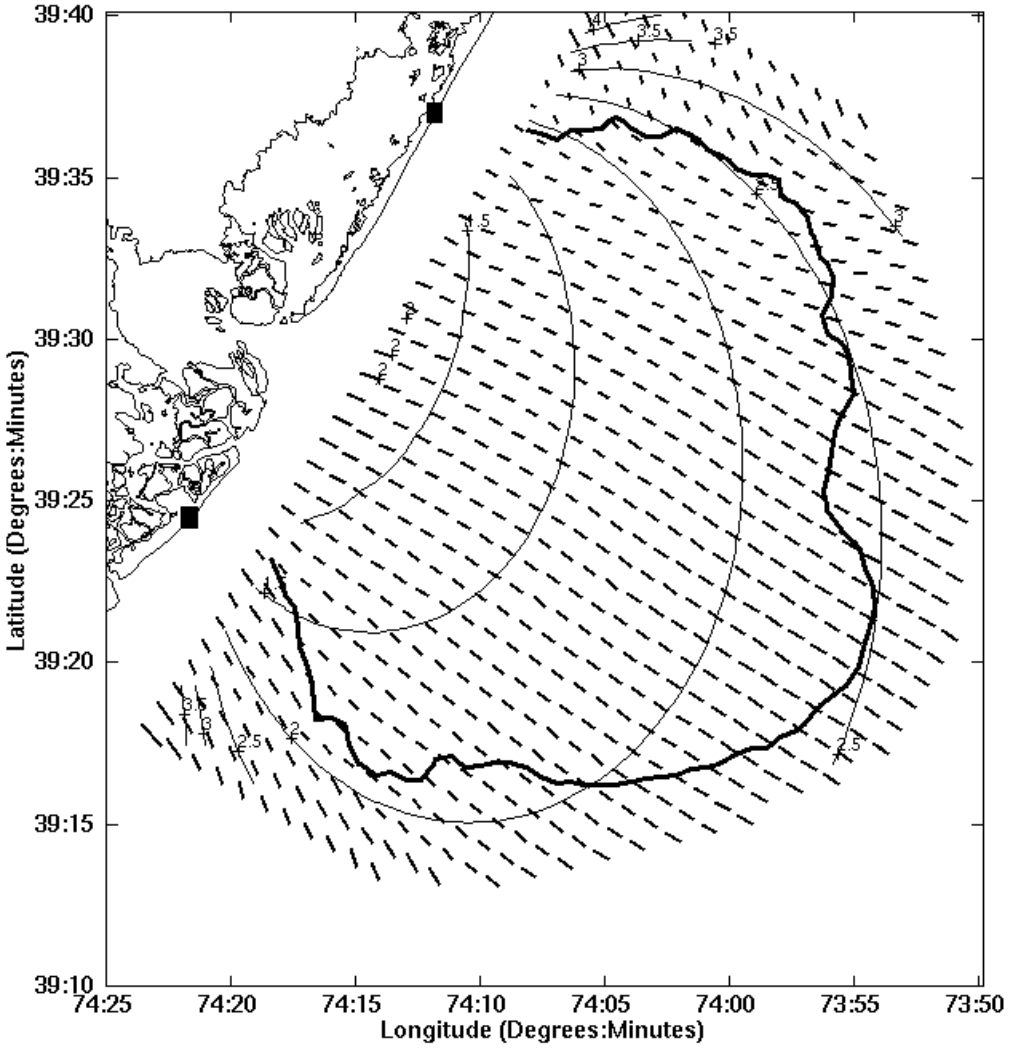

Figure 3.2. The GDOP contours (thin) of the HF radar system, tidal ellipses for the M2 constituent, and the 70 % coverage contour (thick) of the annual dataset.

meteorological tower at the Rutgers University Marine Field Station compliments the ocean observations with a suite of atmospheric data. Satellite imagery obtained from the Rutgers University Coastal Ocean Observation Lab provides continuous spatial coverage of sea surface temperature over the region. This particular study utilizes surface map time series of currents and temperature from the HF radar and satellites, bottom temperature and subsurface ADCP velocity profiles from LEO-15, and local wind measurements from the meteorological tower (Figure 3.3). The detided ADCP and wind data were centered averaged on the hour and filtered to match the HF radar sampling.

3.3 Results and discussion

3.3.1 Annual mean

The annual mean between May, 1999 and May, 2000 is a relatively weak flow generally alongshore toward the southwest (Figure 3.4). This flow is consistent with previous results discussed in the introduction. While the general flow is toward the southwest, the surface flow does follow the local topography. Upstream of a topographic bump in the middle of the data footprint, the alongshore flow veers offshore and accelerates, following the topography. Downstream of the topographic bump the flow returns to an alongshore direction. Even though the current measurements of an HF radar system are limited to the uppermost portion of the water column, the annual mean currents are influenced by the underlying topography on the order of the baroclinic Rossby radius, O(10km). The coastal ocean within the 30 m isobath is so shallow that the surface frictional layer could extend all the way to the bottom causing the surface and

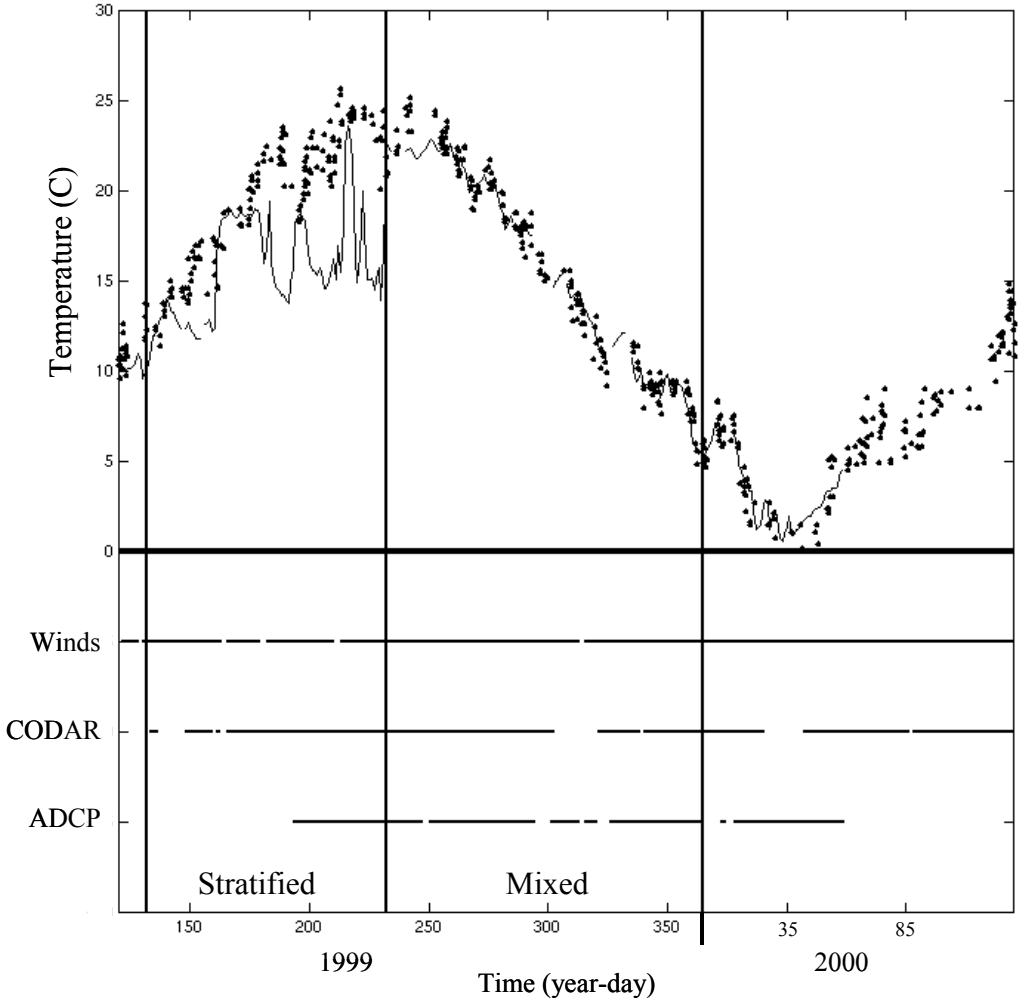

Figure 3.3. Time series of sea-surface temperature (dots), bottom temperature (solid line), and wind velocity, HF radar, and ADCP availability. The stratified and mixed regimes are delineated by vertical lines.

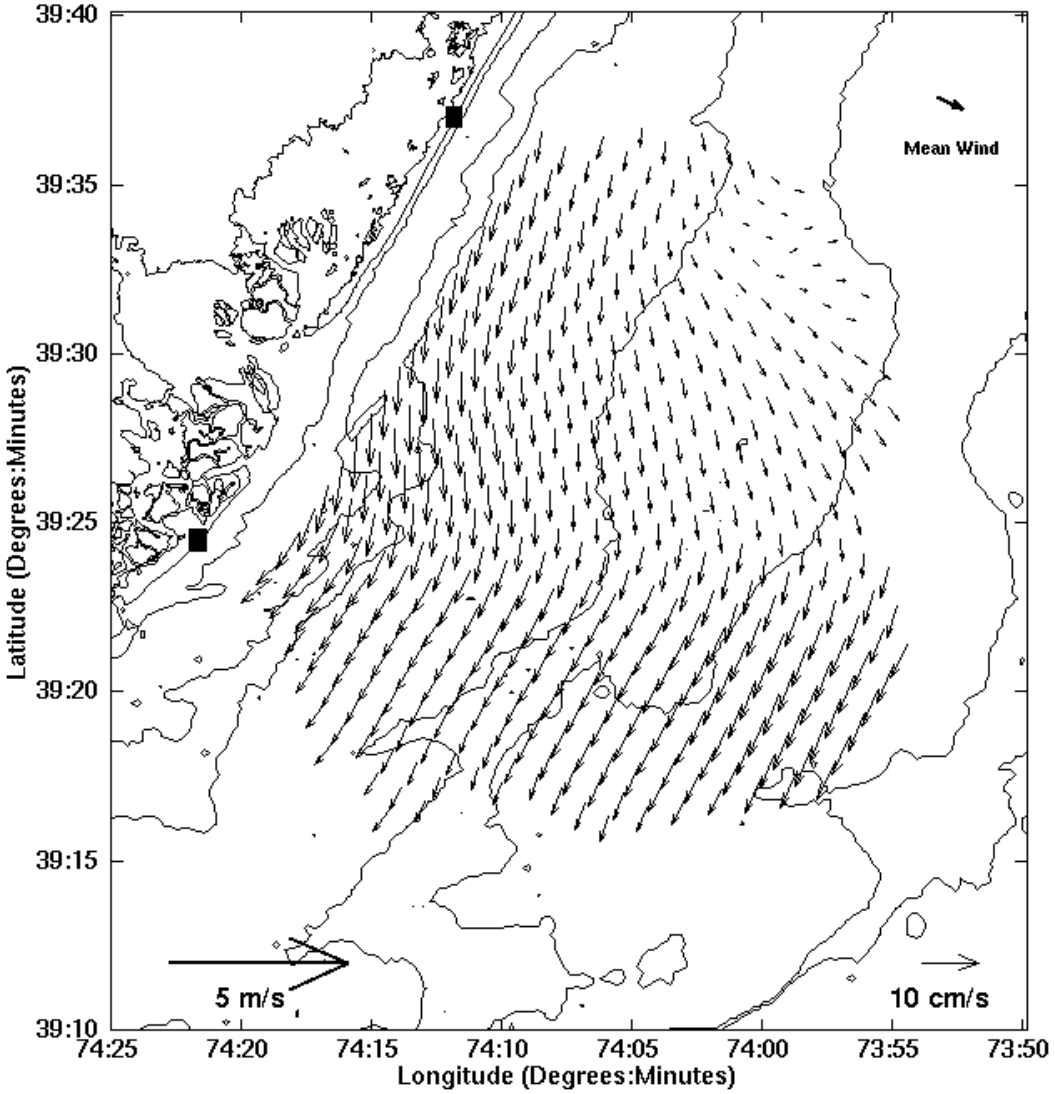

Figure 3.4. Annual mean currents measured between May, 1999 and May, 2000 with the HF radar system. The mean wind measured at the field station (upper right), the current scale (lower right), and wind scale (lower left) are also shown.

bottom boundary layers to interact. Here we discuss the role of stratification on the interaction and how this interaction influences the current response on seasonal time scales.

3.3.2 Mixed vs. stratified

To see the effect of stratification on the surface dynamics, the annual record was divided into two regimes, stratified and mixed. Using the surface temperature from a satellite mounted AVHRR sensor and the bottom temperature from the LEO CTD, the stratification was quantified. Within the annual data there are two clear regimes. One in which the bottom and surface temperatures are very similar (labeled mixed) and a second regime in which there is a significant temperature gradient between the surface and bottom (labeled stratified) (Figure 3.3). For this particular study, the stratified regime runs from year-day (yd) 133 to yd 231 and the mixed regime runs from yd 232 to yd 365. Both the current and wind data were divided into these two seasonal regimes so that the influence of stratification on the surface current fields could be studied.

3.3.3 Stratified regime

Forcing. The forcing during the summer stratified season is typically dominated by winds and buoyancy. Using the techniques described in Yankovski and Garvine (1998), the influence of buoyancy in the research area was determined by the magnitude of freshwater outflow leaving the Hudson River. Yankovski and Garvine (1998) cite an approximate 40-day lag between freshwater outflow at Watertown, New York and arrival off the southern New Jersey coast. Based on this 40-day lag, the brackets of Figure 3.5a

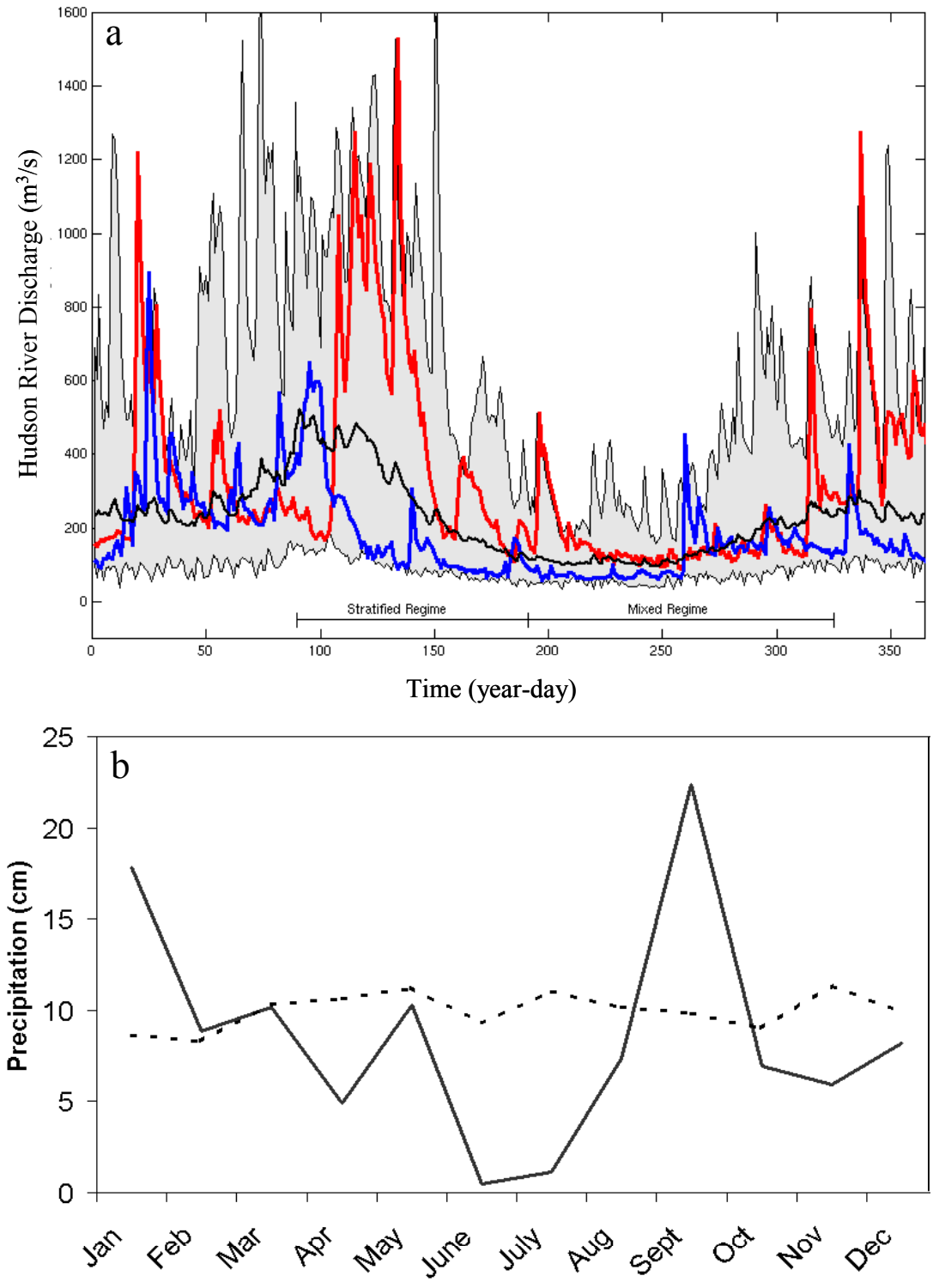

Figure 3.5. (a) The daily averaged Hudson River outflow for 1996 (red), 1999 (blue), and the 25 year mean (black) measured at a USGS station near Watertown, New York. The 25 year data envelope is shaded gray. (b) Average (dashed) and 1999 (solid) monthly New York City precipitation.

indicate the freshwater outflow at Watertown, NY that would influence the dynamics of the stratified regime. Unlike the spring of 1996 when Hudson River water influenced the local current structure (Yankovski and Garvine, 1998), the spring of 1999 did not have a significant outflow of fresh Hudson River water (Figure 3.5a). The average outflow affecting the circulation during the stratified regime is 187 m^3/s in 1999 and was 467 m^3/s in 1996. For the entire period influencing the stratified regime, the freshwater outflow is below the 25 year mean and often falls along the 25 year minimum. The average outflow affecting the circulation during the stratified regime is 187 m^3/s in 1999 and was 467 m^3/s in 1996. In addition, the precipitation data confirms that 1999 had generally below average rainfall with New York City precipitation below normal through much of the year (Figure 3.5b). Consequently, the summer stratification season of 1999 is likely to have a much smaller interaction between wind and buoyant forced responses than that observed in previous years.

The wind forcing during the stratified regime was strong and predominantly alongshore. A histogram of the low-passed filtered winds shows that the wind was mostly from the northeast (downwelling favorable) and the southwest (upwelling favorable) with the southwest winds dominating (Figure 3.6). The mean and standard deviation wind velocities from each direction indicates that the strongest velocities with the most variability were from the upwelling favorable direction. The forcing of the 1999 summer stratification season was dominated by an oscillation between upwelling and downwelling favorable winds.

Response. The current response during the stratified regime was separated into a mean and transient. The mean response is relatively weak across the field with an

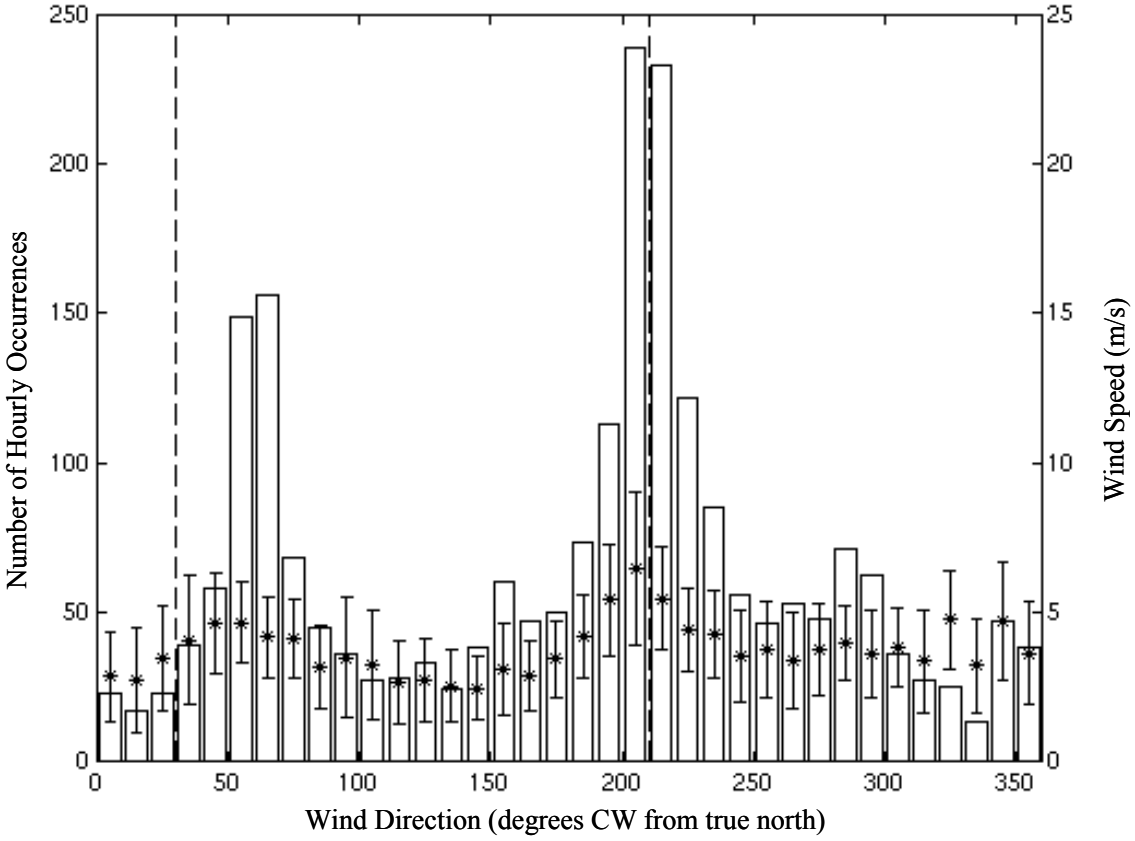

Figure 3.6. Histogram of wind forcing over the stratified regime. The mean (stars) and standard deviation (bars) of the wind velocity in each angular bin are also shown. The dashed lines indicate the bearing of the coast to the north and south.

average magnitude of 3.6 cm/s (Figure 3.7). The current direction varies significantly across the field and indicates a weak relationship with the mean southwesterly alongshore wind. The cyclonic rotation north of the bump hints at the interaction between surface currents and topography described by Glenn et al. (1996) and Song et al. (2001). The variance, on the other hand, is fairly uniform and much more energetic (Figure 3.8). The principle components are strongly rectilinear indicating a tendency for the variability to be aligned with the coast. This combined with a weak mean indicates that over the entire stratified regime the response is highly variable and tends to be oriented along the coast.

The complex correlation between the local wind and the current response at each HF radar grid point shows a very strong correlation with a mean of 0.84 and a standard deviation of 0.03 across the entire field (Figure 3.9). In addition to the magnitude, the vectors indicate the current direction with the highest correlation to the wind. The vectors at each gridpoint, plotted with respect to the mean stratified wind, indicate that over the entire field the most correlated current is shifted to the right of the wind. This offset fluctuates slightly across the field with a maximum of 23 degrees near the center of the field and a minimum of 4 degrees near the northern edge. The vertical variability of this correlation was determined from the ADCP. As expected the surface currents are more correlated with the wind than the bottom currents (Figure 3.10). Once again, the phase offset between the wind and current indicates that the highest correlated currents are shifted to the right of the wind at the surface and rotate to the left with depth. The spiral is a fairly typical picture of an upwelling/downwelling regime in which the surface layer moves to the right of the forcing and the bottom layer moves to the left.

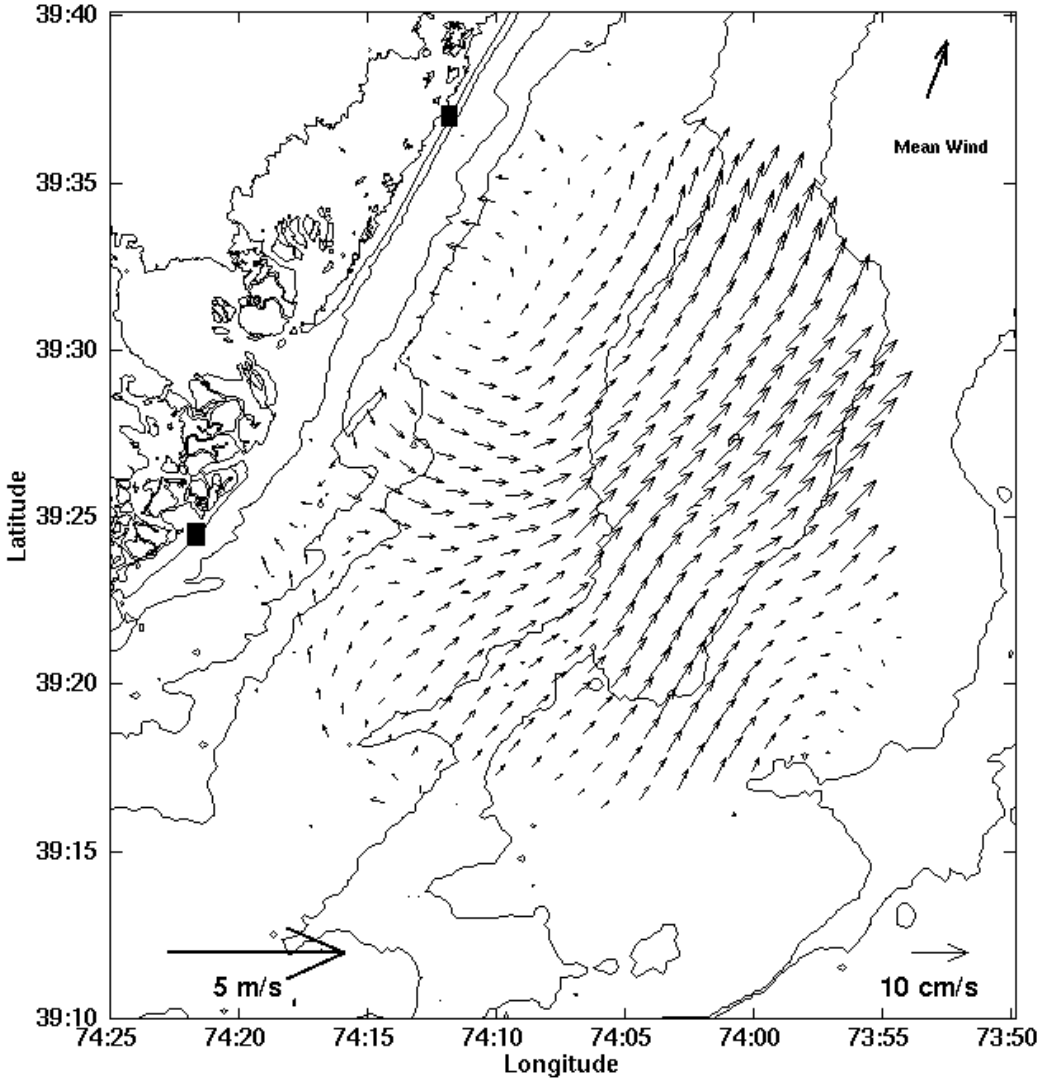

Figure 3.7. Mean stratified regime current response. The mean stratified wind measured at the field station (upper right), the current scale (lower right), and wind scale (lower left) are also shown.

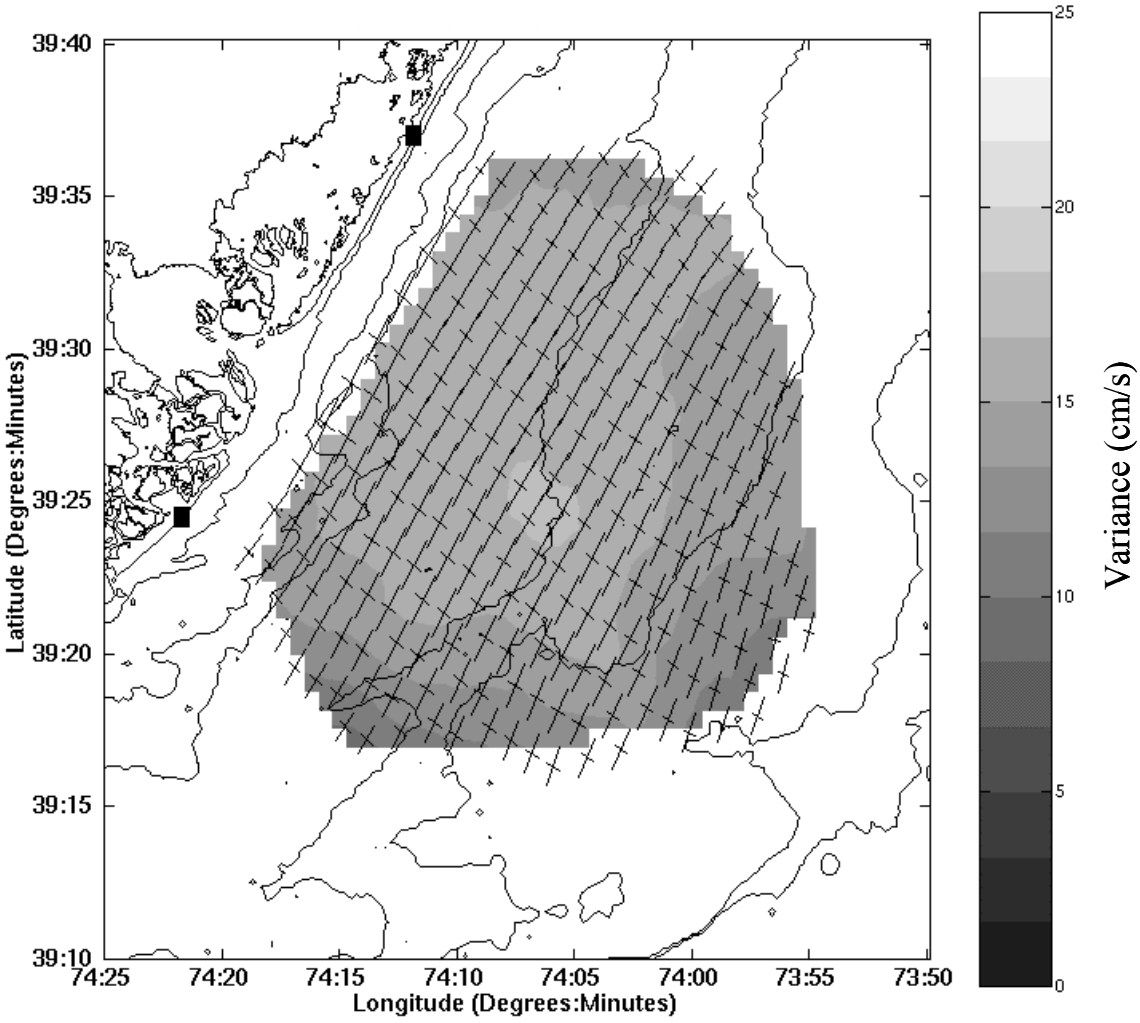

Figure 3.8. Principle components of the stratified regime transient response.

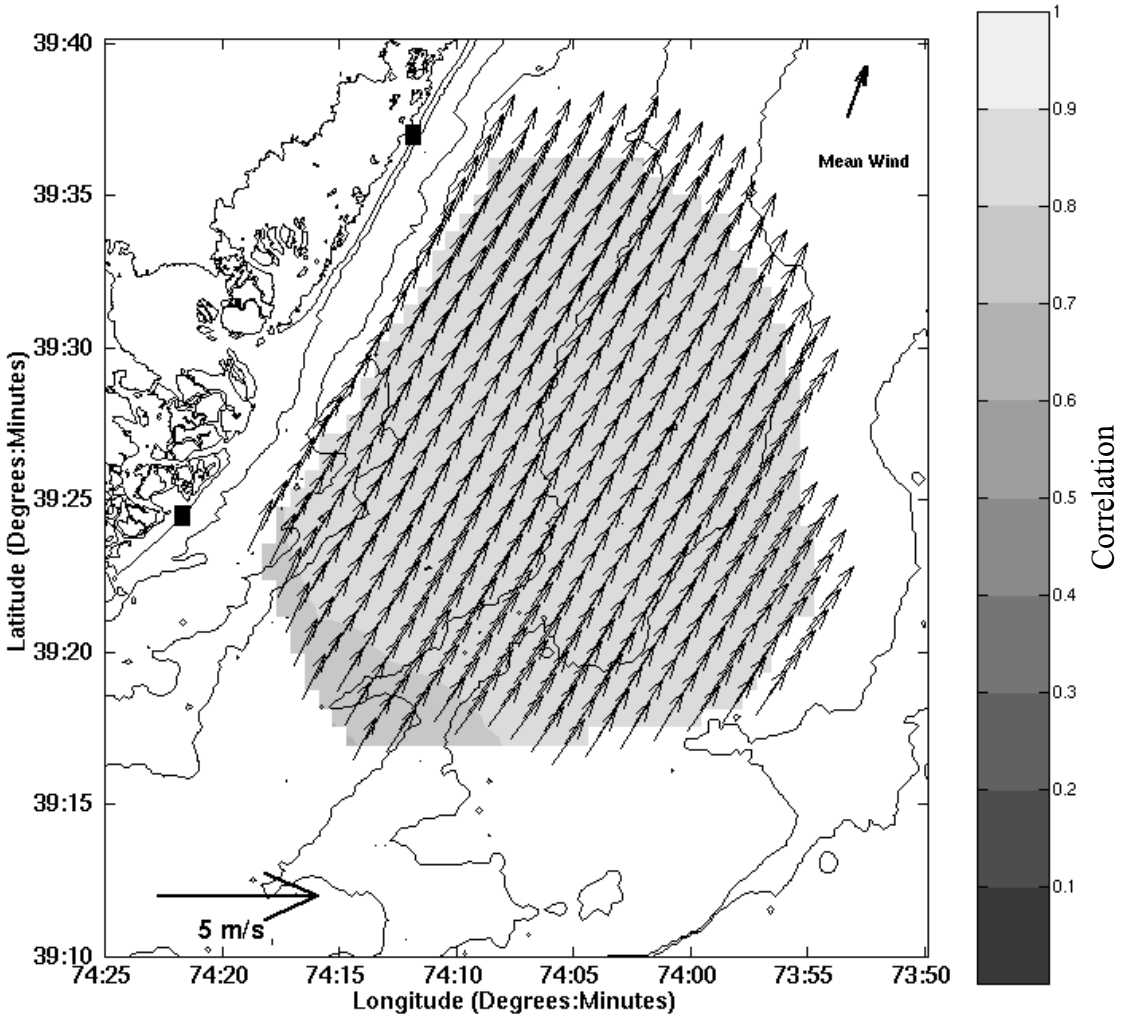

Figure 3.9. Complex correlation of the stratified regime transient response with the local winds. The angle between the mean wind (upper right) and each grid point (black vectors) indicates the offset between the highest correlated current and wind.

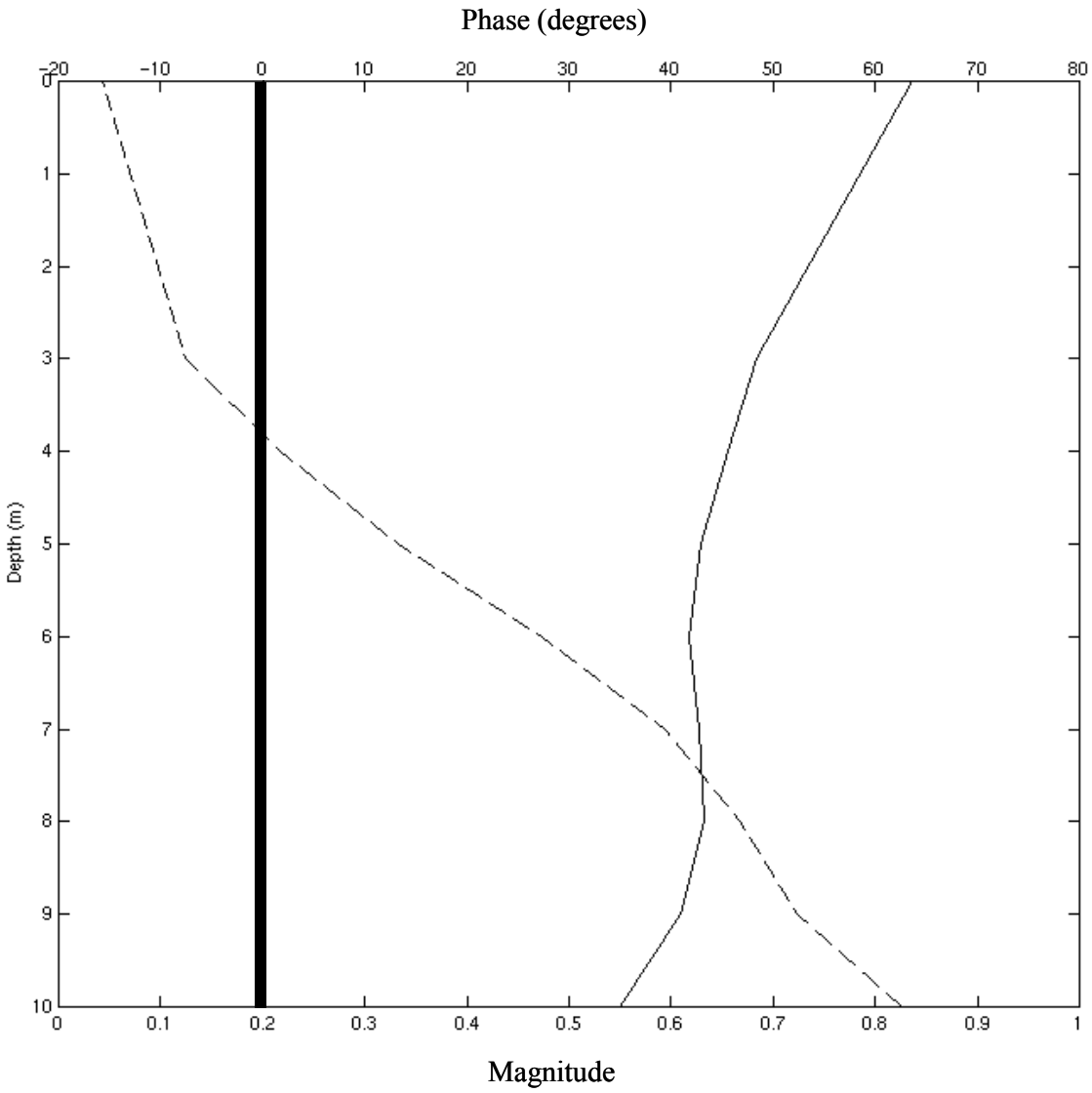

Figure 3.10. Magnitude (thin) and phase (dashed) of the complex correlation between the vertical current profile and the local wind forcing during the stratified regime. Negative phase indicates that the highest correlated current is to the right of the wind. The heavy line indicates zero phase.

A linear correlation was used in this analysis to identify that component of the observed flow most correlated with the wind. The complex correlation between the wind and each HF radar grid point indicates the angular offset between the highest correlated wind and current response. At each point this offset was used to obtain the best relationship between the local wind and current from the highest correlated direction. After the wind was rotated according to the complex correlation, a best-fit linear regression was used to describe the relationship between the wind and current for each direction so that:

$$u_{cor}(x,y,t) = slope_x(x,y) * u_{wind}(t) \tag{3.1}$$

$$v_{cor}(x,y,t) = slope_y(x,y) * v_{wind}(t) \tag{3.2}$$

where $slope_x$, and $slope_y$ are the slopes of the linear fit for the east and north current components, respectively. u_{cor} and v_{cor} are the predicted east and north components of the wind correlated current. If this correlated response is subtracted from the total response, the residual will be the component of the flow uncorrelated with the wind.

$$u_{total} = u_{cor}(x,y,t) + u_{uncor}(x,y,t) \tag{3.3}$$

$$v_{total} = v_{cor}(x,y,t) + v_{uncor}(x,y,t) \tag{3.4}$$

The magnitude of this residual current for each directional component, u_{uncor} and v_{uncor}, is a function of the scatter about the linear fit (Figure 3.11). The further an individual point falls from the best-fit line, the smaller the contribution of the wind to its measured

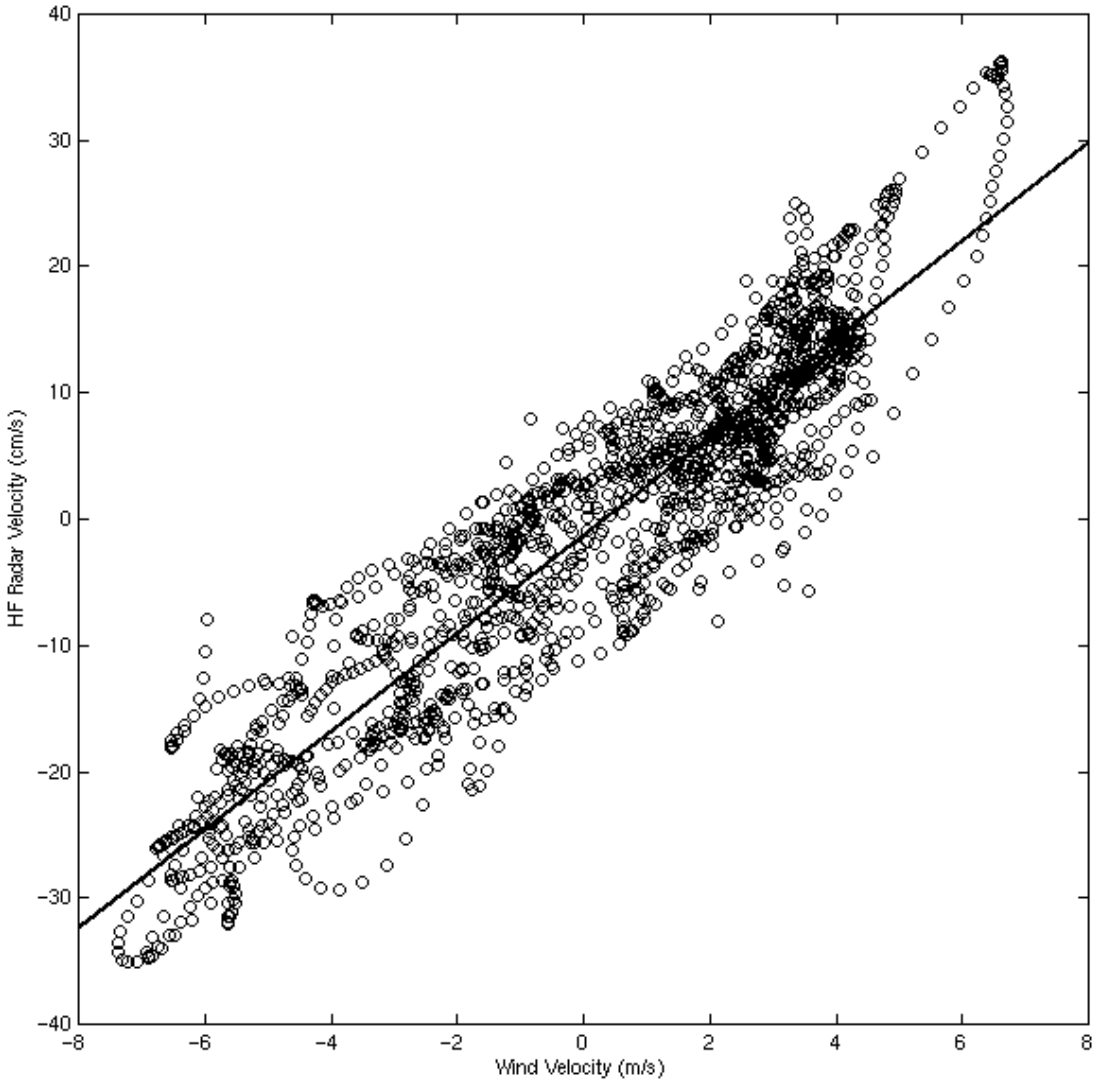

Figure 3.11. Scatter plot of wind and surface velocity for a single HF radar grid point. The line indicates the slope used to predict the wind correlated component of the flow.

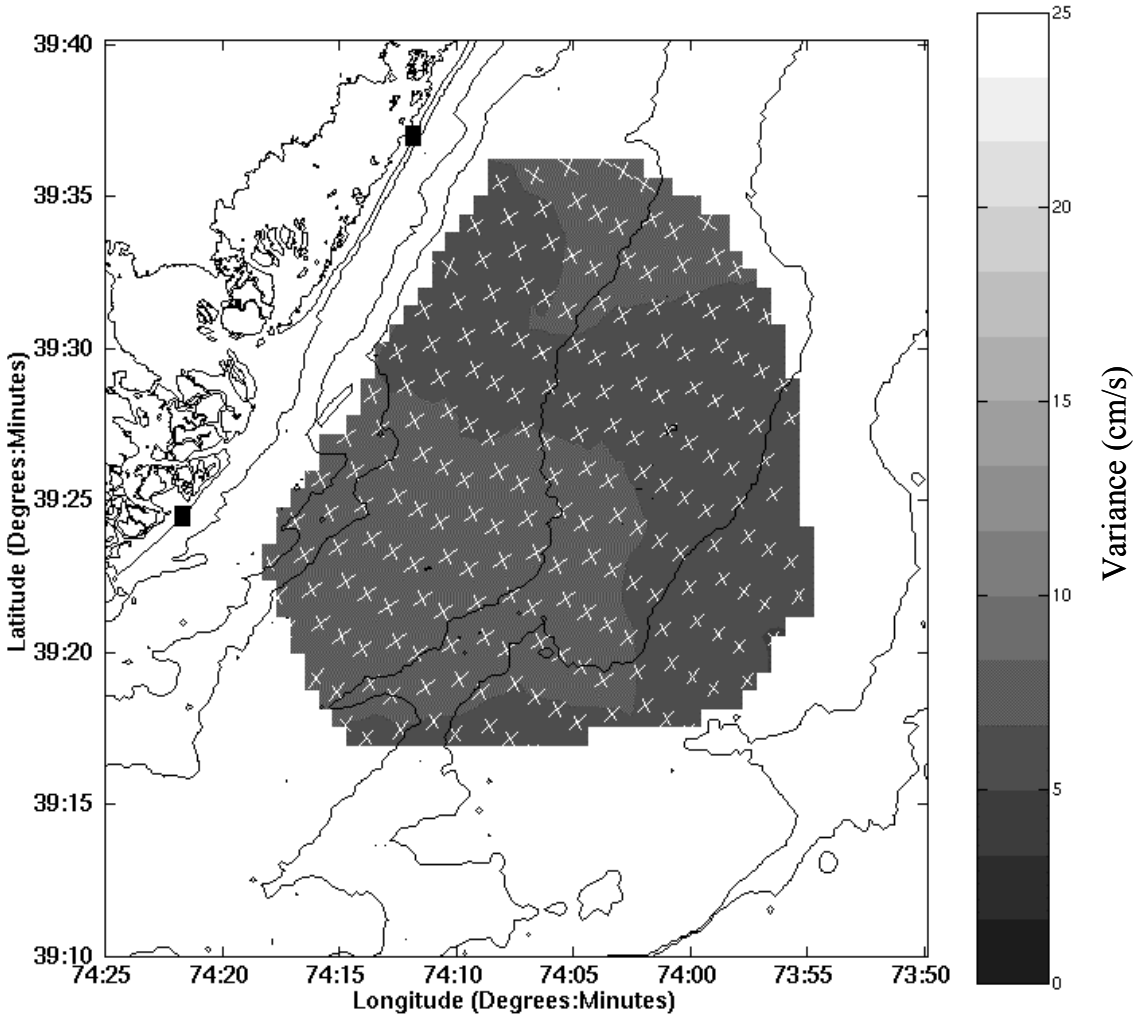

Figure 3.12. Residual component of the stratified regime transient response.

velocity. Typical correlation between the wind and the residual current are all below 0.2 across the field indicating that equation 3.1 and 3.2 does describe the wind-correlated component of the total response. Based on this technique, the variance of the residual current is significantly less than the total variance (Figure 3.12 and 3.8). Therefore, the wind forcing accounts for the majority of the variability seen in the stratified transient response. The complex correlation and weak residual variance indicate a tightly linked system between the wind forcing and the current response. Since the orientation of the forcing and response are both along the coast, a better representation of the current structure related to the local forcing can be achieved by separating the stratified regime into upwelling and downwelling regimes.

3.3.3.1 Upwelling regime

Unlike the seasonal stratified mean, the upwelling mean is very strong and, for most grid points, shifted to the right of the mean upwelling wind (Figure 3.13). This mean response is clearly indicative of an upwelling favorable wind stress. The spatial variability of this field is more evident when the spatial mean is subtracted from the temporal mean of each gridpoint (Figure 3.14). The spatial structure of the response is very complicated with eddy-like features and strong horizontal shears. North of the bump a cyclonic eddy indicates the influence of the underlying topography on the mean response. Here the mean is steered offshore over the bump and rotates counterclockwise north of the bump. The eddy location coincides with numerical results in which the upwelling center north of the bump is characterized by a cyclonic eddy (Glenn et al., 1996). This feature coincides with the cyclonic circulation in the overall mean of the

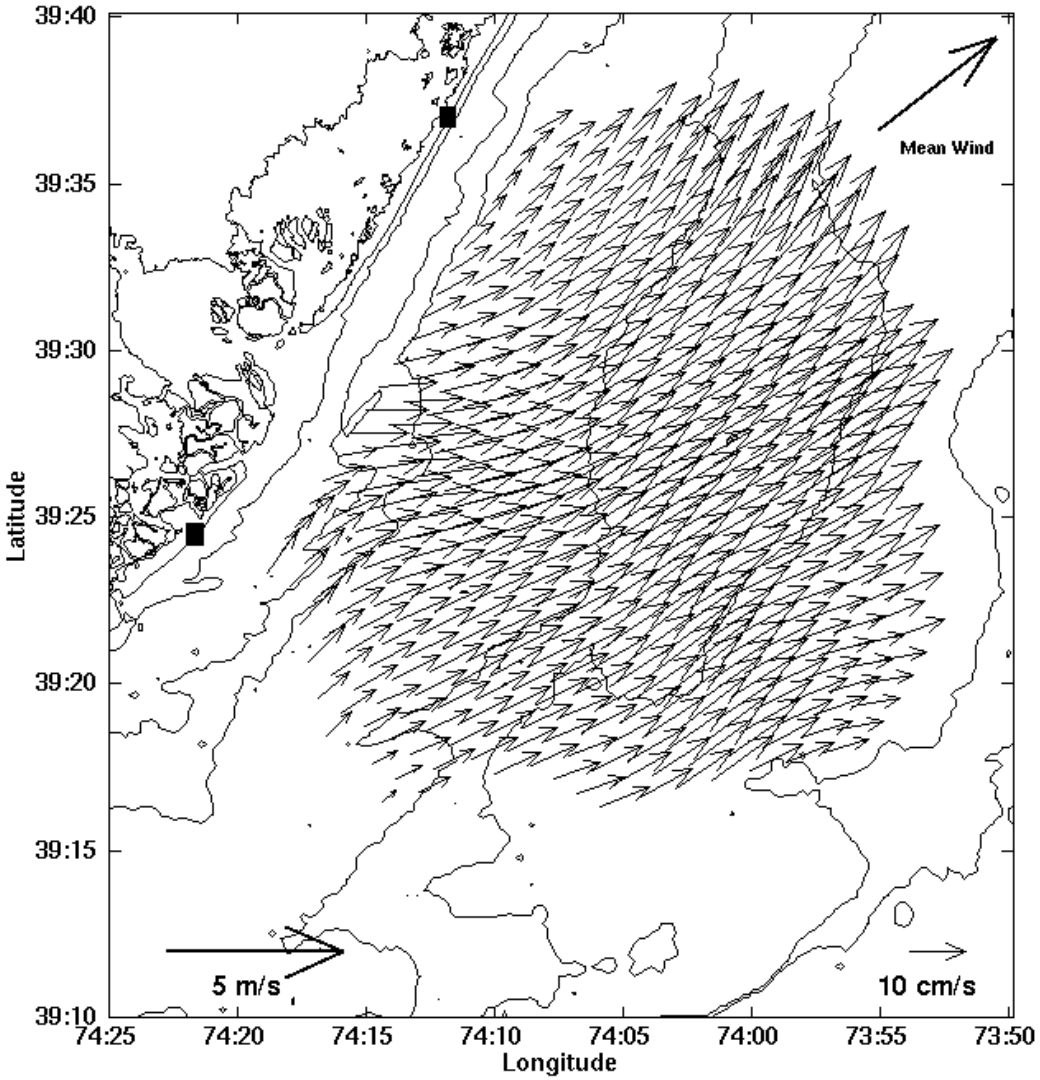

Figure 3.13. Mean upwelling regime response. The mean upwelling wind measured at the field station (upper right), the current scale (lower right), and wind scale (lower left) are also shown.

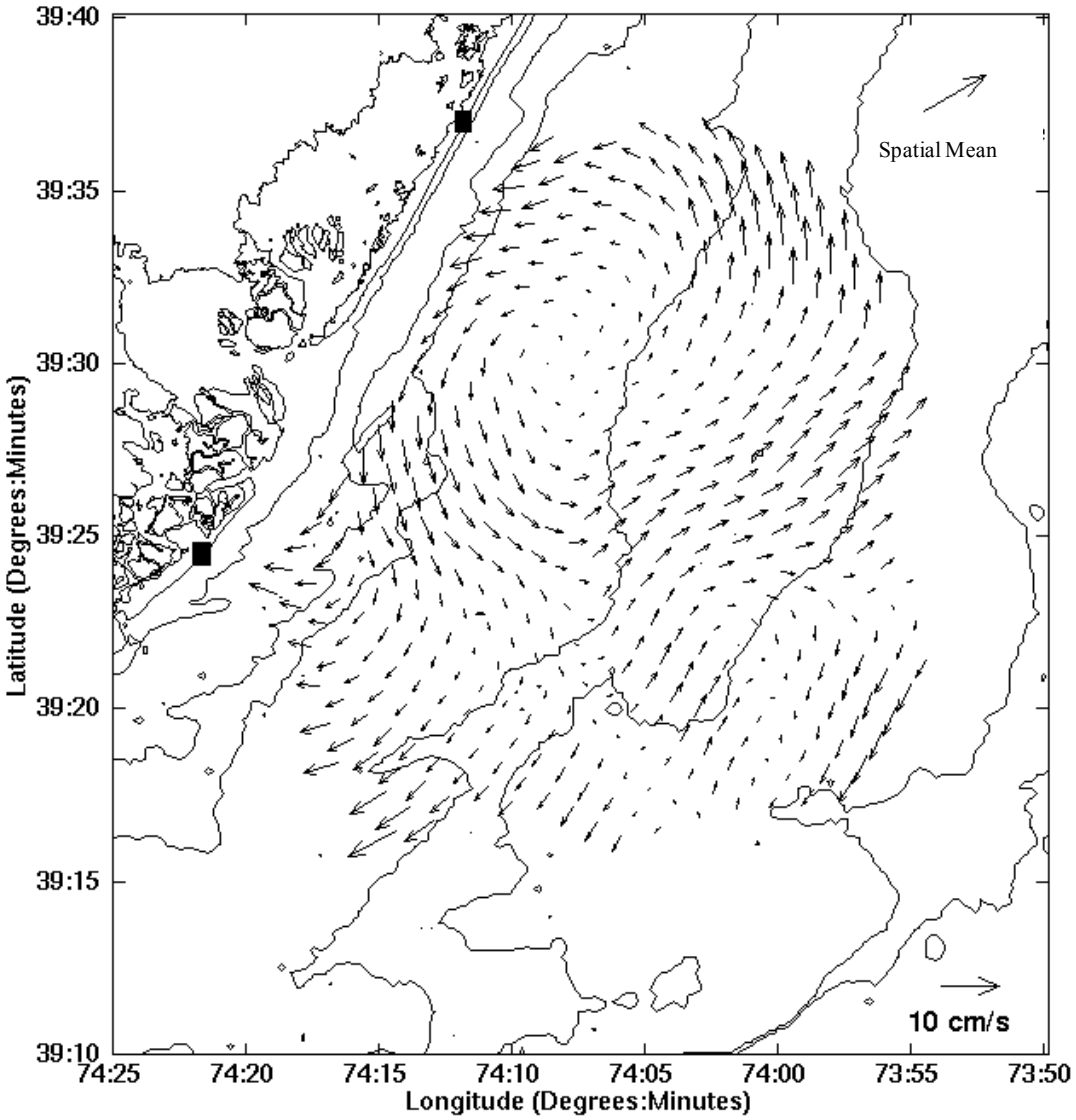

Figure 3.14. Spatial structure of the mean upwelling response. The vector field is the difference between the temporal mean at each grid point and the spatial mean (upper right).

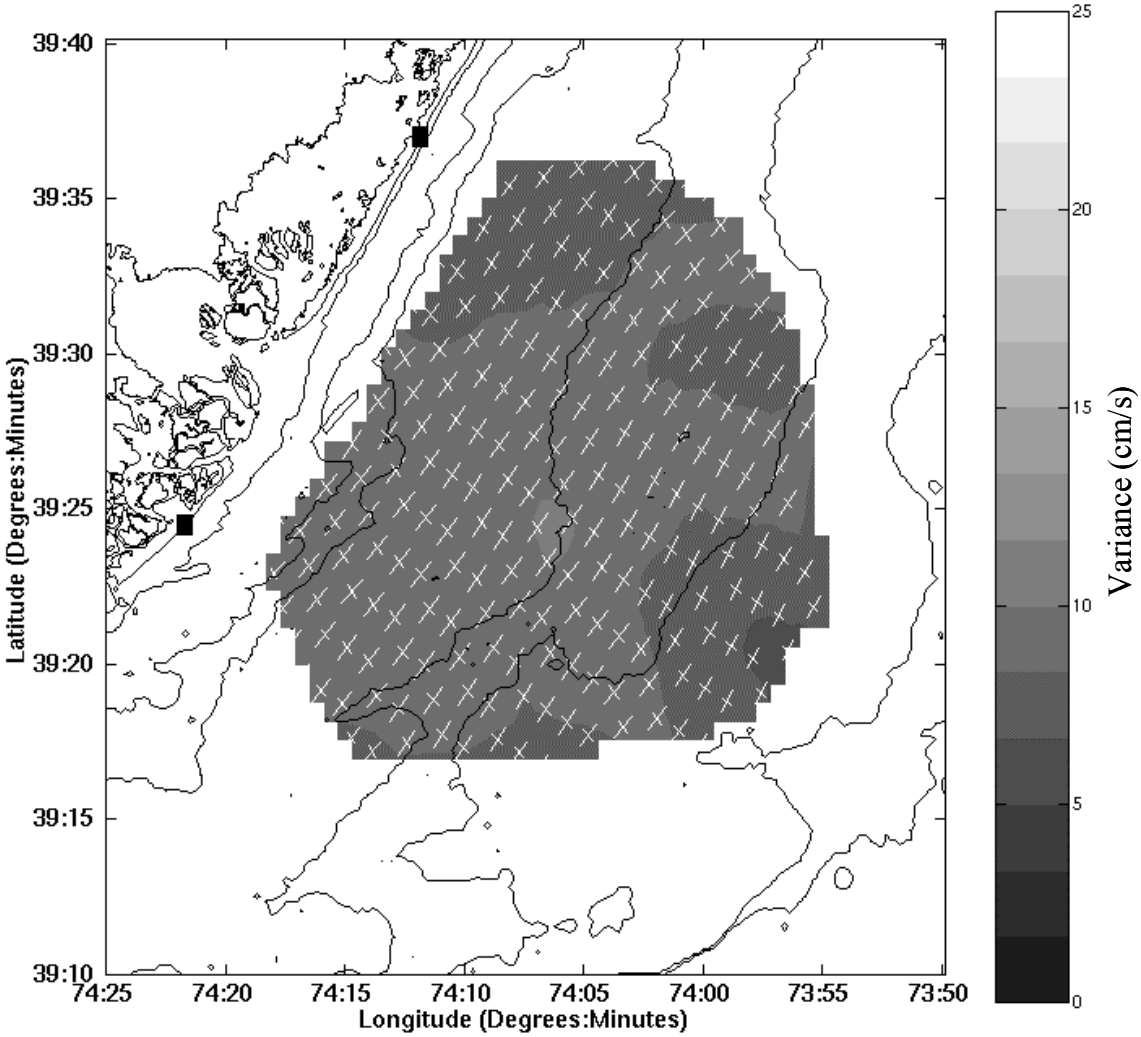

Figure 3.15. Principle components of the upwelling regime transient response.

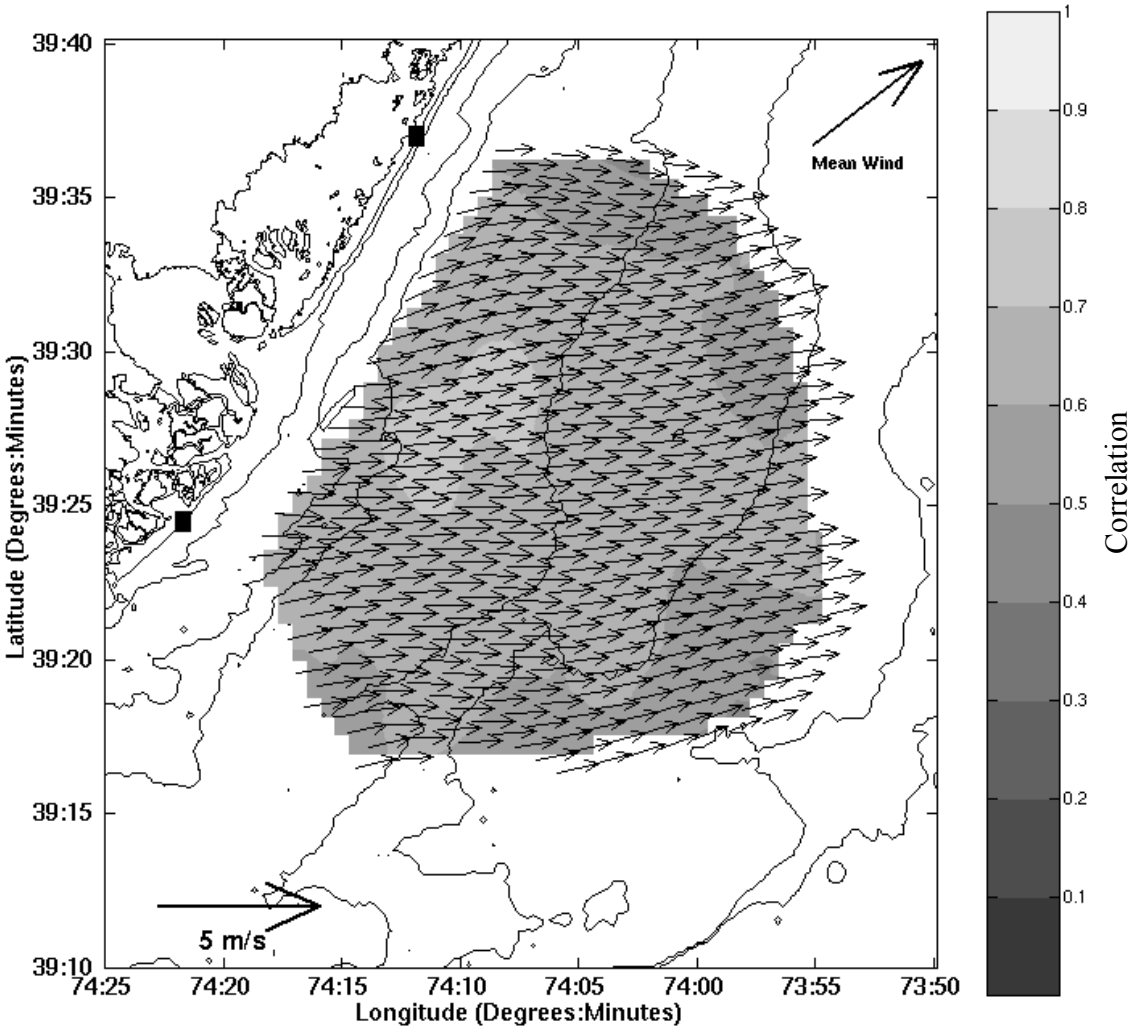

Figure 3.16. Complex correlation between the upwelling regime transient response and the local winds. The angle offset between the mean wind (upper left) and each grid point (black vectors) indicates the angle between the highest correlated current and winds.

stratified regime (Figure 3.7). Unlike the stratified variance, the upwelling variance is much weaker than the mean, indicating that this response is fairly steady (Figure 3.15).

The complex correlation shows that the strongest relationship between the wind and response is confined to the nearshore region of the field, just north of the bump (Figure 3.16). Sea Surface Temperature (SST) (Glenn et al., 1996) maps and numerical model simulations (Song et al., 2001) show that the surface temperature structure seen during a typical upwelling event consists of cold eddy north of the bump and warm water offshore separated by a strong front. A strong northward flowing jet is observed on the offshore side of the front. Since the correlation scale matches the typical offshore extent of the cold eddy, the surface currents inside the front are more correlated with the wind than the northward flowing jet outside the front.

3.3.3.2 Downwelling regime

The mean surface response to downwelling favorable winds is again relatively strong (Figure 3.17). The spatial structure of the mean can be separated into two regions, nearshore and offshore. The nearshore response is along-shore toward the south and oriented to the left of the wind (Figure 3.17). The offshore response, no longer oriented with the coast, is more closely aligned with the wind. The horizontal shear of the downwelling regime is more uniform than the upwelling regime and appears to be related to the stratification (Figure 3.18). During a typical downwelling event, the thermocline intersects the bottom. Offshore of this intersection the water column remains stratified and onshore of the intersection the water column becomes mixed. According to the downwelling mean, the response of the stratified offshore region is weaker and aligned

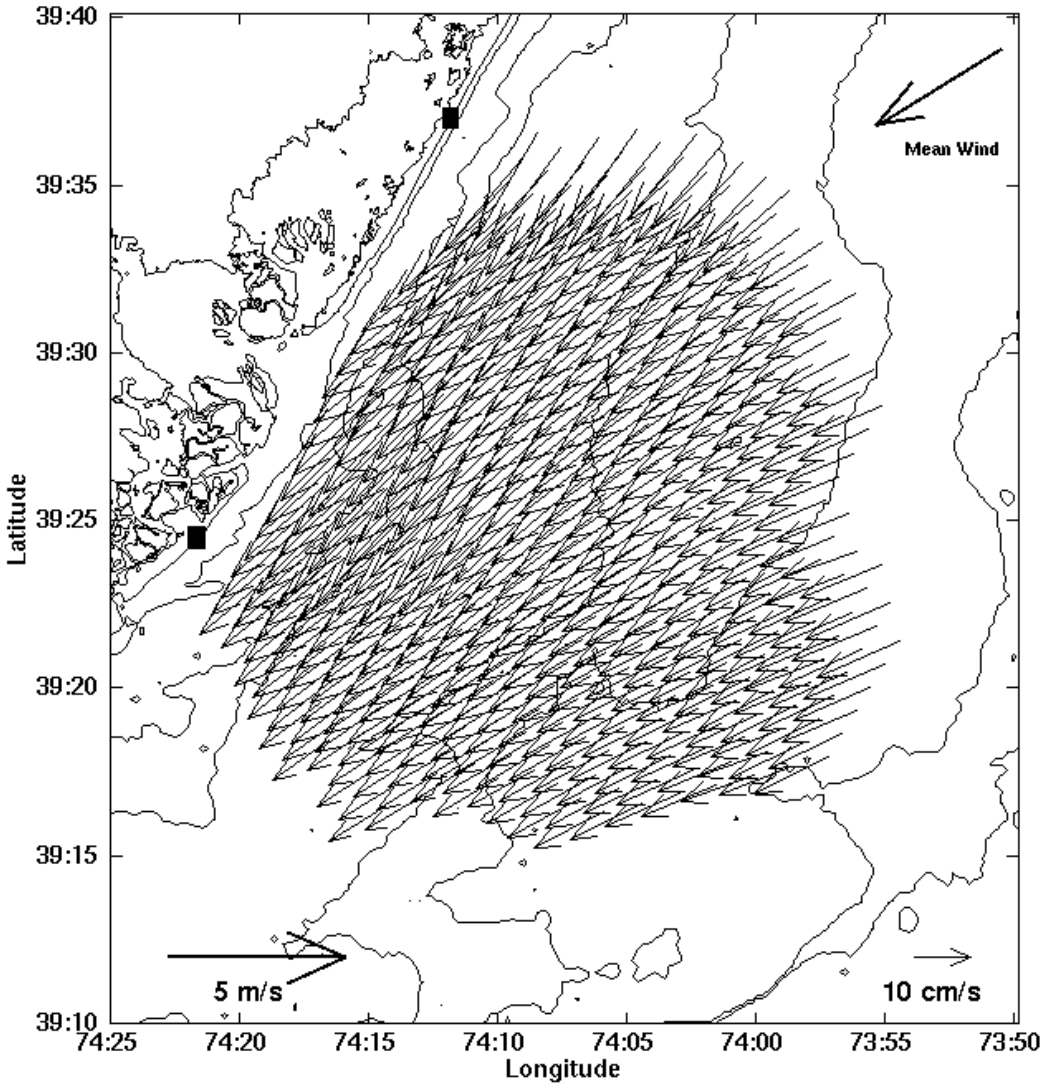

Figure 3.17. Mean downwelling regime response. The mean downwelling wind measured at the field station (upper right), the current scale (lower right), and wind scale (lower left) are also shown.

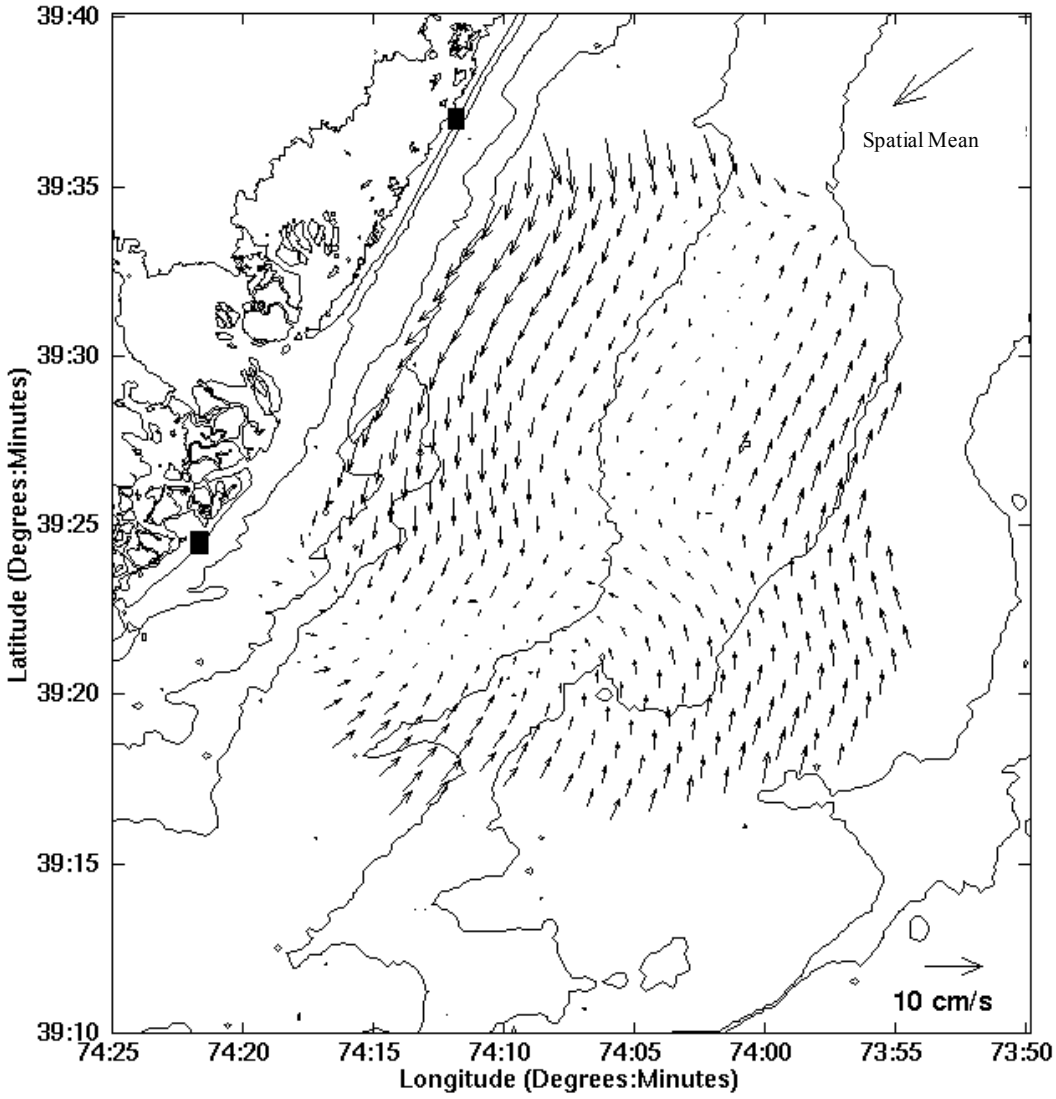

Figure 3.18. Spatial structure of the mean downwelling response. The vector field is the difference between the temporal mean at each grid point and the spatial mean (upper right).

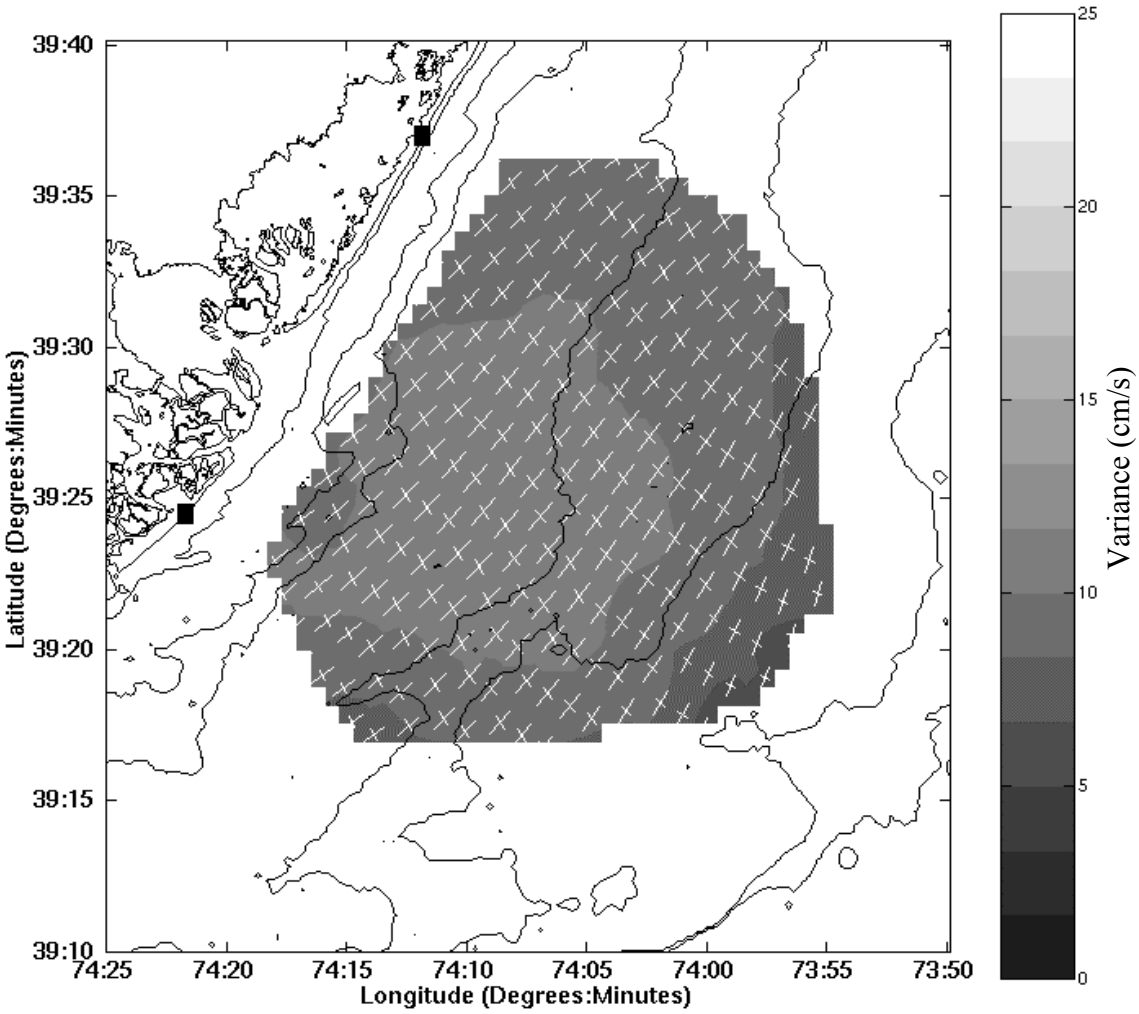

Figure 3.19. Principle components of the downwelling regime transient response.

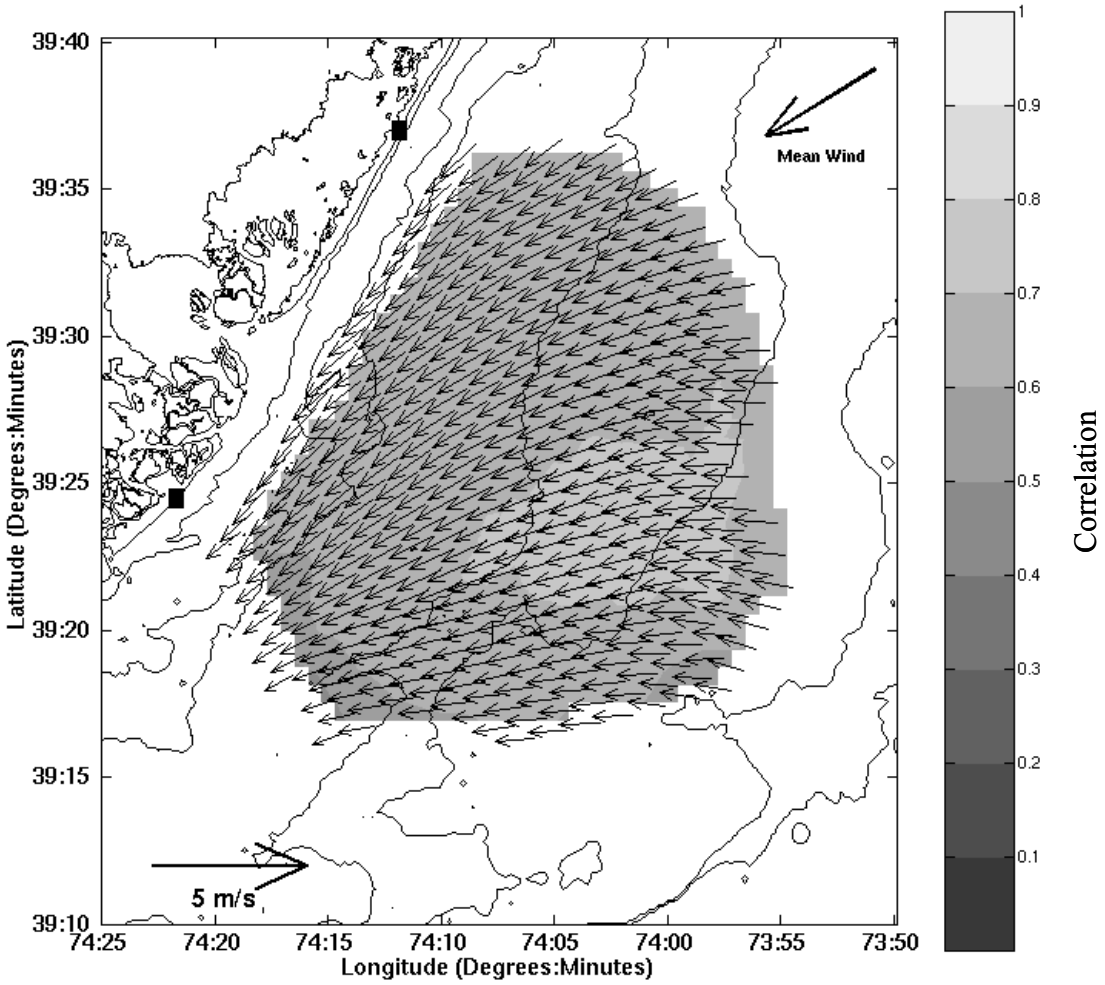

Figure 3.20. Complex correlation between the downwelling regime transient response and the local winds. The angle offset between the mean wind (upper left) and each grid point (black vectors) indicates the angle between the highest correlated current and winds.

with the wind and the nearshore response of the mixed water column is stronger and aligned with the coast. Unlike the stratified mean and similar to the upwelling response, the downwelling variance is relatively weak indicating another relatively steady response (Figure 3.19).

The complex correlation shows that the highest wind correlation during downwelling favorable winds is further offshore than that observed during upwelling favorable winds (Figure 3.20). Therefore, the surface currents over the stratified water column are more tightly linked to the wind than the nearshore currents of the mixed water column. The downwelling response can best be described as a steady flow in which the weaker offshore currents of the stratified water column are more closely aligned with the wind and the stronger nearshore currents of the mixed water column are more closely aligned with the coast.

Both the downwelling and upwelling regimes indicate that the current response during the stratified regime is relatively steady with strong means and weak variability. This response is influenced by the local topography during upwelling events and stratification during downwelling events.

3.3.4 Mixed regime

Forcing. The buoyancy forcing during the mixed regime was more episodic than observed during the stratified regime. The peak seen around yd 260 in the Watertown outflow and the September peak in precipitation (Figure 3.5) are from a large rain event associated with the passing of tropical storm Floyd (Chapter 4). Once again throughout most of the period influencing the mixed regime dynamics, the outflow is below the 25

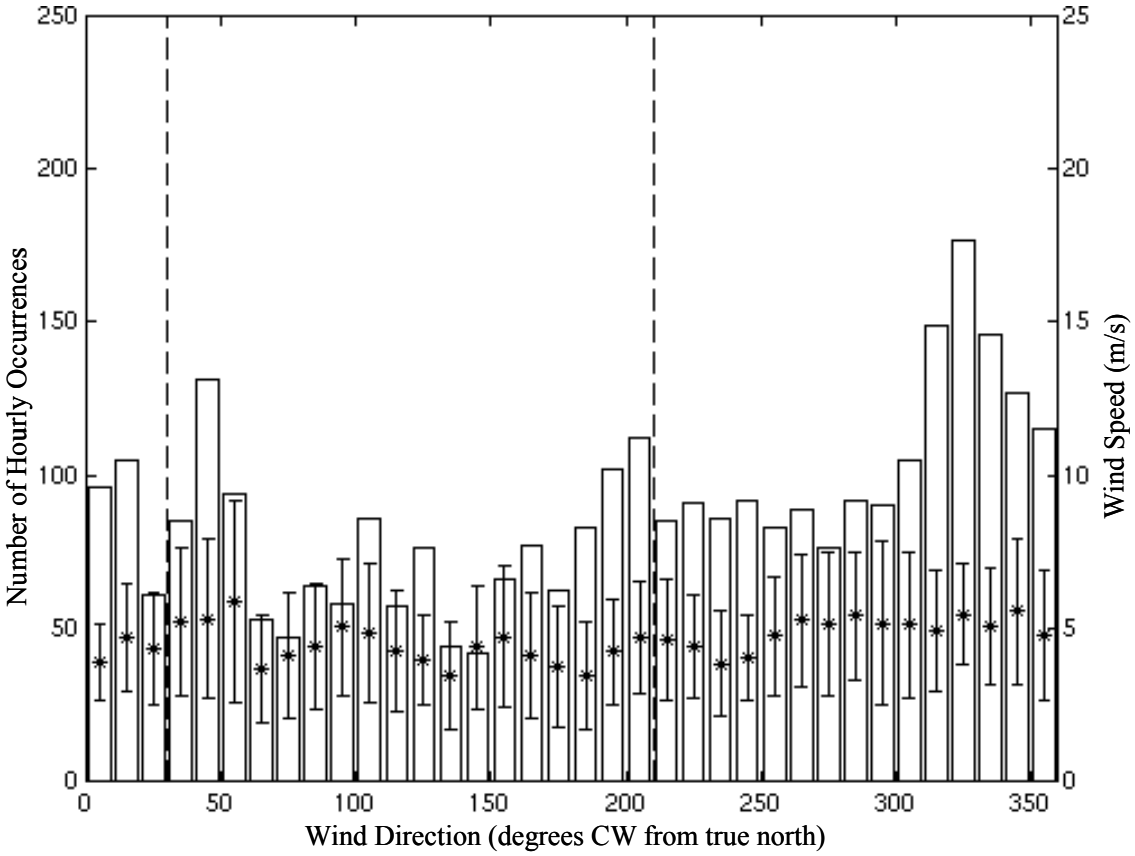

Figure 3.21. Histogram of wind forcing over the mixed regime. The mean (stars) and standard deviation (bars) of the wind velocity in each angular bin are also shown. The dashed lines indicate the direction of coast to the north and south.

year mean and often near the 25 year minimum. While Floyd was a significant freshwater event, over the seasonal temporal scale studied here, the influence of the buoyancy is again relatively low. The wind forcing throughout the mixed regime was much more evenly distributed than observed during the stratified regime with a peak in the northwest direction (Figure 3.21). This is in agreement with the climatology described by Moores et al. (1976) in which the winds measured over much of the year tend to be from the northwest. The mean and standard deviation of the wind measured in each directional bin show that the forcing is stronger than seen in the stratified regime and more variable (Figure 3.21 and 3.6).

Response. The mean response closely resembles that seen in the annual mean (Figures 3.4 and 3.22). The currents follow the local topography north of the bump and turn more alongshore south of the bump. The magnitude of the flow is on the order of 4.5 cm/s. The spatial structure of the variance also reflects the underlying topography with an energy maximum centered over the bump (Figure 3.23). The mean and transient indicate that the response is relatively steady around the bump and much more variable over the bump.

The wind forcing and response are less correlated than that observed during the stratified regime with a mean of 0.69 and a standard deviation of 0.03 across the field. The vectors indicate that the angular offset between the wind and these highest correlated currents is now shifted to the left of the wind with a mean of 14.9 degrees and a maximum of 31 degrees nearshore (Figure 3.24). The vertical structure of the correlation at the ADCP is highest at the surface and decreases with depth (Figure 3.25). The angular shear from surface to bottom is relatively small confirming that the system is

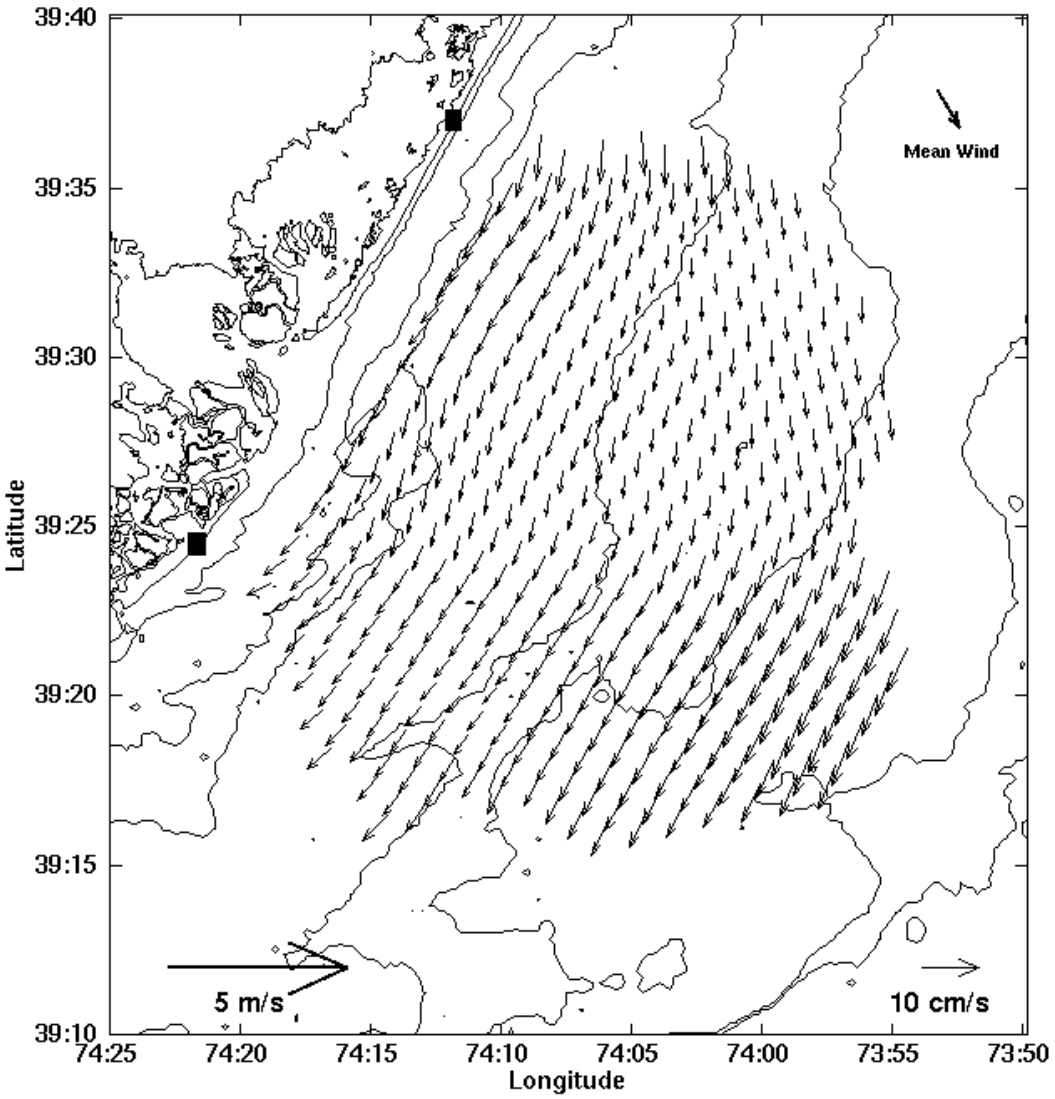

Figure 3.22. Mean mixed regime response. The mean mixed wind measured at the field station (upper right), the current scale (lower right), and wind scale (lower left) are also shown.

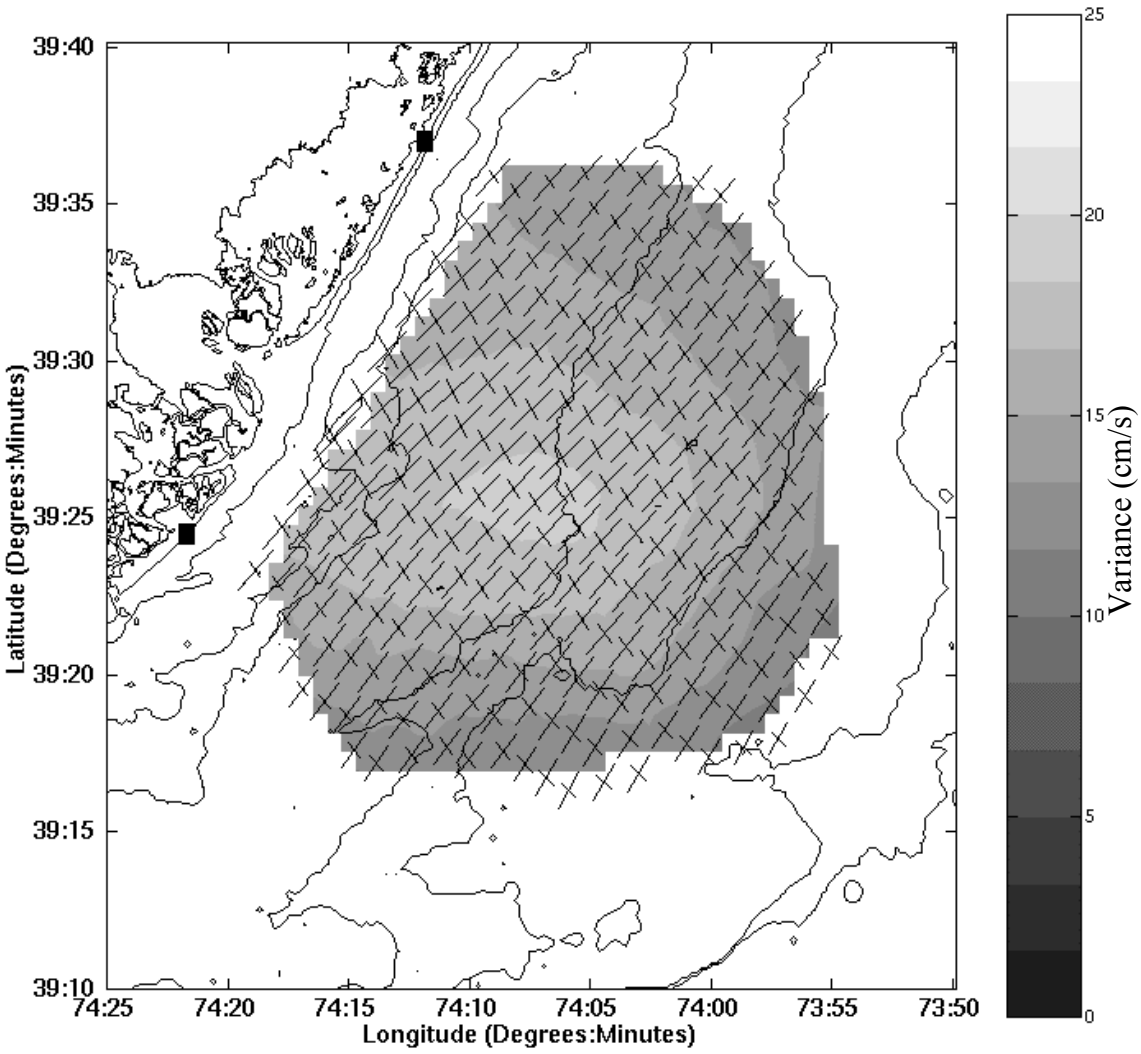

Figure 3.23. Principle components of the mixed regime transient response.

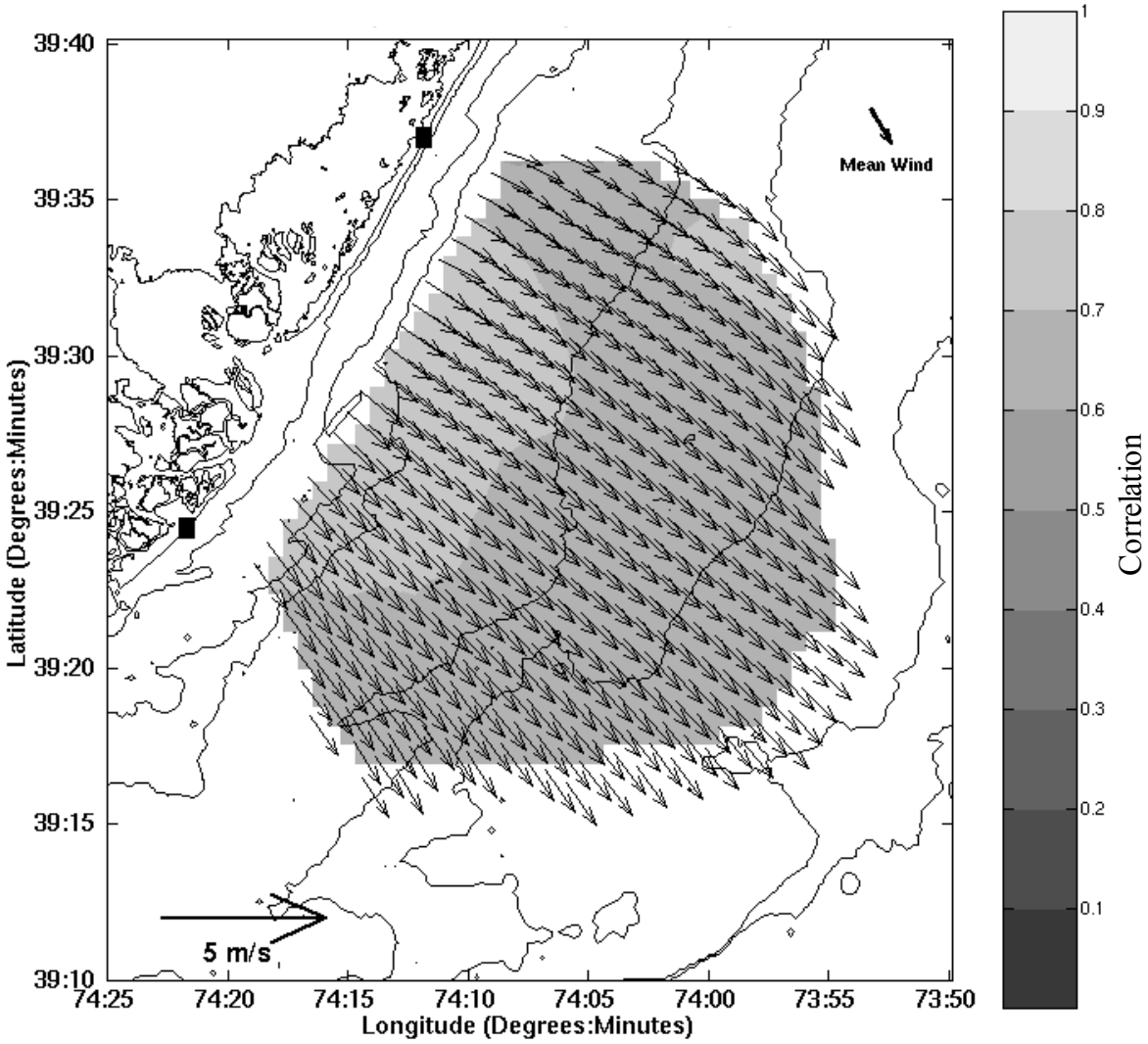

Figure 3.24. Complex correlation of the mixed regime transient response with the local winds. The angle between the mean wind (upper right) and each grid point (black vectors) indicates the offset between the highest correlated current and wind.

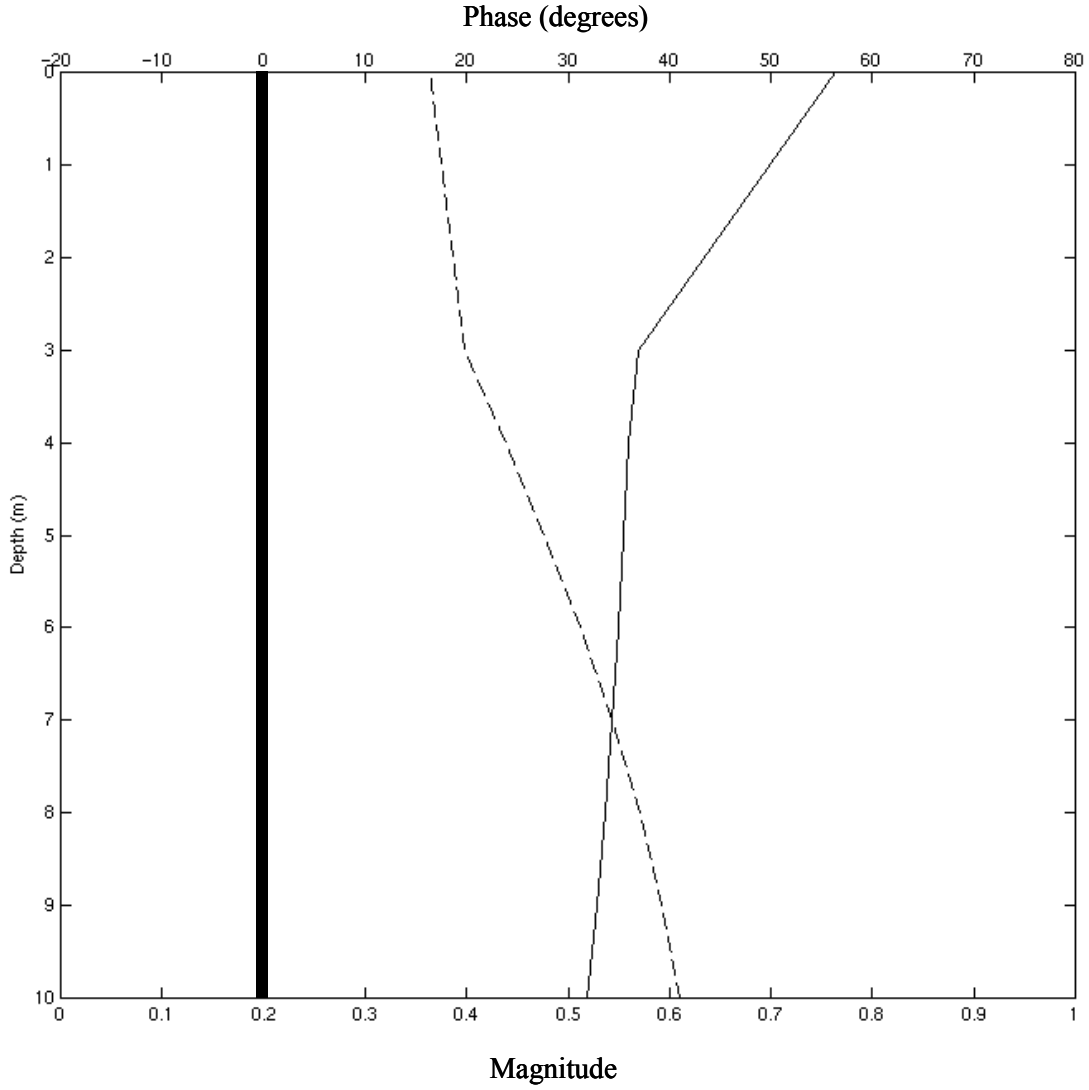

Figure 3.25. Magnitude (thin) and phase (dashed) of the complex correlation between the vertical current profile and the local wind forcing during the stratified regime. Negative phase indicates that the highest correlated current is to the right of the wind. The heavy line indicates zero phase.

acting as a single layer. The single layer rotation to the left could be an indication of a bottom Ekman layer extending to the surface. Assuming a standard linear eddy viscosity, $K=\kappa u_* z$, the scale height of the bottom boundary layer for geophysical flows is:

$$l = \frac{\kappa u_*}{f} \tag{3.5}$$

where κ is von Karman's constant, u_* is the frictional velocity, z is the distance above the bed, and f is the Coriolis parameter (Smith and Long, 1976). Since κ and f are constants, the frictional velocity, u_*, is the only unknown. Assuming a constant stress layer:

$$u(z) = \frac{u_*}{\kappa} \ln(\frac{z}{z_o}) \tag{3.6}$$

where z_o is the height above the bed at which the current goes to zero. The velocities at two different heights (u_1 at z_1 and u_2 at z_2) can be used to solve for u_*:

$$u_* = \frac{(u_2 - u_1)\kappa}{\ln\left(\frac{z_2}{z_1}\right)} \tag{3.7}$$

The two bottom bins of the ADCP are used to estimate u_*, and equation (3.5) is used to estimate the scale height, l. A time series of l indicates that the bottom boundary layer scale height frequently exceeds the water depth (Figure 3.26). With a mean value of 65 m and a standard deviation of 50 m, the shallow water column (<35 m) within the HF radar grid is dominated by overlapping boundary layers.

Using the linear model described above, the residual currents were calculated by subtracting u_{cor} and v_{cor} from the total transient. The principle components have less energy than the total response, however the structure observed in the total mixed variance is still evident in the residual field (Figure 3.27). Therefore the wind forcing appears to

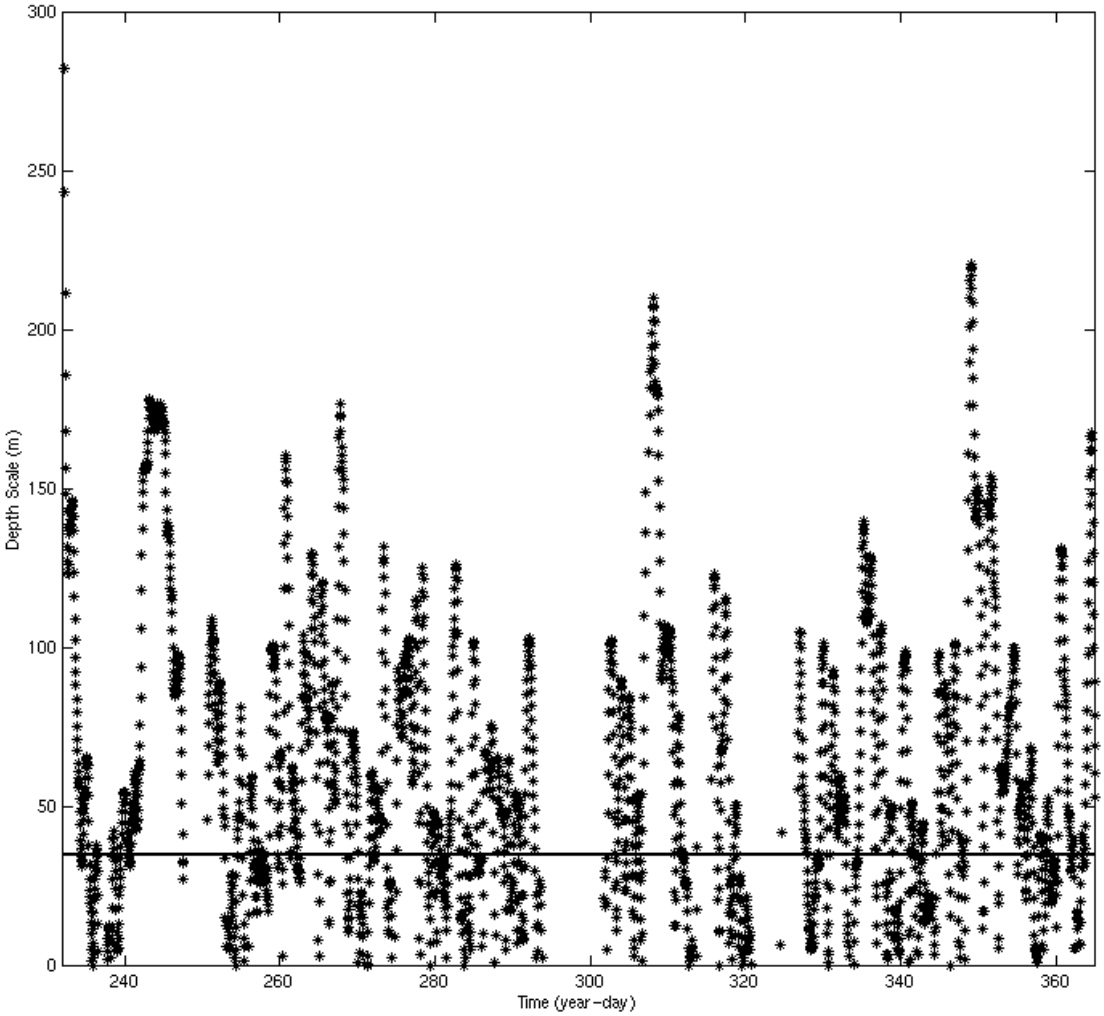

Figure 3.26. Time series of frictional layer thickness, *l*, defined by equation 3.5. For reference, the solid black line indicates the 35 m isobath.

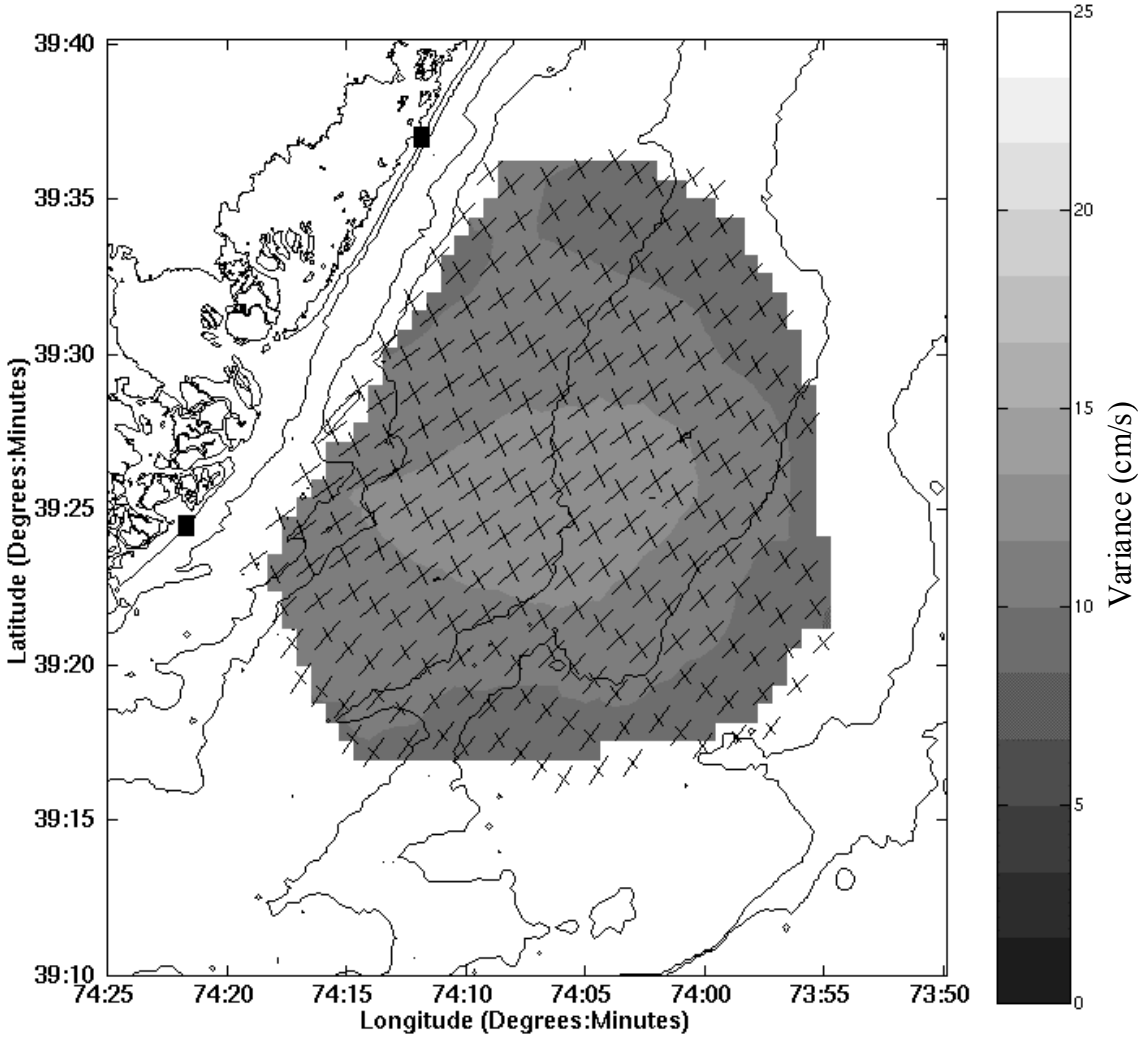

Figure 3.27. Residual component of the stratified regime transient response.

amplify the mixed response but does not drive it. Even without the wind forcing, the spatial structure of the variance remains.

Bottom Topography. Since the entire water column is moving as a frictional layer, the influence of the underlying topography should be evident in the surface currents. There is already an indication of this interaction in the mixed, stratified, and annual fields. To quantify the role of the topography, the along isobath direction was calculated at each HF radar gridpoint using the depth gradient vector, $\vec{H}$.

$$\vec{H} = \frac{\partial h}{\partial L_x}\hat{i} + \frac{\partial h}{\partial L_y}\hat{j} \tag{3.8}$$

Where $\hat{i}$ and $\hat{j}$ are unit vectors, h is depth, and L is the horizontal scale. By definition the along isobath direction is orthogonal to $\vec{H}$. By varying L, different scales of topography were tested. The small-scale meanders in the alongshore topography are on the order of 5 km (Figure 3.28). As L is increased, these meanders are unresolved and the along isobath direction becomes predominantly alongshore across the field (Figure 3.29). It is at this 20 km scale that the topography and the principle components of the transient uncorrelated response are more closely aligned. The angular difference between the predominately alongshore isobaths and the major axis of the principle components has a mean of 29 degrees and a standard deviation of 15 degrees (Figure 3.30). The most striking feature that comes out of this difference is the tendency for smaller offsets to fall along the 20 m isobath (Figure 3.30). Along this isobath, the current variability tends to follow the topography closer than the surrounding area. At the smaller scale of 5 km, some of the steepest gradients also fall along the same 20 m isobath (Figure 3.31). So the current response of the mixed regime is closely linked to the topography on several

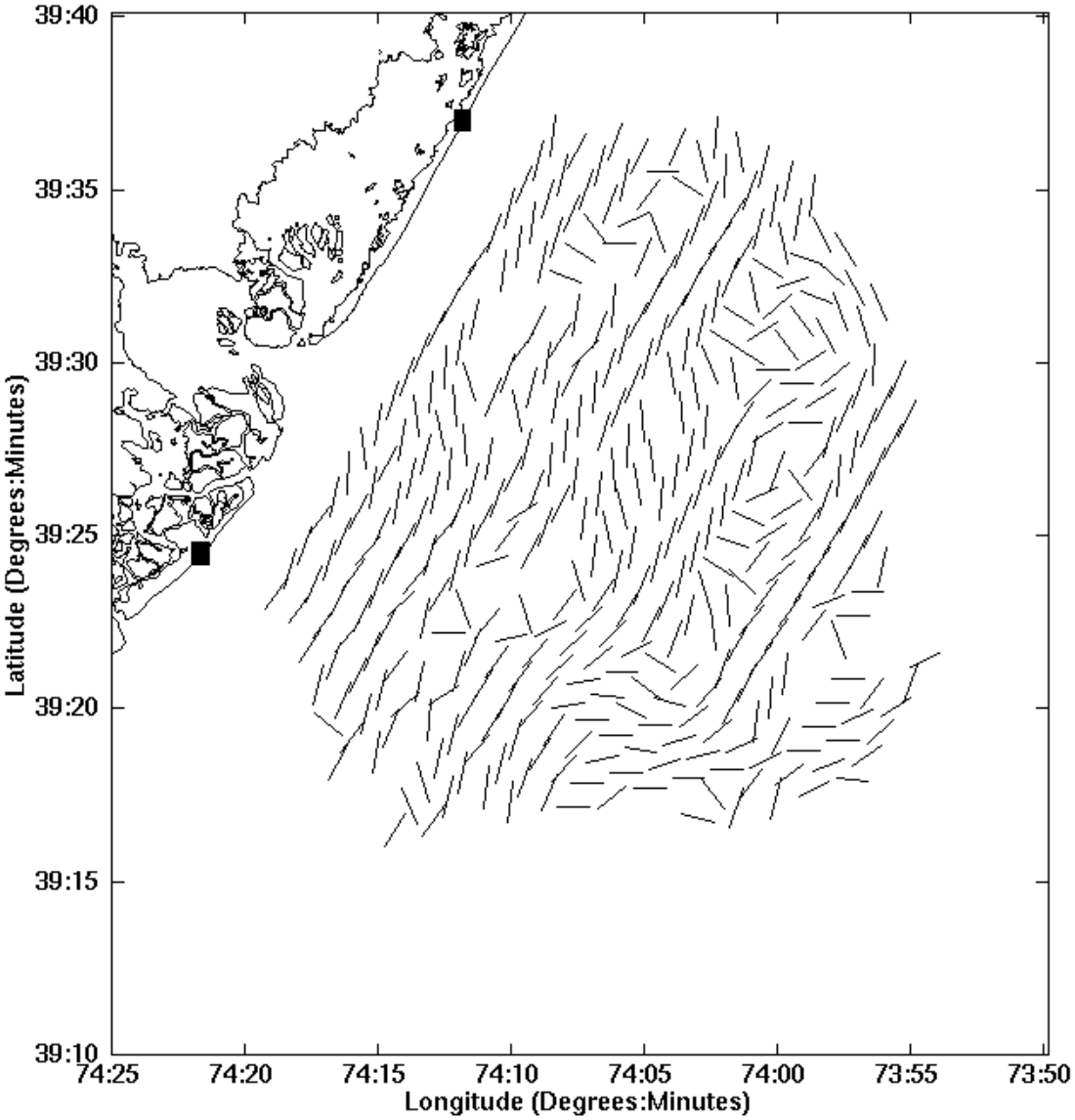

Figure 3.28. The along isobath direction for L = 5 km.

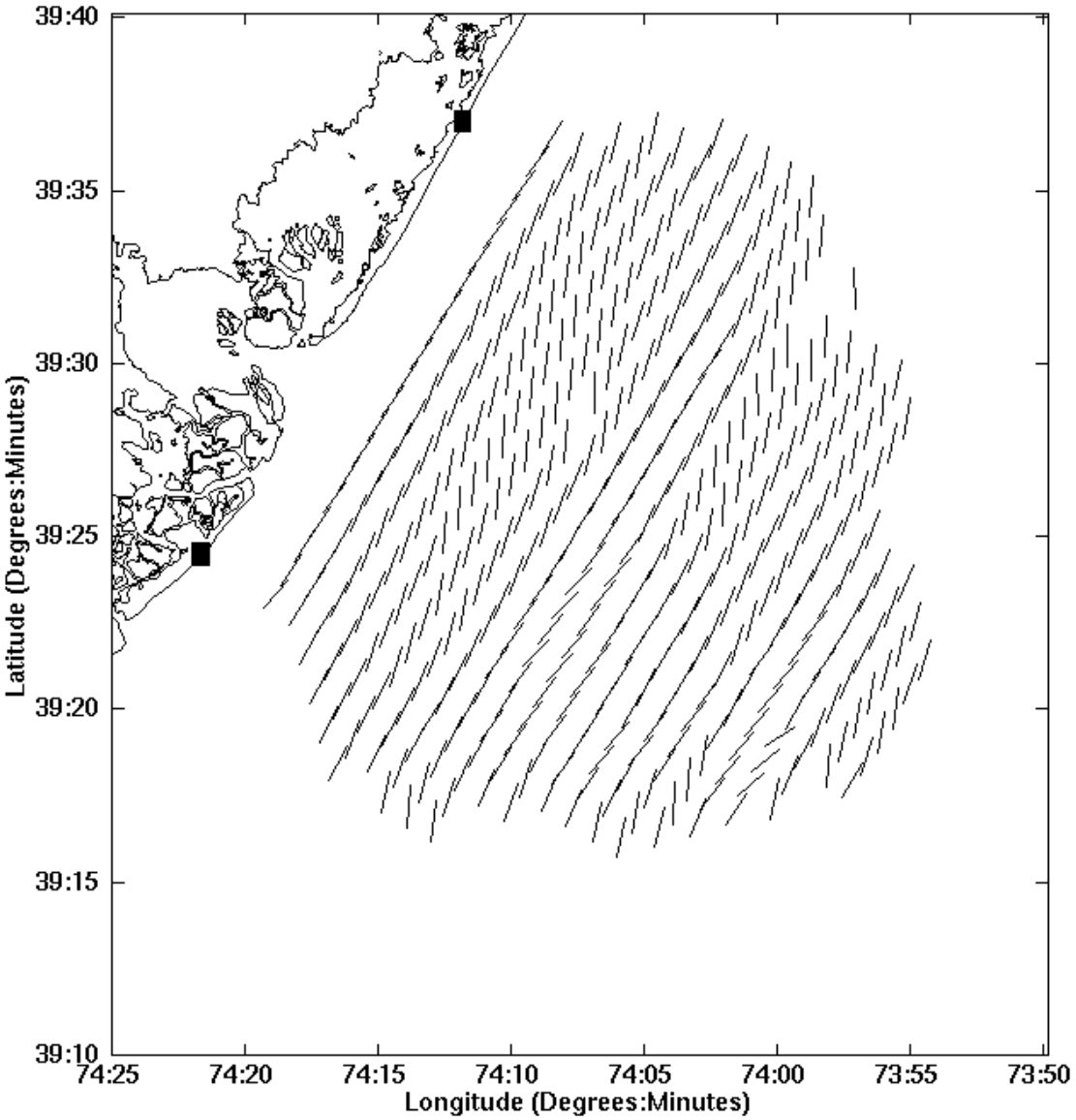

Figure 3.29. The along isobath direction for L = 20 km.

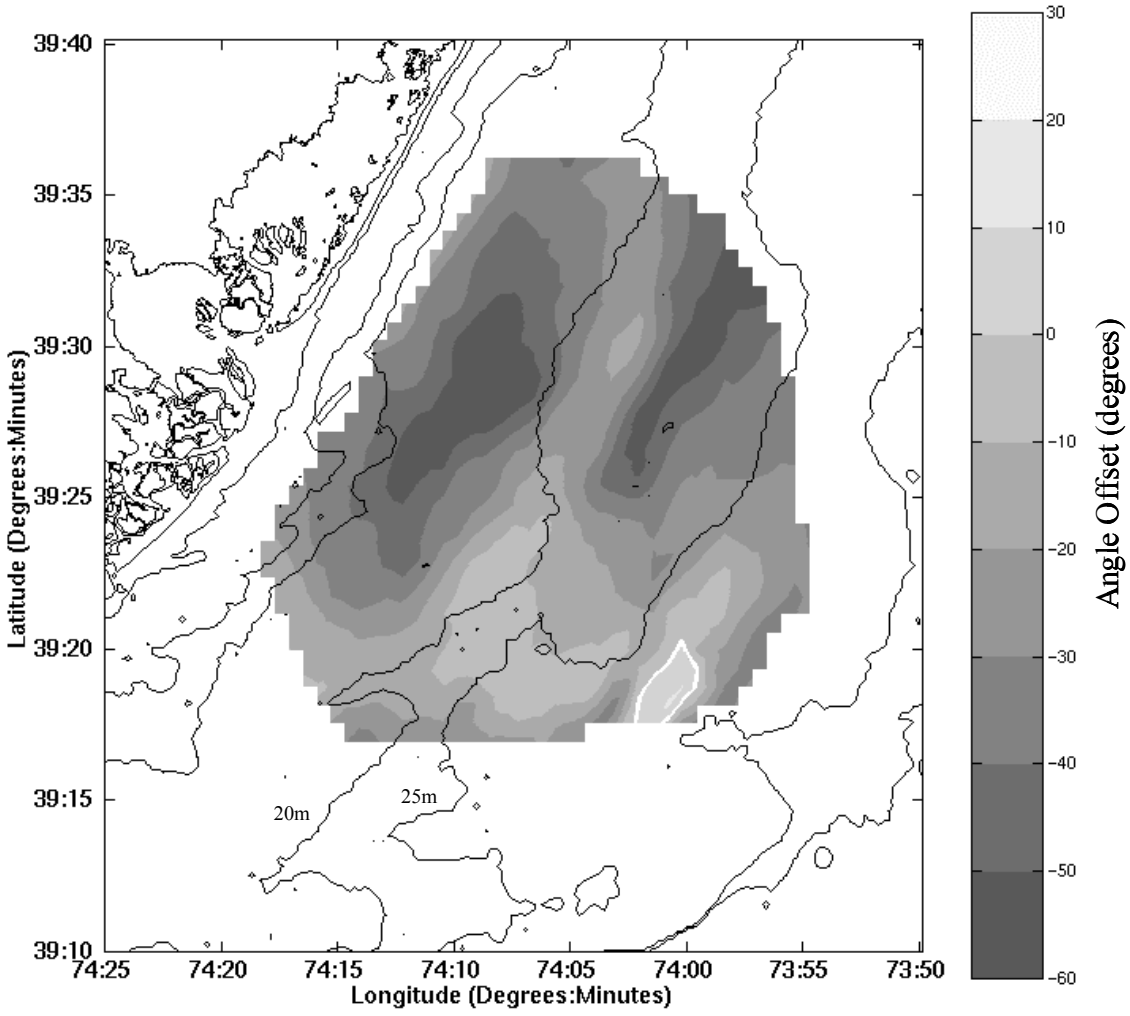

Figure 3.30. The difference between the 20 km along isobath direction and the major axis of the mixed residual response. The 20m and 25m isobaths are also labeled.

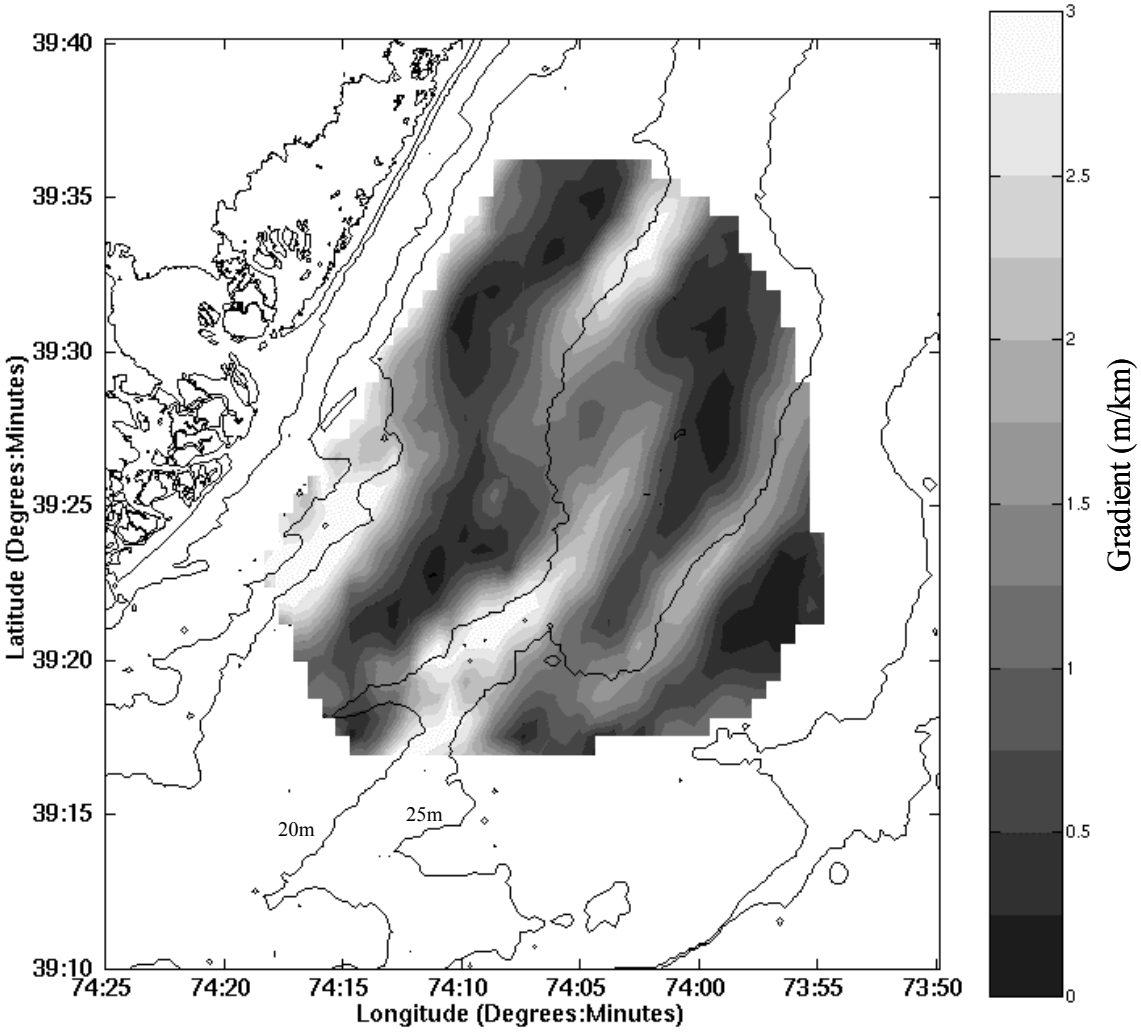

Figure 3.31. The magnitude of the smaller-scale depth gradient (L = 5 km). The 20m and 25m isobaths are also labeled.

scales. The larger alongshore scale topography steers the current variability and the small-scale topography modulates this response with the strongest influence coinciding with the steepest gradients.

3.4 Conclusions

Stratification has been shown to significantly influence the local surface current response to local forcing. Over the annual time scale in which the water column is predominately mixed, the surface flow is alongshore toward the southwest with perturbations reflecting the local topography. If this annual mean is separated into stratified and mixed regimes, clear differences emerge in the response. When the water column is stratified the surface layer is very correlated with the local wind forcing with the highest correlated currents at the surface to the right of the wind. The vertical structure of the correlation shows a two-layer system in which the surface layer flows to the right of the wind and the bottom layer flows to the left. Both the forcing and the response show that the stratified regime is dominated by upwelling/downwelling events. During these events the surface flow is relatively steady with horizontal wind correlation dependent on both local topography and stratification.

In contrast, the mixed regime forcing and response is much more variable. The response tends to be aligned with the coast even though the stronger wind fields no longer favor the alongshore direction. The mixed mean resembles the annual mean having a general flow toward the southwest with perturbations around the local topography. The vertical structure of the correlation shows a single layer in which the most wind correlated current is to the left of the wind throughout the water column. The

left offset of the most correlated current increases with distance below the surface. The frictional length scale calculated throughout this period indicates that the entire water column is composed of a single frictional layer. As a single layer, the surface response is influenced by the local topography on several scales. At the larger 20 km scale, the topography appears to steer the variability in the alongshore direction. Over the smaller scale, the spatial structure of the along-shore variability is influenced locally by the slope of the 5 km scale topography.

Stratification clearly influences the response of the surface currents to local forcing. If the water column is stratified, the surface layer motion is strongly correlated with the wind and, in some locations, also influenced by the underlying topography. If the water column is mixed, the response is less correlated with the wind and significantly influenced by the underlying topography, especially where the depth gradients are maximum.

4.0 STORM DRIVEN RESPONSE OVER THE INNER SHELF

4.1 Introduction

Tropical storms and hurricanes force strong current responses over relatively short time scales. Since the generation and propagation of these storms is difficult to predict, most studies have utilized analytical and numerical models in conjunction with sparse observations to describe the current structure of the response. It has been shown that random wind forcing (Kundu, 1984) and fronts (Kundu, 1986; Paduan et al., 1989) can stimulate a clockwise (CW) rotating near-inertial current. Based on this relationship, most wind-forced response studies associated with passing storms have focused on this frequency band. Brooks (1983) documented a strong near-inertial current in the upper ocean when hurricane Allen passed through an instrument array in the western Gulf of Mexico. This response decayed within days of the passing storm. A similar current structure was observed when hurricane Frederic approached the coast of Alabama (Shay and Elsberry, 1987). Using the measured wind forcing as a boundary condition, a linear, inviscid model was used to predict the current response (Shay et al., 1990; Shay and Chang, 1997). During the storm, the stratified water column responded with a weak barotropic and strong baroclinic component. The baroclinic modes were independent of the free surface boundary condition and propagated energy out of the local surface layer within 4 inertial periods. The less energetic barotropic response, on the other hand, was only predicted if the surface rigid lid condition was eased. Keen and Glenn (1999) found that the energy of the barotropic response propagated away from the storm as a Kelvin wave set up by the storm surge near the coast. In the Mid-Atlantic Bight (MAB), hurricane Belle forced two different responses on the outer and mid-shelf (Mayer et al.,

1981). The near-inertial oscillation on the mid-shelf lasted only 2 days compared to the longer response observed in the deeper water over the outer shelf. Mayer et al. (1981) identify friction as a possible contributor to this difference. It has also been suggested that during storm forcing, friction increases shear in shallow water and rotates the currents in deep water (Keen and Glenn, 1995).

In September 1999, tropical storm Floyd propagated toward the northeast along the New Jersey coast. Unlike the responses outlined above, the ocean was initially well-mixed and shallow O (30 m). A coastal ocean observatory set up off the southern New Jersey coast captured the local forcing and current response with a suite of atmospheric and oceanographic instruments. While near-inertial currents have been observed within the study site, this response is typically seen during the summer months when the water column is stratified (Chant, 2001). Chant (2001) shows that this baroclinic response, initiated by the local winds, propagates offshore through the thermocline. Chant (2001) also suggests that the mixing event associated with the passing of tropical storm Bertha near the end of the study period inhibits a rotating near-inertial response. Based on these results, the typical rotating response is not expected for the unstratified water column preceding tropical storm Floyd. In this analysis, the observations are complimented with analytical models to characterize the current structure before, during and after the passing of tropical storm Floyd. Comparisons are drawn between this unstratified shallow water response and the deeper stratified response discussed above.

Section 4.2 describes the instrumentation used in the study. An overview of the forcing associated with tropical storm Floyd is presented in section 4.3. Section 4.4

describes the current response to this forcing with observations and analytical models. Finally, section 4.5 presents some concluding remarks.

4.2 Methods

Instrumentation. The forcing and response to tropical storm Floyd was captured by several different components of an ocean observatory off the New Jersey coast (Figure 4.1). Remote systems including satellites and High Frequency (HF) radar provided complete coverage of ocean surface parameters including sea surface temperature and surface velocity fields. The HF radar system uses two sites in Brant Beach and Brigantine, New Jersey (Figure 4.1) to generate hourly surface current maps (Barrick, 1977; Barrick and Lipa, 1986). The particular dataset used here is a subset of the annual dataset described in Chapter 3. The HF radar grid stretches 40 km in the along-shore direction and about 30 km in the cross-shore direction (Figure 4.1). The time series data at each grid point were detided with a least squares fit of the dominant regional tidal constituents to a yearlong time series.

Subsurface velocity was measured with a bottom-mounted ADCP at the Longterm Ecosystem Observatory (Grassle et al., 1998; Glenn et al., 2000a; Schofield et al., 2001). The ADCP is located about 5 km offshore in 12 meters of water (Figure 4.1). The subsurface data were centered averaged on the top of the hour and detided to match the sampling of the HF radar system. The depth-averaged flow discussed in this paper is an average of the ADCP data from 3 to 10 m and a surface measurement from an HF radar grid point near the ADCP. In addition to subsurface velocity, the LEO CTD provided time series data of bottom temperature, pressure and salinity. Using the time series of the

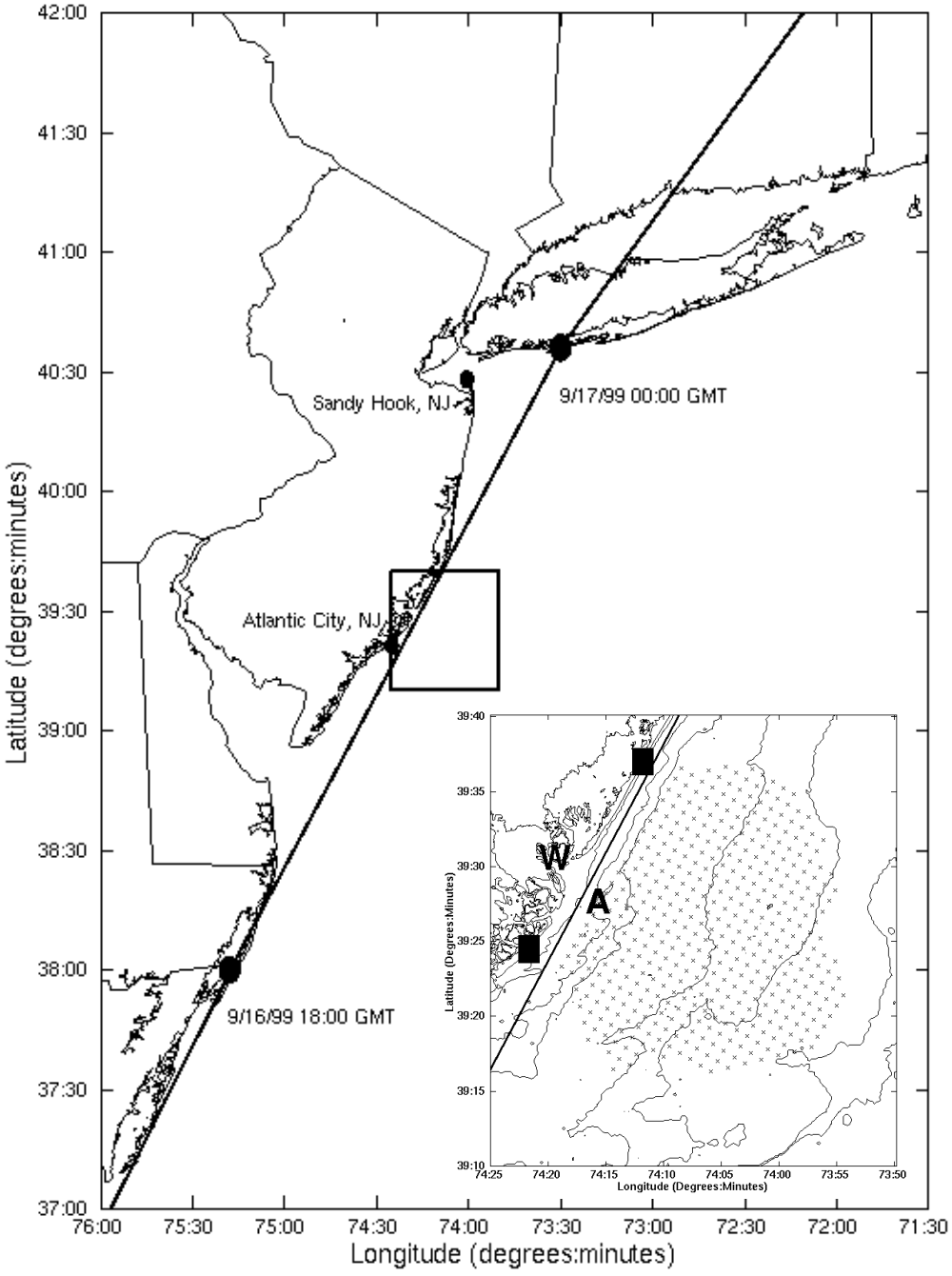

Figure 4.1. Storm track for hurricane Floyd and the locations of the NOAA coastal sites in Atlantic City and Sandy Hook are shown. The locations of the HF radar sites (black squares), HF radar grid (*), ADCP/CTD (A) and met station (W) are shown in the inset.

measured temperature and salinity to calculate density and assuming a hydrostatic balance in the vertical, the sea level height was estimated at the LEO site. The Sea Level Anomaly (SLA) is based on a 45-day mean. The measured SLA was corrected for atmospheric pressure and detided using the harmonic fit described above. SLA based on Mean Sea Level (MSL) was also measured at two NOAA coastal sites in Sandy Hook and Atlantic City, New Jersey (Figure 4.1). These data were also corrected for atmospheric pressure and detided. The meteorological data, measured at the Rutgers University Marine Field Station (Figure 4.1), included time series data of temperature, atmospheric pressure, winds, and relative humidity. A more detailed description of the instrumentation and data coverage can be found in Chapter 3 of this dissertation.

4.3 Forcing

During the morning hours of September 8th, 1999 (yd 251), tropical storm Floyd first formed about 1400 km east of the Leeward Islands. After two days, the storm strengthened to hurricane status and continued on a west/northwest track toward the eastern United States. Floyd's intensification fluctuated between category one and four on the Saffir/Simpson Hurricane Scale with sustained winds from 150 to 250 km/hr. The hurricane made landfall along the southern North Carolina coast at 06:30 GMT on September 16th (yd 259). At this time Floyd was a category two hurricane with sustained winds near 167 km/hr and a forward speed of about 28 km/hr. After landfall, the heavy rains caused extreme flooding as the storm weakened and accelerated toward the north/northeast. Floyd was downgraded to a tropical storm at 1800 GMT on yd 259 with sustained winds of 111 km/hr. The strong tropical storm continued moving toward the

northeast along the New Jersey coast with a forward speed of about 54 km/hr (Figure 4.1). Wind data from the Rutgers meteorological station clearly shows the center of the storm arriving late on yd 259 (Figure 4.2). The eye of the storm, seen in the local winds and barometric pressure (Figure 4.2), passes through the study site at yd 259.9167. Prior to the eye, the strong southeast winds peaked at 18 m/s. Within the eye, the winds diminished to 5 m/s before 15 m/s northwest winds accompanied the second half of the storm. Throughout the period the winds were predominately in the cross-shore direction. The near-inertial energy of the wind forcing peaks before and after the eye (Figure 4.2c). The equal amplitude of the CW and counterclockwise (CCW) rotating components indicates that the near-inertial forcing is rectilinear (Figure 4.2c). With an inclination 60 degrees left of true north, this rectilinear response has a cross-shore orientation. There was also locally heavy rainfall associated with the storm that peaked at 1.4 cm/hr at Atlantic City (Figure 4.2e). This rainfall potentially increases the freshwater flux to the inner-shelf after the storm.

Hydrography. The inner-shelf observatory focuses on the coastal ocean within the 30m isobath. Within this shallow system, vertical temperature gradients, calculated with surface satellite data and bottom CTD data, never exceed 2 °C throughout the storm forcing (Figure 4.3a). There is also a tendency for warmer water near the surface before the storm and cooler water near the surface after the storm, indicating a fresher ocean surface after the storm. The bottom salinity minimum just after the storm also supports a freshwater pulse into the coastal ocean coincident with the storm rains (Figure 4.3b). Perhaps the strongest ocean signal associated with Floyd was seen in the sea surface

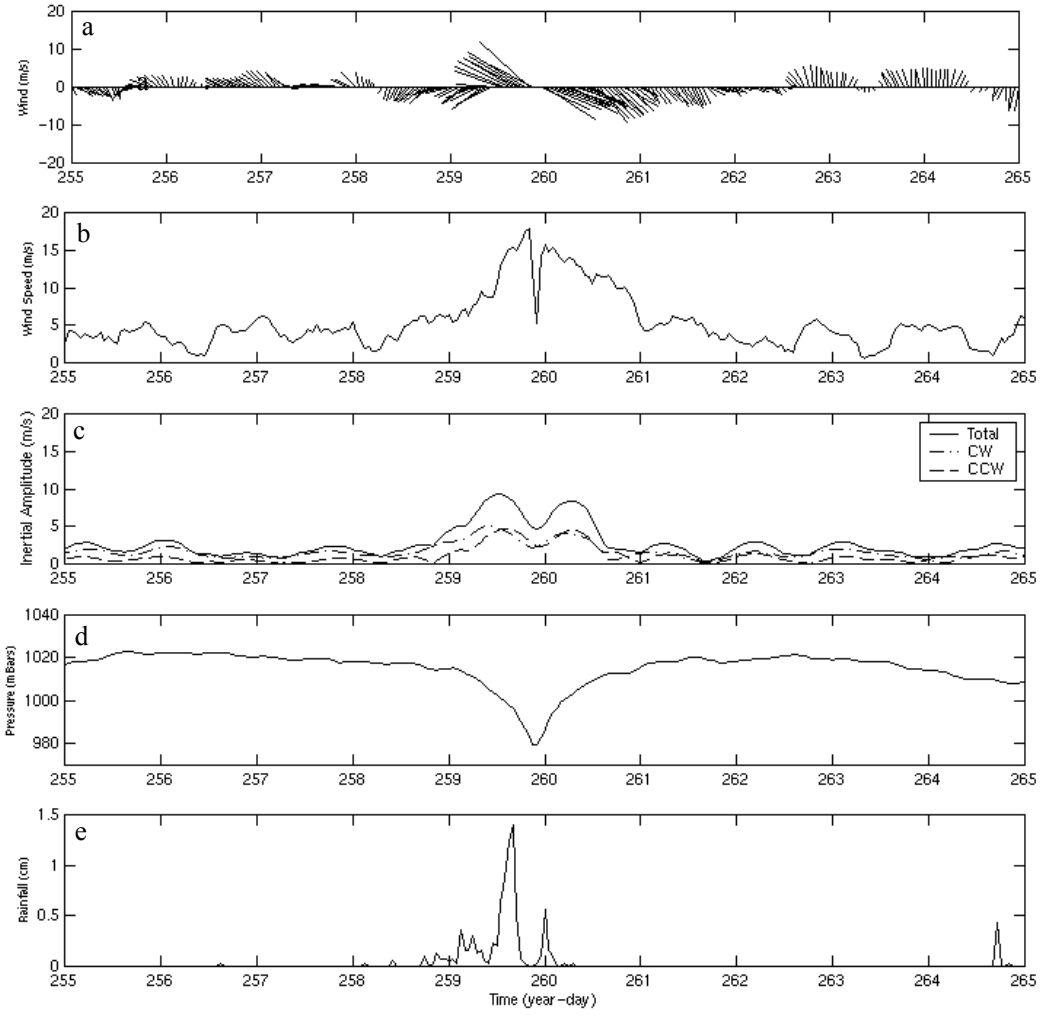

Figure 4.2. Time series of (a) wind velocity, (b) wind magnitude, (c) near-inertial wind amplitude, (d) barometric pressure, and (e) hourly Atlantic City precipitation surrounding tropical storm Floyd.

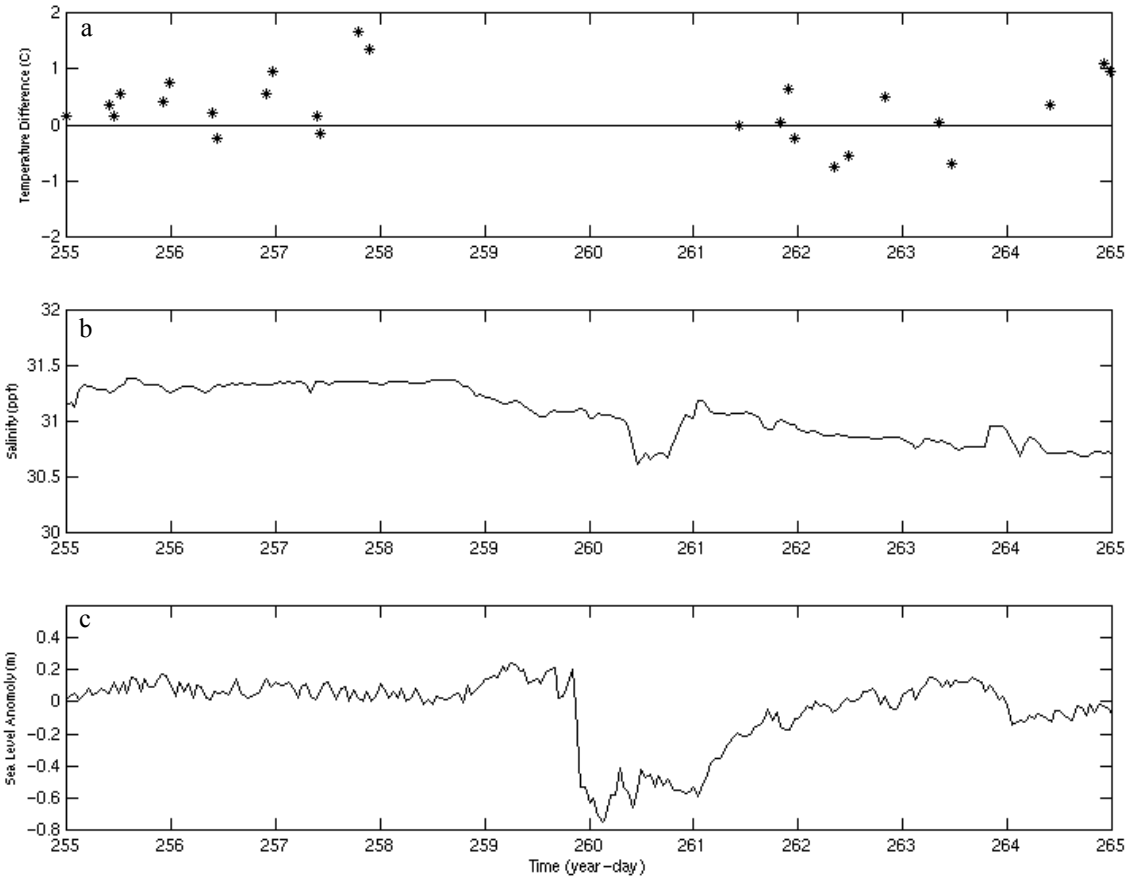

Figure 4.3. (a) Temperature gradient, (b) bottom salinity , and (c) sea level anomaly during the passage of tropical storm Floyd.

height. A surge of 20 cm at the offshore site was followed by an 80 cm drop coincident with the eye of the storm (Figure 4.3c). This 80 cm drop is about 6% of the total water column. After the storm, a freshwater pulse into the inner shelf potentially stratifies initially mixed water column.

4.4 Response

The vertical current structure several days before the storm was highly sheared (Figure 4.4). The stronger currents near the surface tend to follow the winds more closely than the weaker currents near the bottom (Figure 4.4). There is also a slight rotation to the left with depth. This rotation is representative of the typical vertical structure seen throughout the Fall of 1999 (Chapter 3). As the storm approaches, this climatology breaks down and the currents increase and become more uniform with depth (Figure 4.4). Even though the wind forcing is primarily in the cross-shore direction, the depth independent current response is alongshore (Figure 4.4). Within 48 hours of the storm onset, the episodic response is replaced by the seasonal structure observed before the storm.

4.4.1 Near-inertial response

4.4.1.1 Observed near-inertial response

The near-inertial component of the flow was obtained using a least squares fit to the detided time series. The local inertial frequency was fit to the data using a 1.5 day

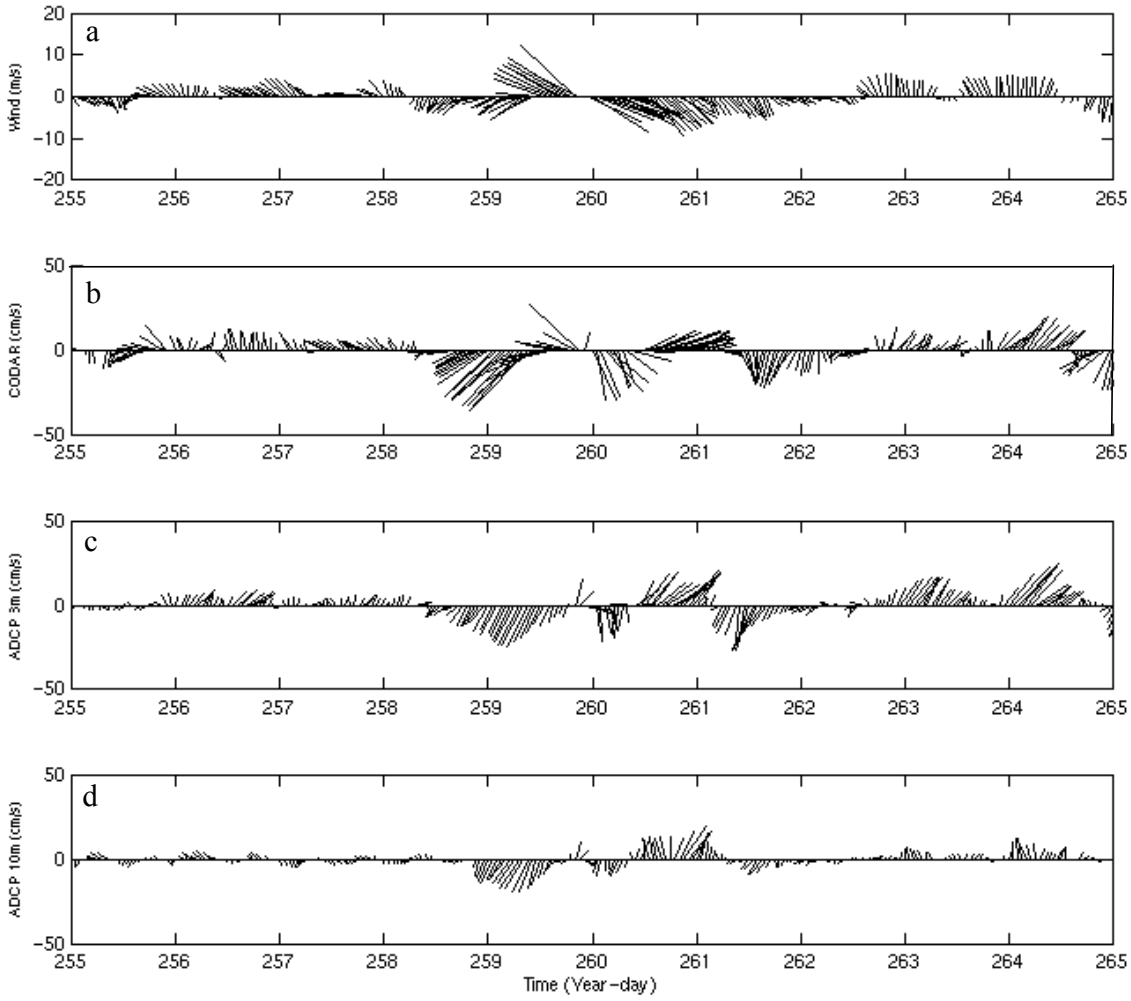

Figure 4.4. Time series of (a) wind velocity, (b) surface current (c) current at 3 m depth, and (d) current at 10 m depth surrounding tropical storm Floyd.

moving window. This technique has been used in previous dynamical studies and is the mathematical equivalent to complex demodulation (Chant, 2001).

The near-inertial amplitude peaks during the storm, between year day 259 and 261 (Figure 4.5). There is very little vertical structure in the band except for slightly weaker amplitudes near the bottom. The equal amplitude of the clockwise and counterclockwise rotating components indicates that, like the forcing, the response is rectilinear.

Spatial maps of the near-inertial response show that this rectilinear response is oriented in the along-shore direction. At one half inertial period before the storm, the strongest response is seen in the shallower water near the coast (Figure 4.6). There is a slight 5 degree advance in phase between the southern and northern edges of the field. When the eye is over the study site, the response is in phase and reaches its peak amplitude over the entire field (Figure 4.7). Within half an inertial period after the storm, the currents, still in phase, have significantly decreased across the field (Figure 4.8). Throughout the entire event, the near-inertial response is nearly uniform across the HF radar field and peaks with the storm.

The vertical structure of the near-inertial response is also rectilinear with a mean eccentricity on the order of 10^{-3}. Half an inertial period before the eye, the amplitudes are relatively weak with an 8 cm/s maximum near the surface. There is a slight rotation to the left with depth, however, the ellipses are generally oriented along the coast (Figure 4.9a). Similar to the surface response the amplitudes peak near the center of the eye with amplitudes reaching 18 cm/s near the surface and 12 cm/s near the bottom. Once again, the ellipses are oriented with the coast and in phase throughout the water column (Figure

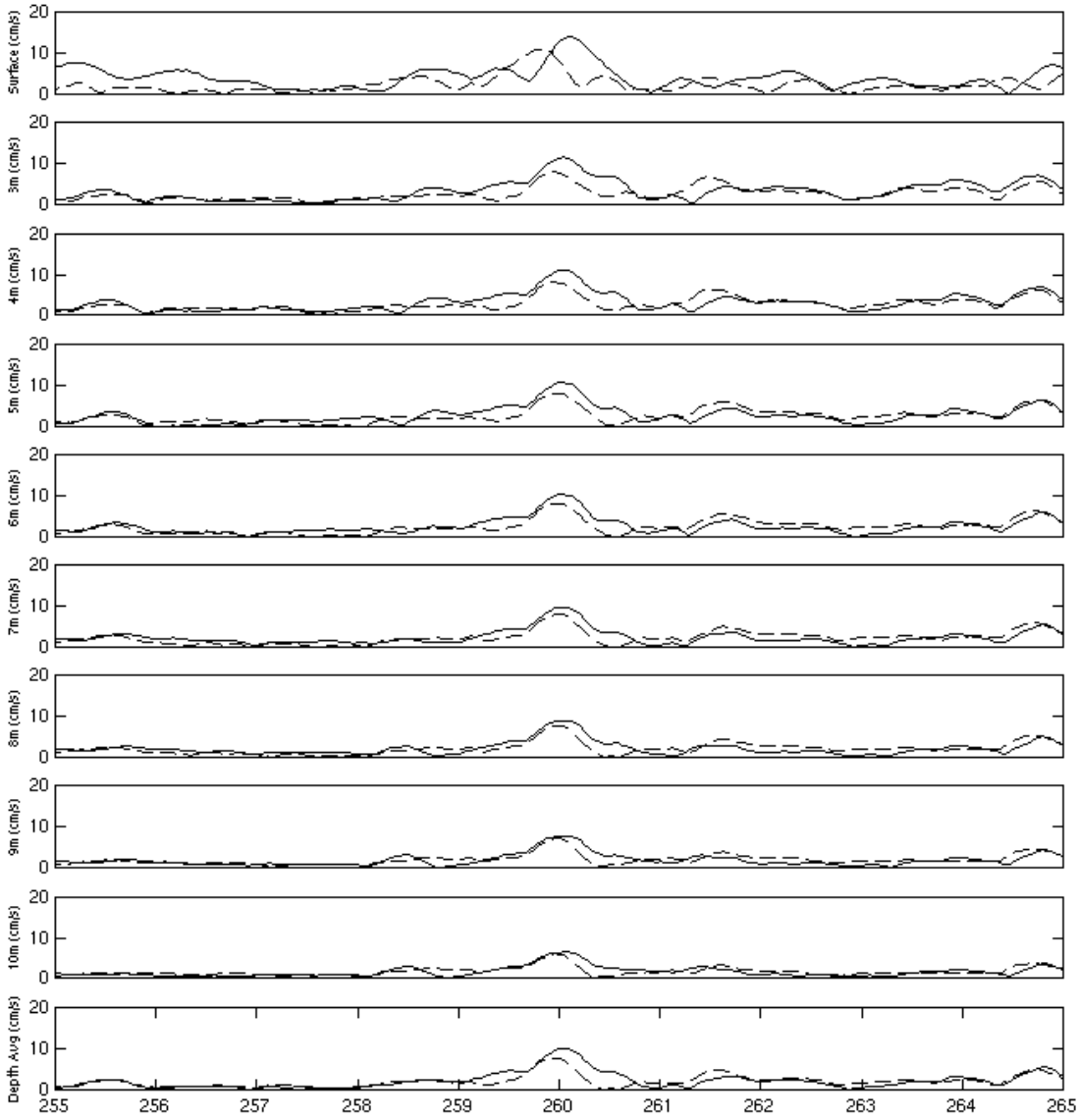

Figure 4.5. Vertical structure of the CW rotating (solid) and CCW rotating (dashed) components of the near-inertial response.

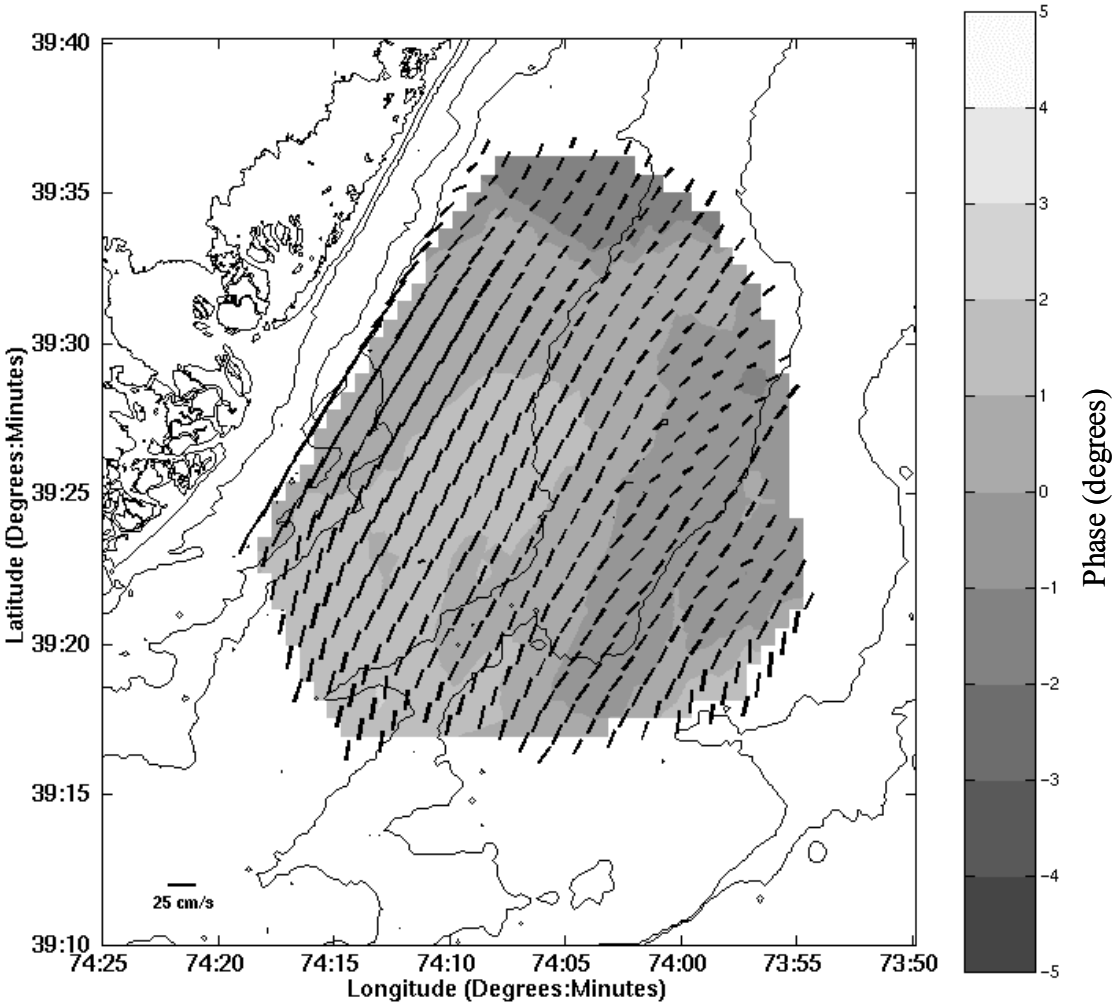

Figure 4.6. The amplitude, orientation, and phase of the near-inertial ellipses ½ inertial period before the passing of tropical storm Floyd.

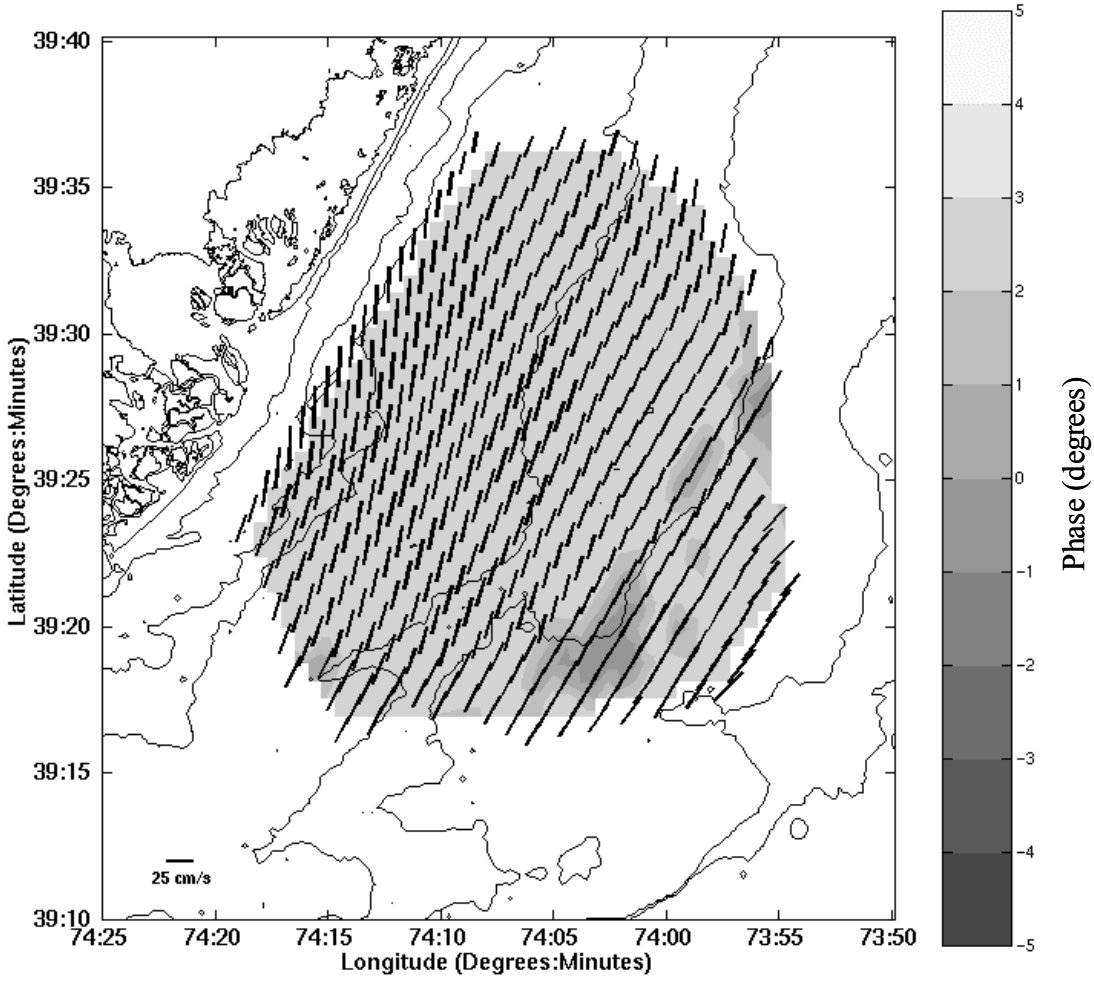

Figure 4.7. The amplitude, orientation, and phase of the near-inertial ellipses during tropical storm Floyd.

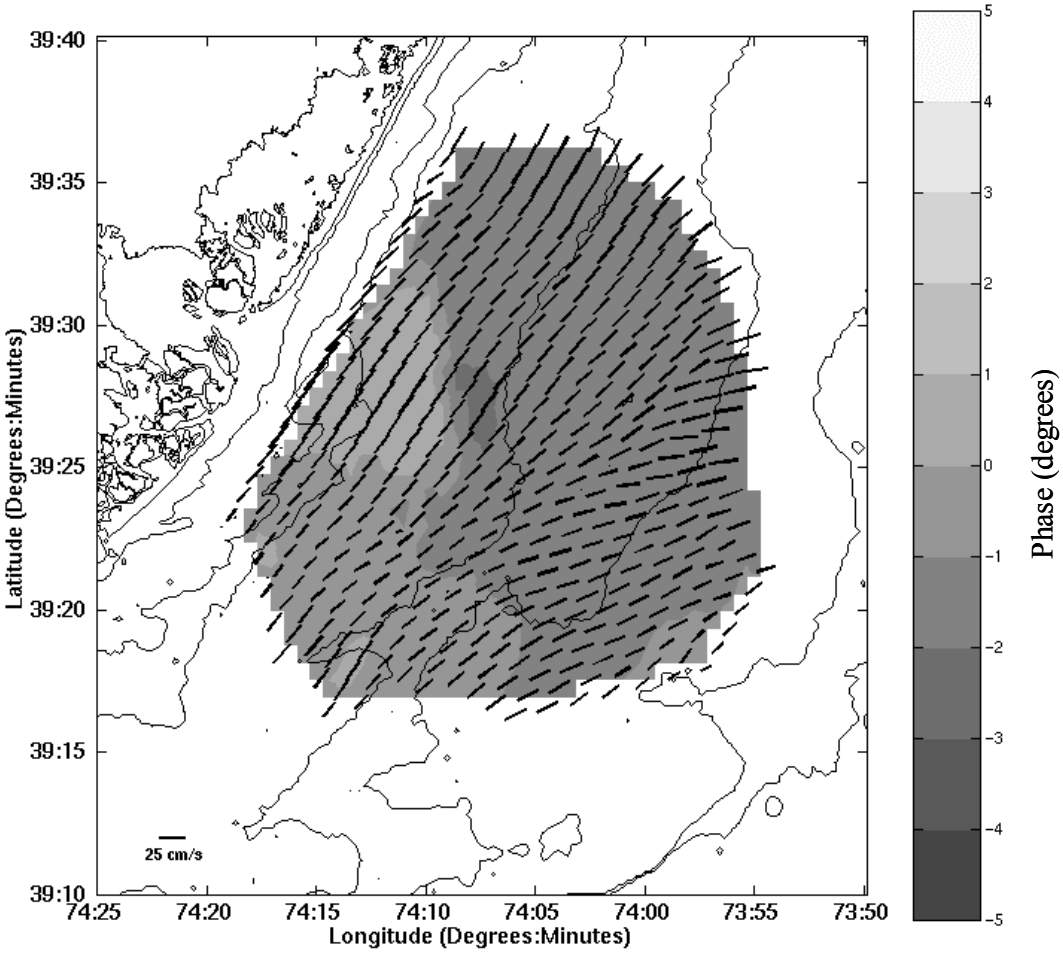

Figure 4.8. The amplitude, orientation, and phase of the near-inertial ellipses ½ inertial period after the passing of tropical storm Floyd.

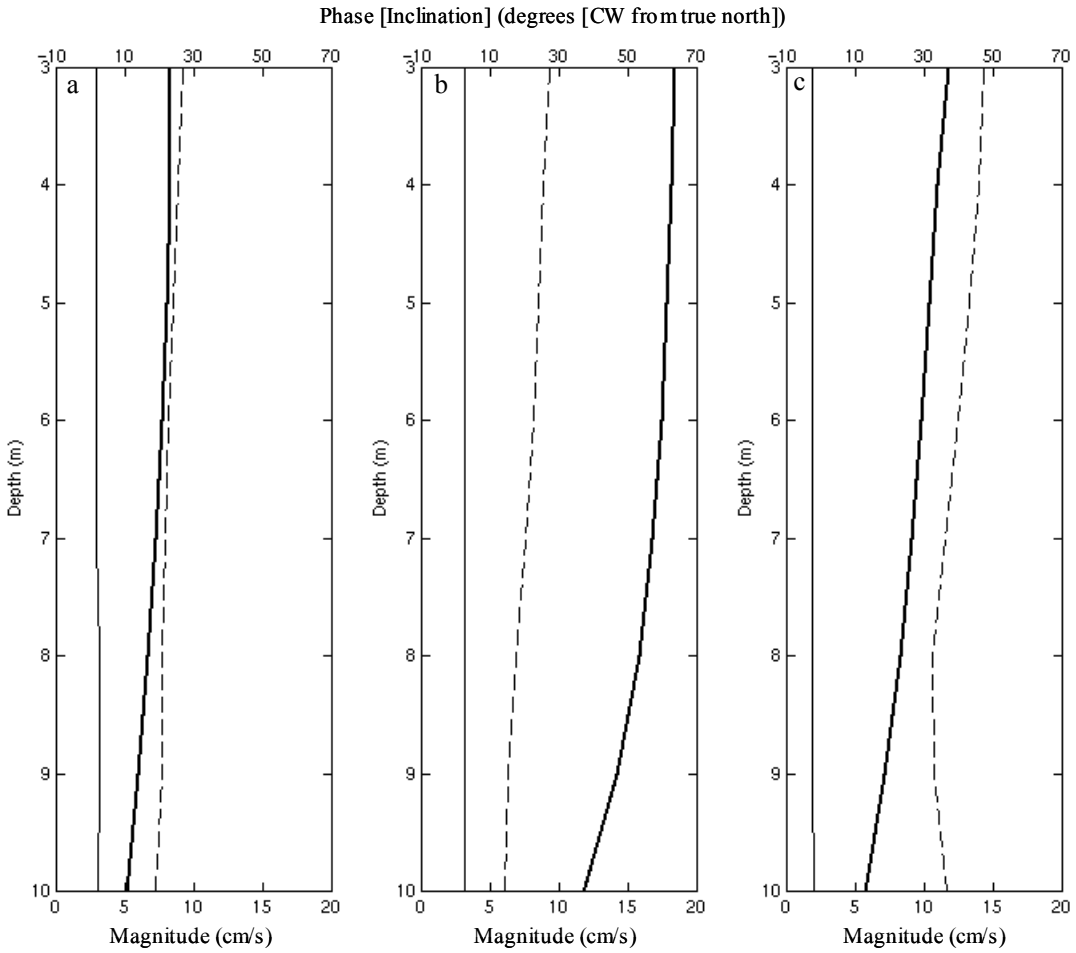

Figure 4.9. The magnitude (thick), inclination (dashed), and phase (thin) of the near-inertial rectilinear response (a) ½ inertial period before, (b) during , and (c) ½ inertial period after the passing of tropical storm Floyd.

4.9b). Throughout the storm, the depth independent structure of the response is rectilinear in the along-shore direction and peaks with the storm. Since the shear is so weak during the storm, a 1-d model is used to study the observed response.

4.4.1.2 Modeled near-inertial response

Using the Pollard and Millard (1970) slab model, the near-inertial response was simulated based on the local tropical storm wind field. This model has been used in previous studies to predict the near-inertial response to local wind forcing (Pollard, 1980; Paduan et al., 1989). The governing equations of the model are:

$$\frac{\partial u}{\partial t} - fv = F - cu \tag{4.1}$$

$$\frac{\partial v}{\partial t} + fu = G - cv \tag{4.2}$$

where u [F] and v [G] are the cross-shore and along-shore components of the depth-averaged velocity [acceleration due to wind friction], f is the Coriolis parameter, and c is an e-folding damping scale. Pollard (1980) shows that with a local wind field measurement, this simple model adequately predicts the near-inertial response. Some model inaccuracies can occur if the depth of the mixed layer is not known or varies with time (Pollard and Millard, 1970). Since the study area here is so shallow and the entire water column mixed, the depth of the mixed layer defaults to the depth of the water column and does not change with time. The wind frictional force is calculated from the measured wind fields at the Marine Field Station using the following relationships:

$$F = \frac{\rho_a C_d U_m U_x}{\rho_w H} \tag{4.3}$$

$$G = \frac{\rho_a C_d U_m U_y}{\rho_w H} \tag{4.4}$$

where ρ_a [ρ_w] is the density of the atmosphere [ocean], C_d is the drag coefficient (taken to be 0.002), U_m [U_x, U_y] is the magnitude [cross-shore component, alongshore component] of the local wind. This leaves the e-folding damping scale, c, as the only adjustable parameter in the model. Previous studies have found decay scales on the order of 2 to 8 inertial periods with an average of 4 inertial periods (Pollard and Millard, 1970; Paduan et al., 1987; Shay and Elsberry, 1987). Based on these findings, the model was initially run with an e-folding scale of 4 inertial periods. The predicted depth-averaged near-inertial response of this run is overestimated by the model (Figure 4.10). For both the total and CW rotating component, the model overestimates the peak and the residence time of the energy compared to the observed response. The CCW rotation is the only component underestimated by the model. Similarly, the phase of the total and CW response is better predicted than the CCW phase (Figure 4.11). If the e-folding scale is reduced to one inertial period, the model prediction is much closer to the observed response (Figure 4.12). Both the amplitude and residence time of the total and CW rotating energy is now on the same order as the observations. The shorter decay scale, however, still underestimates the CCW rotating component. The phases are also more closely modeled, especially for the total and CW response (Figure 4.13). With increased friction, the model better predicts the observed near-inertial response. Since the model underestimates the CCW component, the total predicted response rotates CW at the inertial period. This type of near-inertial response is typically observed in a deeper more stratified ocean. The inability of the model to simulate the observed rectilinear response

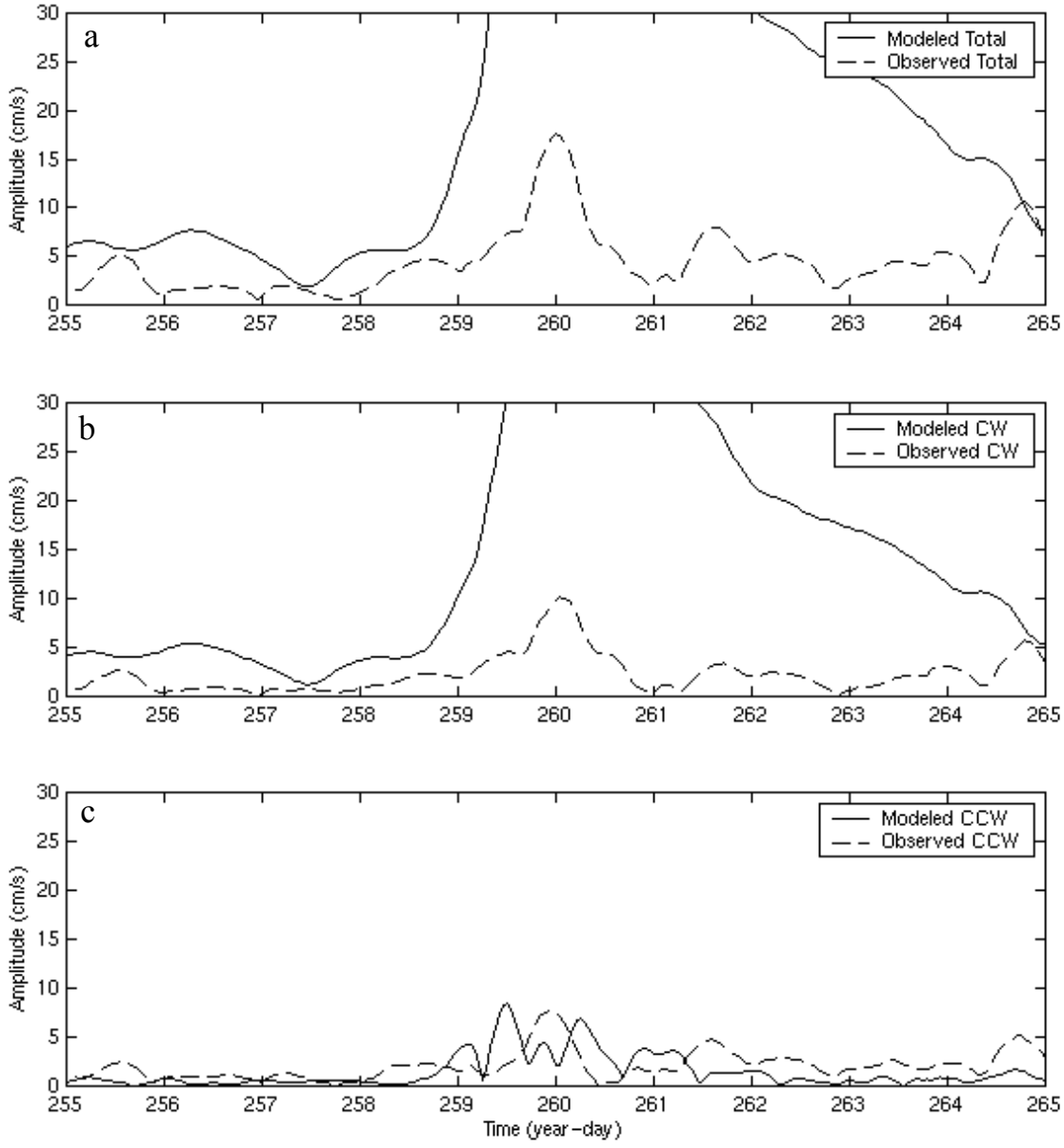

Figure 4.10. The (a) total, (b) CW rotating, and (c) CCW rotating component of the near-inertial amplitude. For this particular run *c* was set to 1/4f.

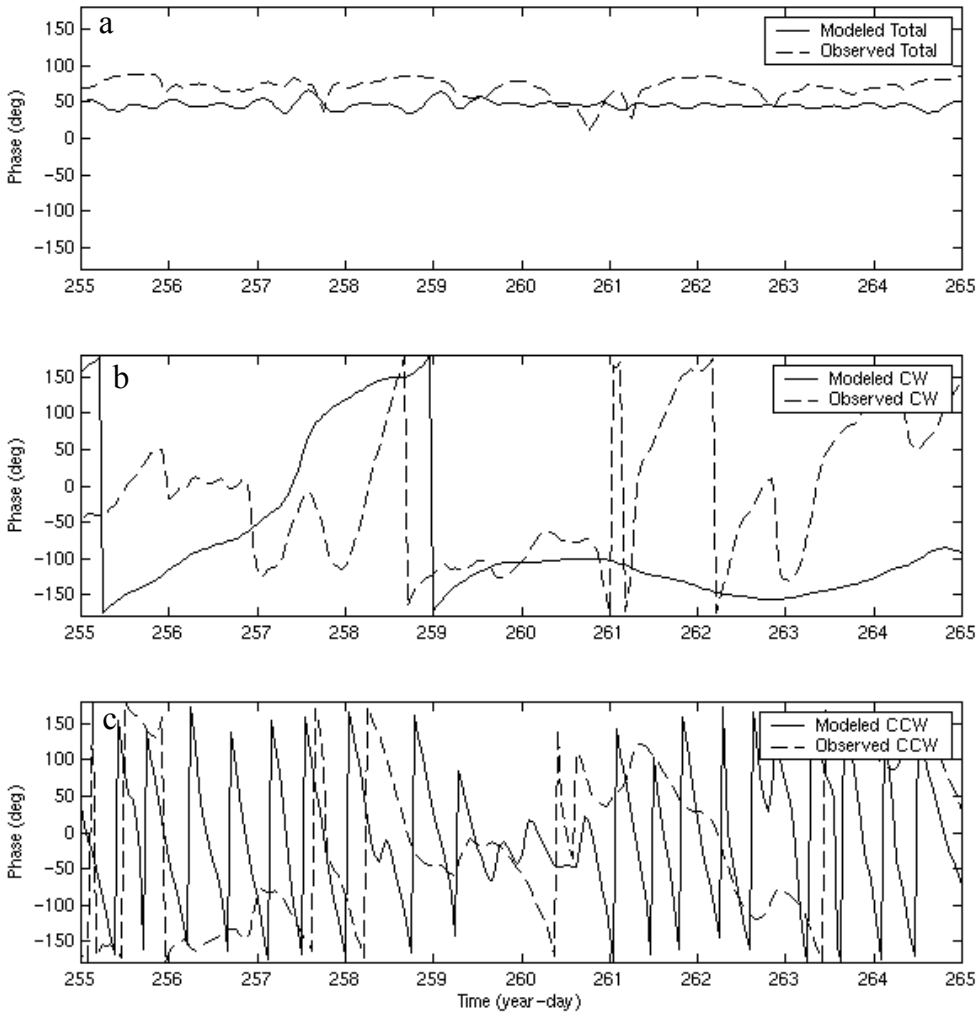

Figure 4.11. The (a) total, (b) CW rotating, and (c) CCW rotating component of the near-inertial phase. For this particular run *c* was set to 1/4f.

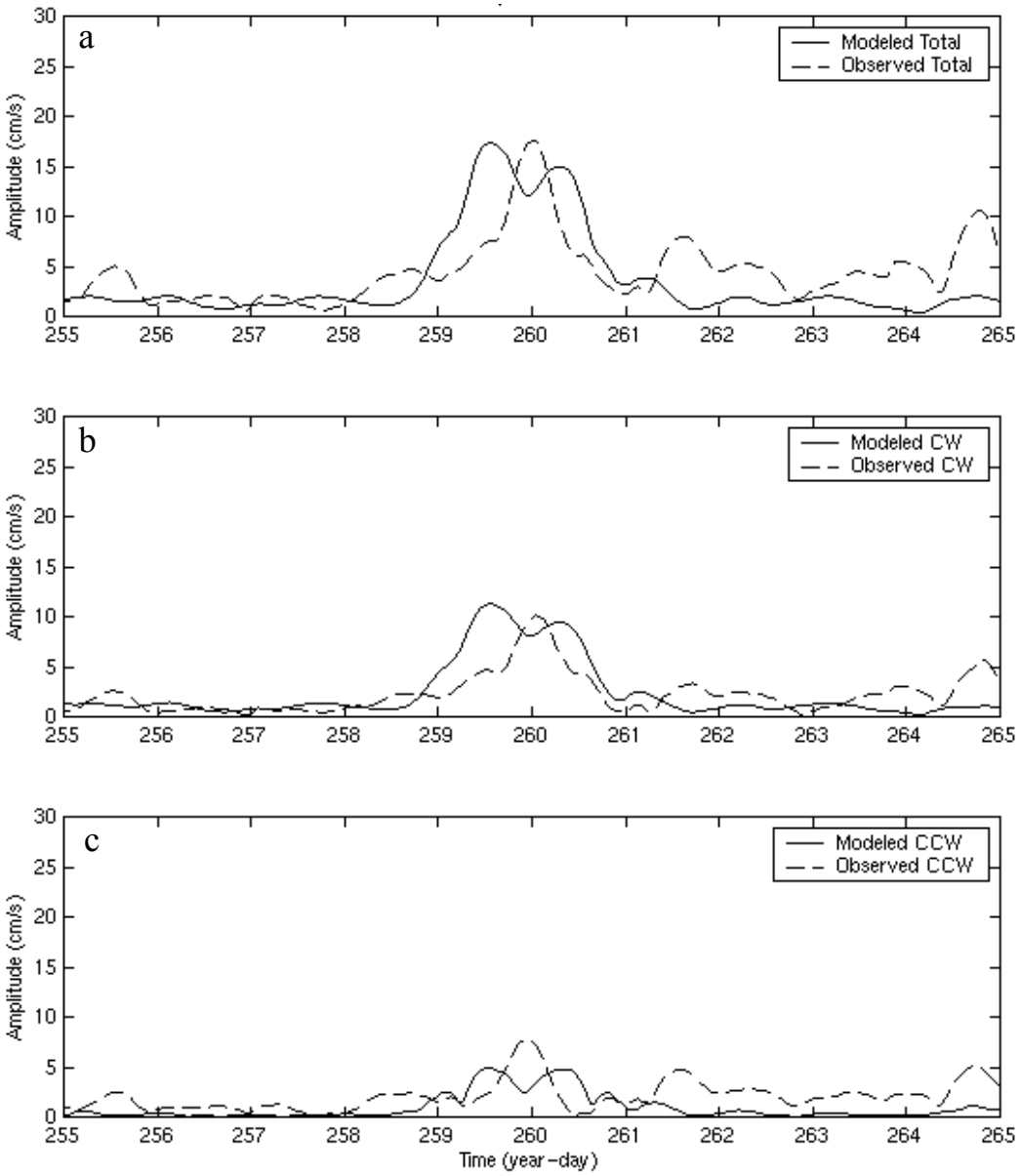

Figure 4.12. The (a) total, (b) CW rotating, and (c) CCW rotating component of the near-inertial amplitude. For this particular run *c* was set to 1/f.

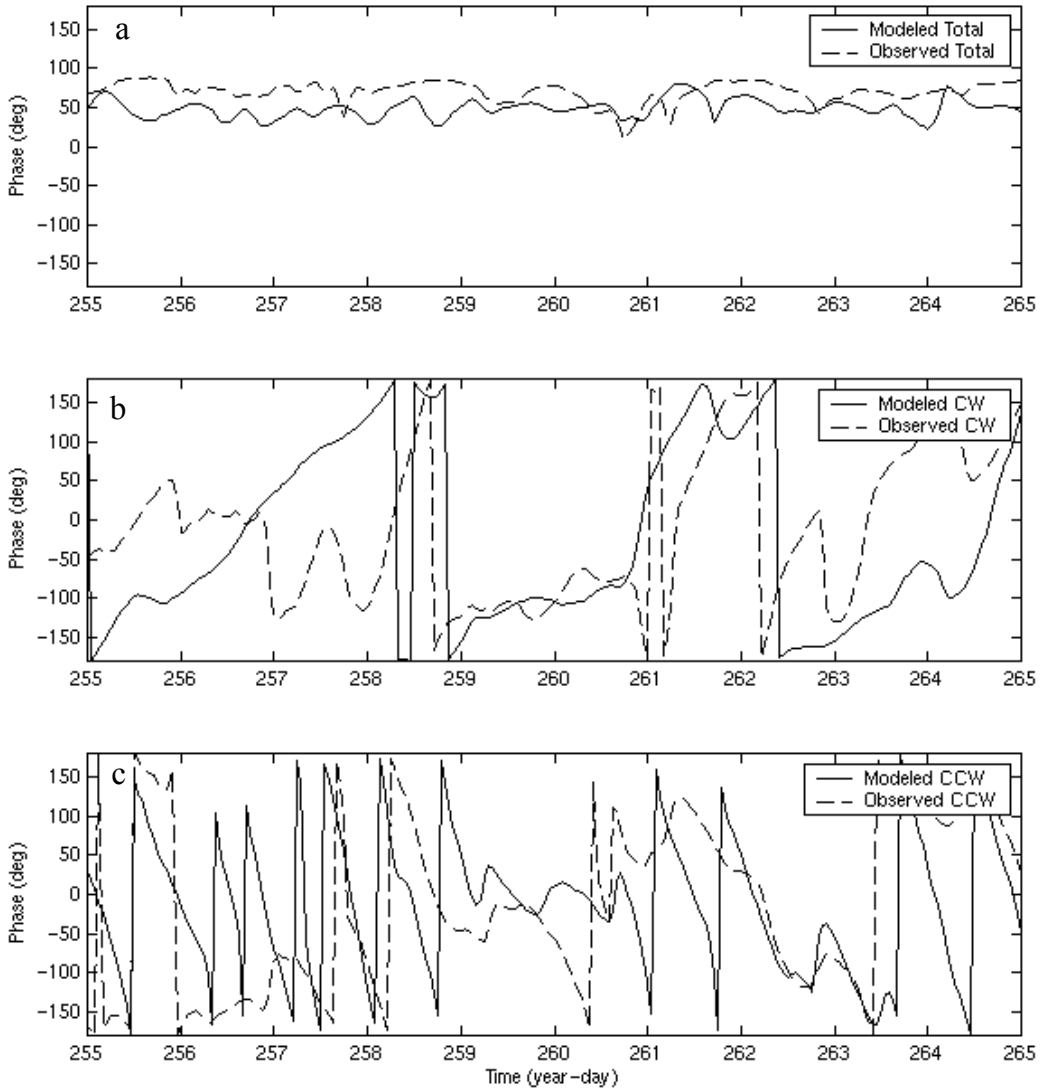

Figure 4.13. The (a) total, (b) CW rotating, and (c) CCW rotating component of the near-inertial phase. For this particular run *c* was set to 1/f.

with equal CW and CCW rotating components indicates that the depth-averaged current must be driven by forcing not included in the model. To more accurately predict the observed rectilinear response the model must include more realistic bottom friction and additional forcing.

4.4.2 Momentum balance

4.4.2.1 The governing equations

Since the observed rectilinear response is not a typical CW rotating near-inertial current, the following analysis describes the total sub-tidal response to the storm forcing. Fandry and Steedman (1994) use the depth averaged shallow water equations to predict the nearshore response to a tropical storm propagating perpendicular and parallel to the coast. In both simulations, the pressure gradient is an important term in the balance (Fandry and Steedman, 1994). Therefore, in addition to a more realistic bottom stress and wind stress, the modeled depth-averaged response to Floyd must include the pressure gradient. The governing equations of the improved model are:

$$\frac{\partial u}{\partial t} = -g\frac{\partial \eta}{dx} + fv + \frac{\tau_{wx}}{\rho H} - \frac{\tau_{bx}}{\rho H} \tag{4.5}$$

$$\frac{\partial v}{\partial t} = -g\frac{\partial \eta}{dy} - fu + \frac{\tau_{wy}}{\rho H} - \frac{\tau_{by}}{\rho H} \tag{4.6}$$

where u and v are the depth-averaged cross-shore and along-shore velocity components, f is the local Coriolis parameter, η is the sea surface height, ρ is the water density, H is the water depth, τ_{wx} (τ_{bx}) is the wind stress (bottom stress) in the cross-shore direction, and τ_{wy} (τ_{by}) is the wind stress (bottom stress) in the along-shore direction. The non-linear terms are not expected to be large for this forcing and response, and therefore are not

included in equations 4.5 and 4.6 (Shay and Elsberry, 1997). In the following analysis the acceleration (first term) and Coriolis force (third term) of equations 4.5 and 4.6 are calculated with the observed depth-averaged current.

Wind Stress. A more robust algorithm replaces the wind stress calculation described in equations 4.3 and 4.4. The TOGA-COARE2.6 algorithm, modified for high wind, uses the wind velocity, air and sea temperatures, atmospheric pressure, and the relative humidity to predict the magnitude of the wind stress, τ_w (Fairall et al., 1996). The direction of the wind stress is taken to be the wind direction.

Bottom Stress. The fifth term in equations 4.5 and 4.6 replaces the e-folding damping term in equations 4.1 and 4.2. Assuming a standard linear eddy viscosity, $K = \kappa u_* z$, the magnitude of the bottom stress (τ_b) can be represented as:

$$\tau_b = \rho u_*^2 \tag{4.7}$$

where u_* is the frictional velocity (Smith and Long, 1976; Forristall et al., 1977). Assuming a constant stress layer, we get the following expression for u_*:

$$u_* = \frac{(u_2 - u_1)\kappa}{\ln\left(\frac{z_2}{z_1}\right)} \tag{4.8}$$

where u_1 [z_1] and u_2 [z_2] are the raw velocity [height above the seafloor] of the bottom two ADCP bins. The frictional velocity, u_*, was then substituted into equation 4.7 to get the magnitude of the bottom stress, τ_b. The direction of the bottom stress is taken to be opposite the bottom current, u_1.

Pressure gradient. The sea surface slope, $\left(\frac{\partial \eta}{\partial x}, \frac{\partial \eta}{\partial y}\right)$, could not be measured directly at the offshore site. Instead it was inferred so that measured terms of model

equations would be in balance. This inferred pressure gradient was compared to the sea level observations from LEO-15 and the NOAA coastal sites. Using these equations the sub-tidal ocean response to the forcing before, during, and after the passing of tropical storm Floyd are described.

4.4.2.2 Before the storm

The depth-averaged cross-shore currents are very weak prior to the storm (Figure 4.14a). The dominant cross-shore balance is geostrophic between the cross-shore pressure gradient and Coriolis (Figure 4.14b). In the along-shore direction, the stronger currents are toward the southwest (Figure 4.15a). The along-shore balance is between the pressure gradient and bottom friction (Figure 4.15b). Since the inferred pressure gradient is a significant term in both momentum balances, it was compared to the measured sea-surface slope. This slope was calculated with the SLA measured at the offshore LEO-15 site and the coastal NOAA sites. Appropriate sites were chosen for the along-shore and cross-shore directions. Both the measured and inferred cross-shore pressure gradients have a negative value that geostrophically balances the along-shore current (Figure 4.14c and 4.14d). The observed slope is more variable with a mean rise of about 40 cm over 10 km. The inferred slope from the model is more stable with a rise of about 2 cm over the same 10 km. Since the measured pressure gradient would geostrophically balance a 4 m/s alongshore current and the inferred pressure gradient geostrophically balances the observed 20 cm/s alongshore current, the measured difference between the SLA at the offshore site and Atlantic City coastal site is not representative of the cross-shore gradient felt offshore. The alongshore pressure gradient was measured between the two coastal

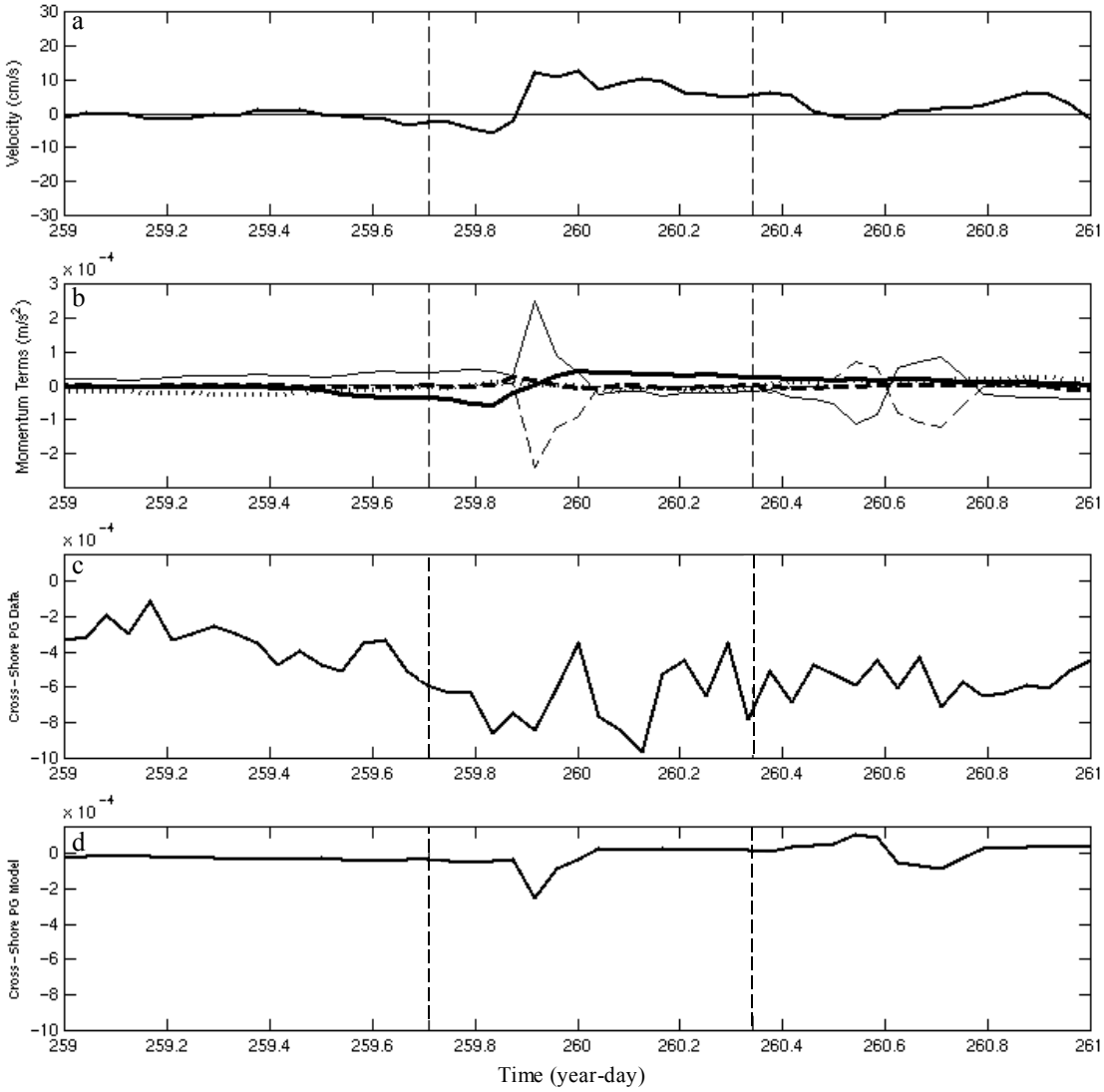

Figure 4.14. Cross-shore (a) depth-averaged velocity, (b) depth-averaged momentum balance, including the acceleration (heavy dashed), Coriolis (dot), wind stress (thick), bottom stress (thin dashed) and pressure gradient (thin) terms, (c) measured pressure gradient, and (d) inferred pressure gradient. The vertical dashed lines separate the data into the before, during and after storm regimes.

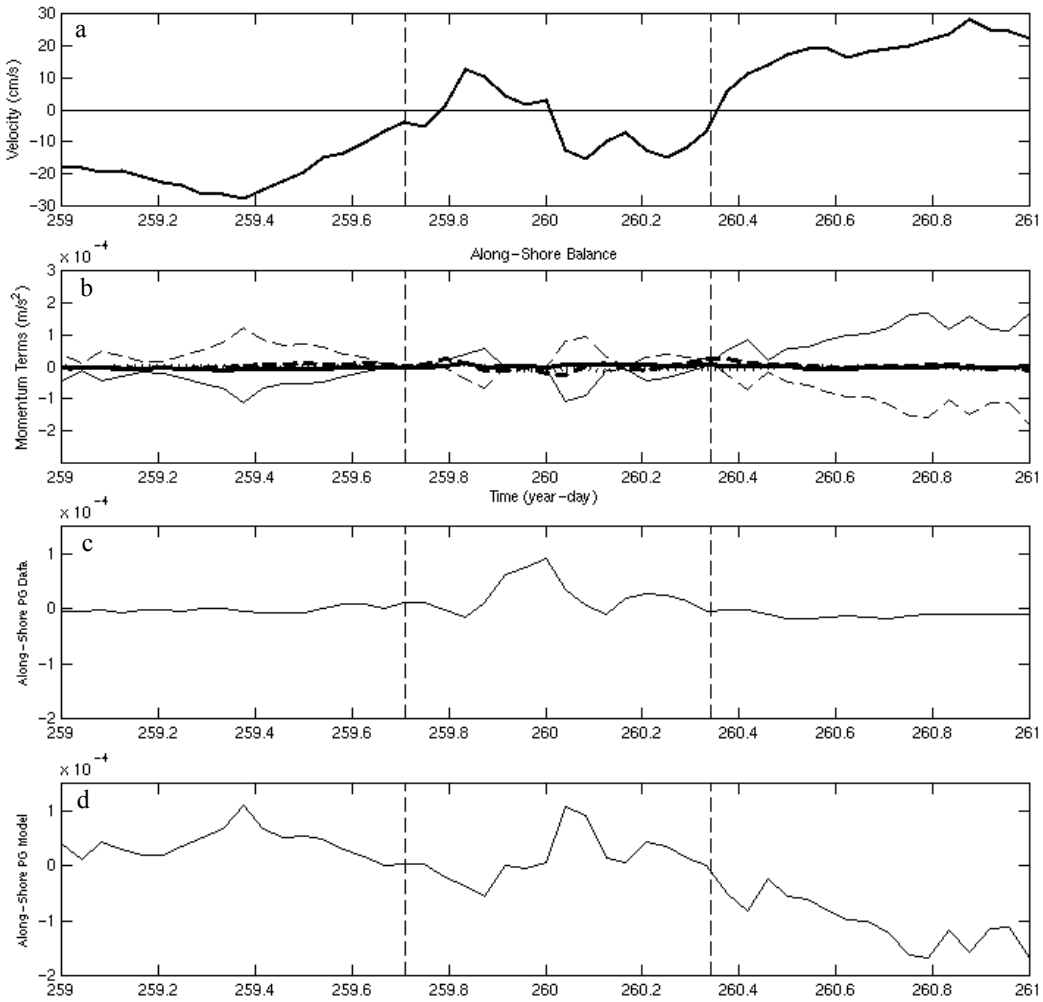

Figure 4.15. Along-shore (a) depth-averaged velocity, (b) depth-averaged momentum balance, including the acceleration (heavy dashed), Coriolis (dot), wind stress (thick), bottom stress (dashed) and pressure gradient (thin) terms, (c) measured pressure gradient, and (d) inferred pressure gradient. The vertical dashed lines separate the data into the before, during and after storm regimes.

sites in Atlantic City and Sandy Hook (Figure 4.1). The two coastal sites are separated by 115 km in the along-shore direction. In this direction, the inferred along-shore pressure gradient is larger than the measured gradient. The peak slope seen at yd 259.3750 is an 11 cm rise over 10 km, while the measured slope for that same time is very close to zero (Figure 4.13c and 4.13d).

According to the model, the pressure gradient is balanced by the measured bottom stress (Figure 4.13b). If we look at a simple two-term balance between the pressure gradient and bottom stress we get:

$$-g\frac{\partial \eta}{\partial y} = \frac{\partial}{\partial z}\left(\kappa u_* z \frac{\partial v}{\partial z}\right) \tag{4.9}$$

After integrating both sides with respect to depth we are left with:

$$-g\frac{\partial \eta}{\partial y} = \kappa u_* \frac{\partial v}{\partial z} \tag{4.10}$$

where η is the SLA and v is the depth dependent along-shore velocity component. A second integration leads to a linear velocity profile in z, as is often observed during strong storm events. Since the observed along-shore velocity profile before the storm is linear in the interior (Figure 4.16), the observed shear is used to calculate the magnitude of the compensating pressure gradient. Substituting this shear and the measured frictional velocity, u_*, into equation 4.10, we get a measure of the sea-surface slope that would balance the observed shear. With a slope of 11.5 cm over 10 km, the observed shear would balance a pressure gradient of the same order as the inferred pressure gradient predicted by the model. Since the measured sea-surface slope between Sandy Hook and Atlantic City underestimates this slope, the pressure gradient must be smaller scale than the 115 km that separates the two coastal sites.

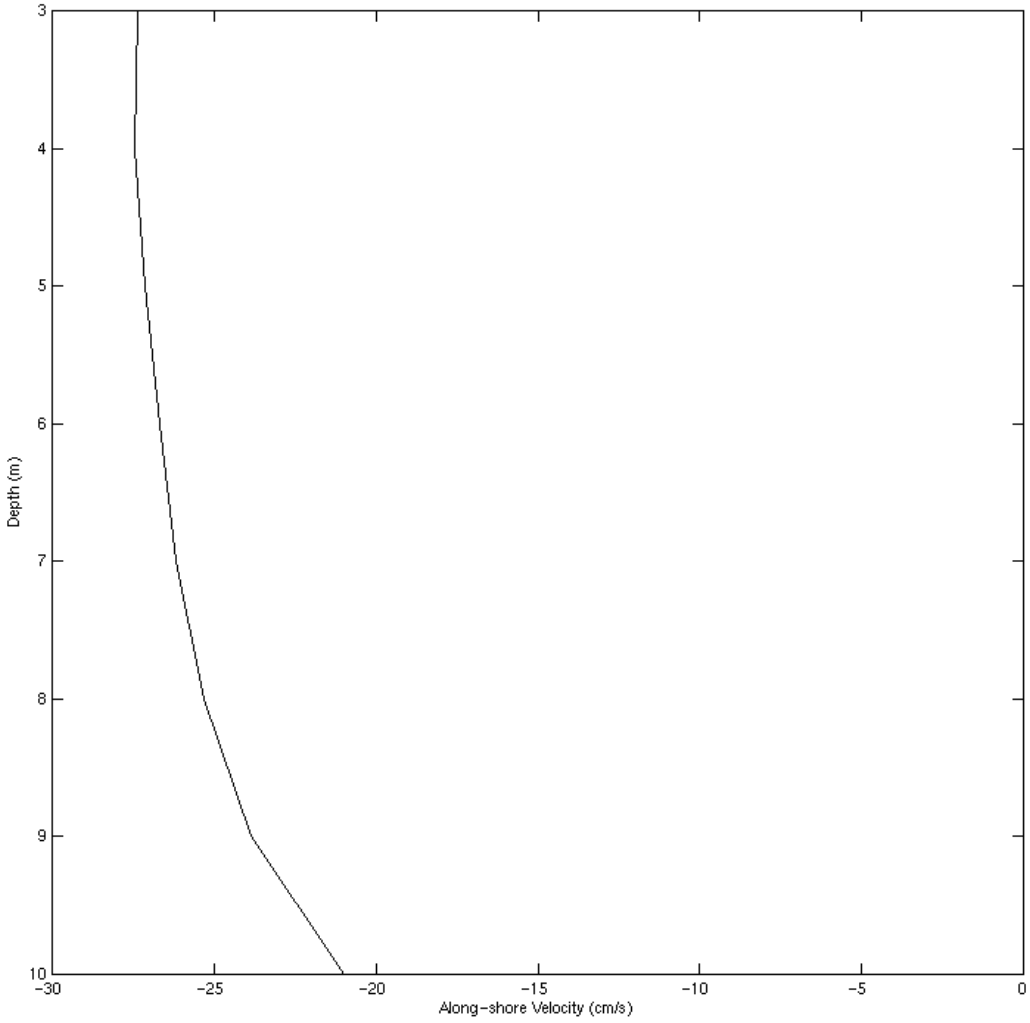

Figure 4.16. Along-shore ADCP profile on yd 259.3750. The linear shear in the interior of the water column is used in equation 4.10 to solve for the pressure gradient.

Atlantic City is not directly offshore of the LEO-15 site so the sea surface slope measured between Atlantic City and the CTD could be more representative of this small-scale along-shore slope rather than the cross-shore slope discussed previously. If the change in sea-level between Atlantic City and LEO is calculated over the alongshore distance of 15 km between sites rather than the cross-shore distance of 5 km, the slope is 13 cm over 10 km. This is in agreement with both the 11 cm rise of the inferred slope and the 11.5 cm rise calculated with the two-term balance. Therefore the sea-level slope measured between Atlantic City and the offshore site is more representative of the small-scale alongshore pressure gradient not the cross-shore pressure gradient originally thought. The current structure before the storm is dominated by an alongshore current forced by an along-shore pressure gradient and balanced by bottom friction.

4.4.2.3 During the storm

As Floyd approaches the study site, the cross-shore winds accelerate the flow onshore and strengthen the pre-existing pressure gradient. The geostrophic balance has weakened with the smaller Coriolis term and the major balance is now between the onshore wind stress and the inferred pressure gradient (Figure 4.14b). In the eye, the onshore winds decrease and the cross-shore current accelerates offshore with the pressure gradient. Coincident with the increased offshore flow, bottom friction increases to balance the large pressure gradient associated with the storm surge. The direction of the spike indicates that the surge is larger near the coast than offshore at the ADCP/CTD. Immediately after the eye, the sea-surface flattens and the weak offshore currents are again balanced primarily by the pressure gradient and the bottom stress. Since the storm

propagates so quickly through the study area, about 50 km/hr, the 15 km along-shore distance between Atlantic City and the LEO-15 site is covered in 18 minutes. Therefore, the sea-level difference measured between the two sites is now more representative of the cross-shore pressure gradient particular to the storm. Both the inferred and measured gradients indicate a larger surge near the coast coincident with the storm, however the measured slope is larger than the inferred (Figure 4.14c and 4.14d). The measured slope of 80 cm over 10 km is too large to be balanced by the measured terms offshore, indicating that near-shore processes must amplify the surge near the coast. This is consistent with long wave theory over irregular-shaped basins that suggests that the cross-shore slope of the storm surge is steeper over shallower water (Dean and Dalrymple, 1991). Dean and Dalrymple (1991) suggest that for a given bottom stress, the steeper the bottom slope, the steeper the storm surge near the coast. Therefore most of the measured 80 cm rise observed between the coastal and offshore sites could occur very close to shore. The 25 cm rise predicted offshore is more representative of the slope acting on the depth-averaged current in the deeper 12 m water column. The second peak seen in the measured pressure gradient, not predicted by the model, could be due to near-shore dynamics associated with the significant rainfall of tropical storm Floyd. A time series of the SLA measured at both Atlantic City and the offshore node clearly illustrates the larger surge near the coast, and the different SLA responses measured near the coast and offshore that leads to the second peak around yd 260.1 (Figure 4.17).

In the along-shore direction the current oscillates several times between northward and southward. The important terms throughout the passing of the storm are a combination of the bottom stress, pressure gradient and acceleration. As the storm

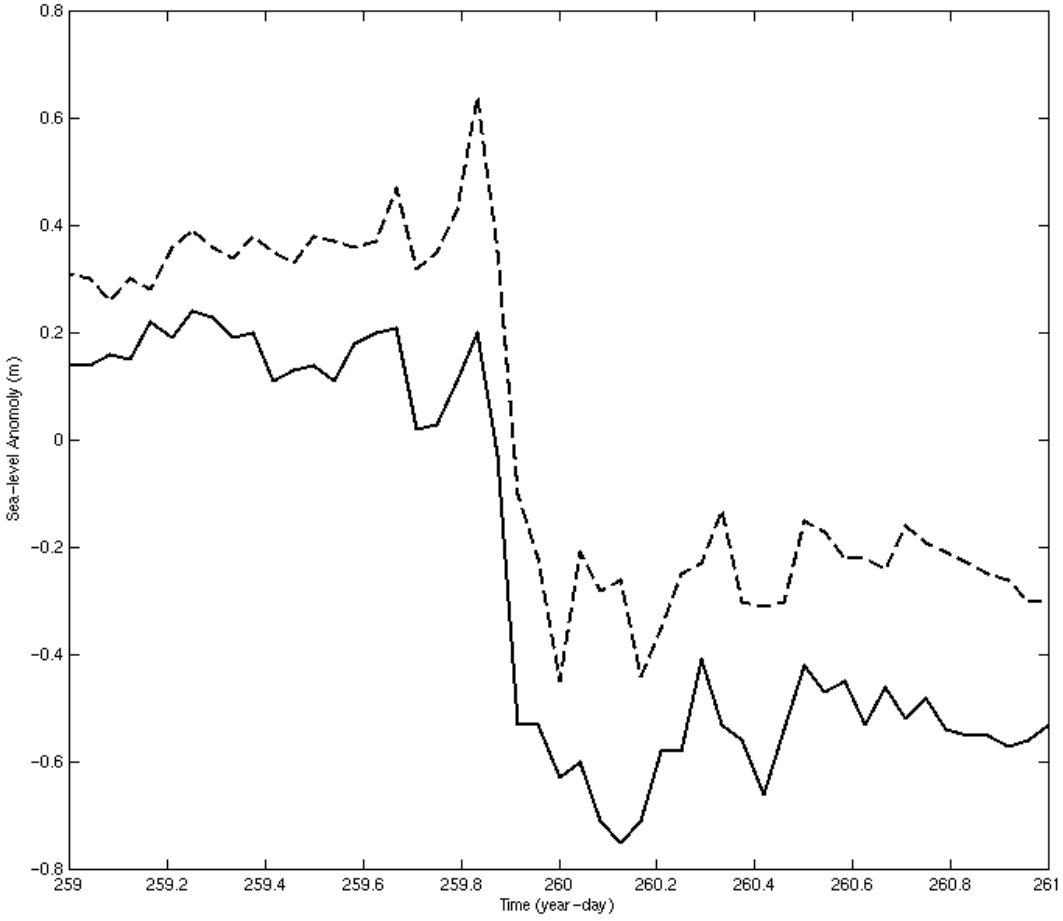

Figure 4.17. SLA measured at Atlantic City (dashed) and the offshore node (solid).

approaches, the surge south of the study site tilts the sea surface down toward the north. This is seen in the term balance as an acceleration to the north followed by a balance between the pressure gradient and bottom stress. Immediately after the storm, the surge moves through the site and the pressure gradient changes sign. This event starts as acceleration toward the south followed again by a balance between the pressure gradient and bottom stress. After the storm has left the area there is another acceleration toward the south that once again starts off as an acceleration followed by a balance between the pressure gradient and bottom stress. This small downwelling event is correlated with the rainfall (Figure 4.2e) and the bottom salinity minimum (Figure 4.3b). There is evidence of all three events in both the measured and inferred pressure gradients (Figure 4.15c and 4.15d). The largest pressure gradient is seen with the second event associated with a surge north of the site. Each dataset contains a slope on the order of 10 cm over 10 km. Since the peak is seen in both the small scale inferred pressure gradient and the larger scale measured pressure gradient, the scale of the forcing is large enough to be resolved over the 115 km that separates the two coastal sites. There is also evidence of the freshwater downwelling event seen after the storm in both the measured and inferred fields. This slope is shallower with an average rise of 4 cm over 10 km. During the storm the cross-shore currents are driven by the cross-shore winds and pressure gradient. The alongshore response is forced by the propagating storm surge and balanced by bottom friction.

4.4.2.4 After the storm

In the cross-shore direction, there is a multi-term balance between the wind stress, pressure gradient, Coriolis and bottom stress. The exception to this multi-term balance is between yd 260.4 and 260.8 when bottom stress balances the pressure gradient. In the alongshore direction there is a northward flowing current that is balanced primarily by the pressure gradient and bottom stress. In both the along-shore and cross-shore directions, the magnitude and structure of the inferred pressure gradient is not in agreement with the measured gradients (Figure 4.14 and 4.15). Since the model over-predicts the pressure gradient to balance the measured bottom friction, this disagreement suggests that the bottom friction may be overestimated.

The vertical structure of the detided velocity field through this period rotates about 80 degrees through the water column, indicating that the system is no longer acting as a single layer (Figure 4.18). Both the magnitude and direction of the ADCP profile show a two-layer system in which the surface layer is much less sheared than the bottom layer (Figure 4.18). Since the flow is stratified, the surface layer is separated from the bottom and no longer feels the effect of the bottom stress. So a surface layer model was set up to predict this response. The surface layer model equations are:

$$\frac{\partial u}{\partial t} = -g\frac{\partial \eta}{dx} + fv + \frac{\tau_{wx}}{\rho H} \tag{4.11}$$

$$\frac{\partial v}{\partial t} = -g\frac{\partial \eta}{dy} - fu + \frac{\tau_{wy}}{\rho H} \tag{4.12}$$

where we assume the stress at the interface is small compared to the other terms due to stratification. Based on the vertical current structure (Figure 4.18), the depth of the surface layer is taken to be 8 m. For comparison, the model was run through the entire record.

The surface model no longer predicts the balances observed before and during the storm. The small-scale along-shore pressure gradient driving the along-shore current before the storm is much smaller. Without bottom friction, the surge seen in the along-shore and cross-shore pressure gradient is also underestimated (Figure 4.19 and 4.20). Before and during the storm, the bottom friction is an important term in the dynamical response. After the storm, however, the surface layer model better predicts the pressure gradient associated with this two-layer system. The oscillation seen in the cross-shore direction and the erroneously large along-shore pressure gradient are no longer predicted by this model (Figure 4.19 and 4.20). Instead the along-shore flow is primarily balanced by acceleration and the pressure gradient. Even though the water column is largely isothermal (Figure 4.3a), the large input of freshwater by the storm into the system stratifies the fluid. Since the temperature gradient after the storm is negative (Figure 4.3a), the water column must be comprised of a cold, fresher layer over a warm, more saline layer. With this surface layer model, the inferred and measured along-shore pressure gradients indicate a rise of about 1 cm over 10 km. Since the same sea-surface slope is also observed between Atlantic City and Sandy Hook, the slope is large scale and indicates a small downward tilt toward the Bight apex following the storm. The structure of the current response after the storm is more representative of a two-layer flow in which the acceleration of the surface layer is balanced by the along-shore pressure gradient.

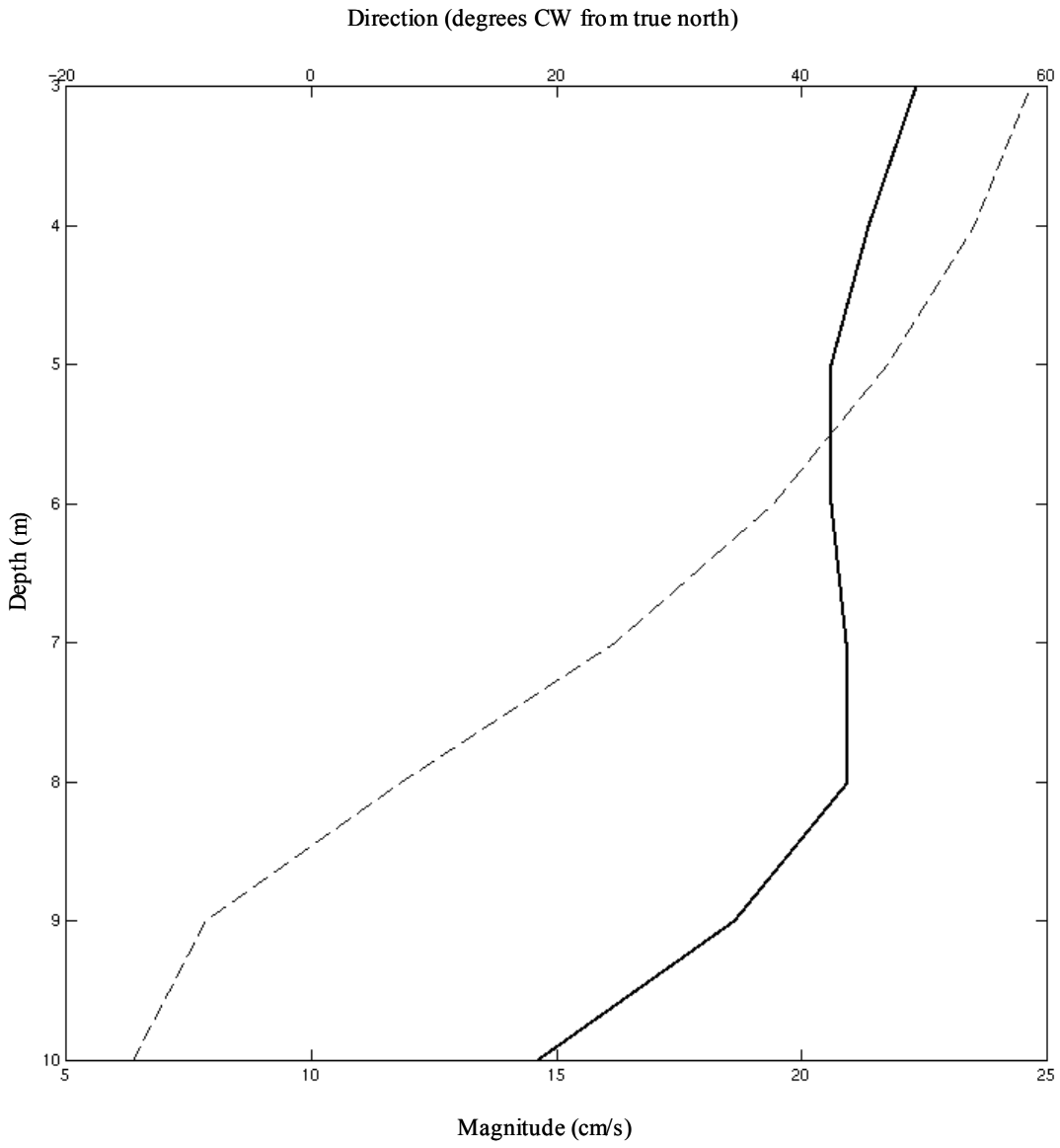

Figure 4.18. Vertical structure of the magnitude (solid) and direction (dashed) of the two layer flow observed after Floyd.

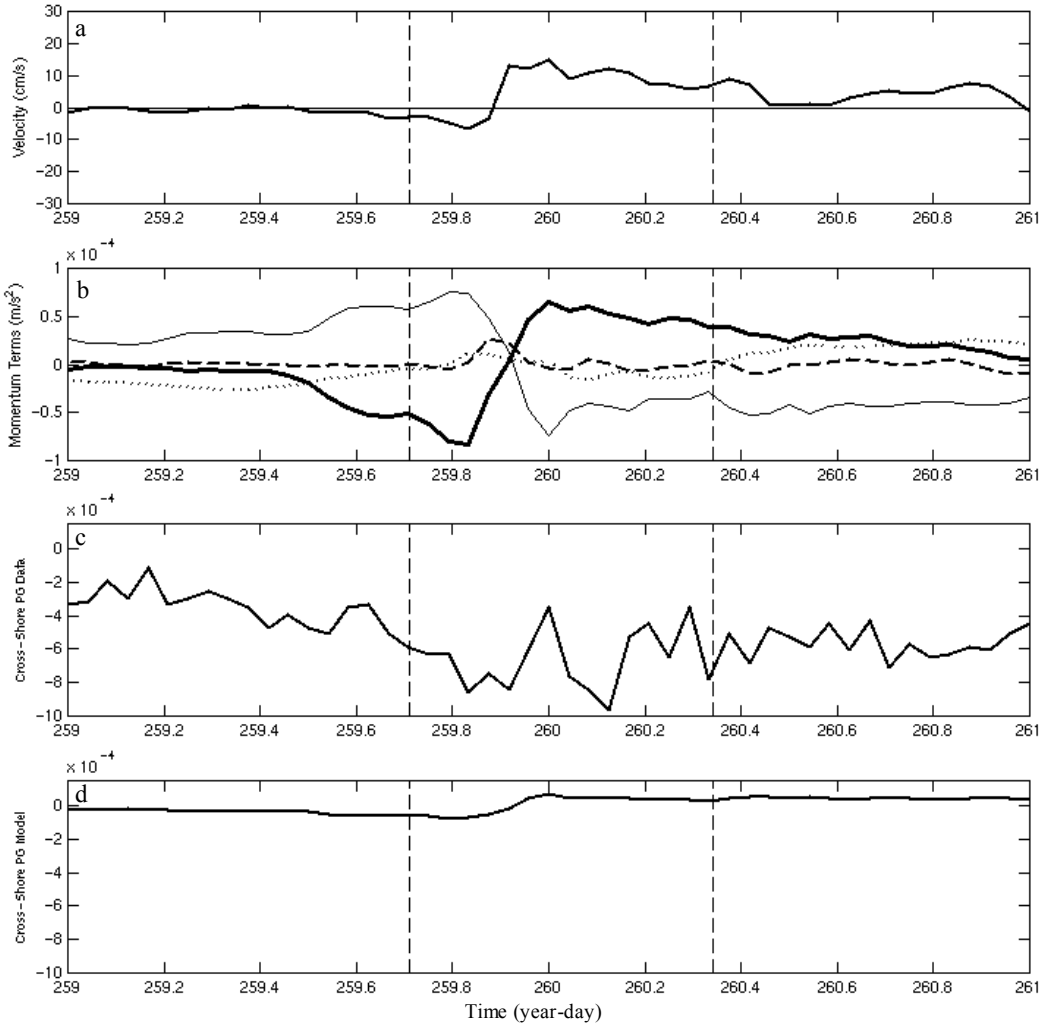

Figure 4.19. Cross-shore (a) depth-averaged velocity, (b) surface layer momentum balance, including the acceleration (heavy dashed), Coriolis (dot), wind stress (thick), and pressure gradient (thin) terms, (c) measured pressure gradient, and (d) inferred pressure gradient. The vertical dashed lines separate the data into the before, during and after storm regimes.

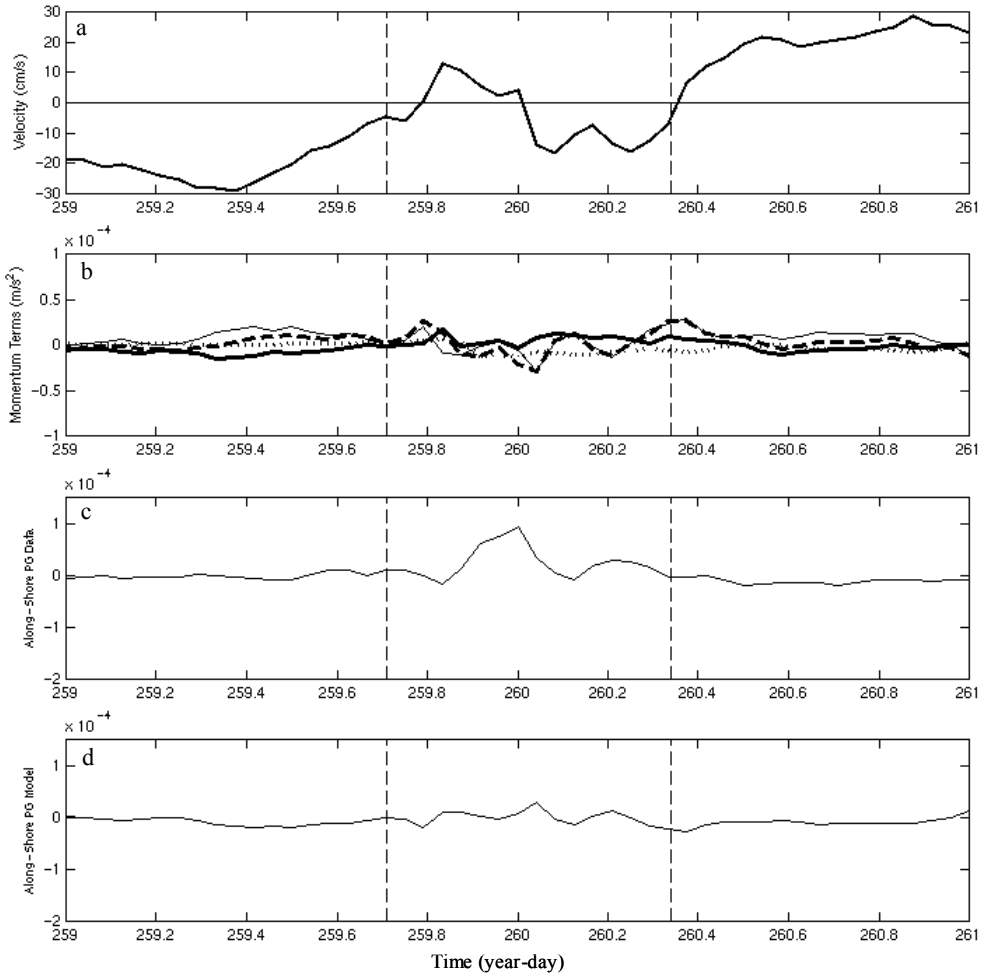

Figure 4.20. Along-shore (a) depth-averaged velocity, (b) surface layer momentum balance, including the acceleration (heavy dashed), Coriolis (dot), wind stress (thick), and pressure gradient (thin) terms, (c) measured pressure gradient, and (d) inferred pressure gradient. The vertical dashed lines separate the data into the before, during and after storm regimes.

The stratification induced by the large rain event reduces the effect of friction on the observed response.

4.4.3 Energy balance

The energy pathways during tropical storm Floyd were identified with a work equation based on the depth-averaged model described in equations 4.5 and 4.6. The work done by each term was calculated by multiplying each term by velocity so that:

$$\frac{\partial KE_x}{\partial t} = -g\frac{\partial \eta}{dx} \bullet u + fv \bullet u + \frac{\tau_{wx}}{\rho H} \bullet u - \frac{\tau_{bx}}{\rho H} \bullet u \qquad (4.13)$$

$$\frac{\partial KE_y}{\partial t} = -g\frac{\partial \eta}{dy} \bullet v - fu \bullet v + \frac{\tau_{wy}}{\rho H} \bullet v - \frac{\tau_{by}}{\rho H} \bullet v \qquad (4.14)$$

Each term on the right side of the equations is the work done by the respective term in equations 4.5 and 4.6. Using these equations, the work done by the wind and bottom friction was compared to the change in kinetic Energy (KE) of the entire system with time. The following discussion focuses on the energy input and dissipation particular to the storm.

*Cross-shore Energetics***.** The kinetic energy of the cross-shore current component is very weak throughout most of the study period except for the peak coincident with the eye of the storm (Figure 4.21a). As the storm approaches, the cross-shore wind adds energy to the system without changing the kinetic energy (Figure 4.21b). Instead the wind work builds up the potential energy of the system in the form of a pressure gradient. It isn't until the wind dies in the storm eye that this potential energy is turned into kinetic. Following the peak in kinetic energy, the bottom friction work peaks, quickly dissipating the energy (Figure 4.21c).

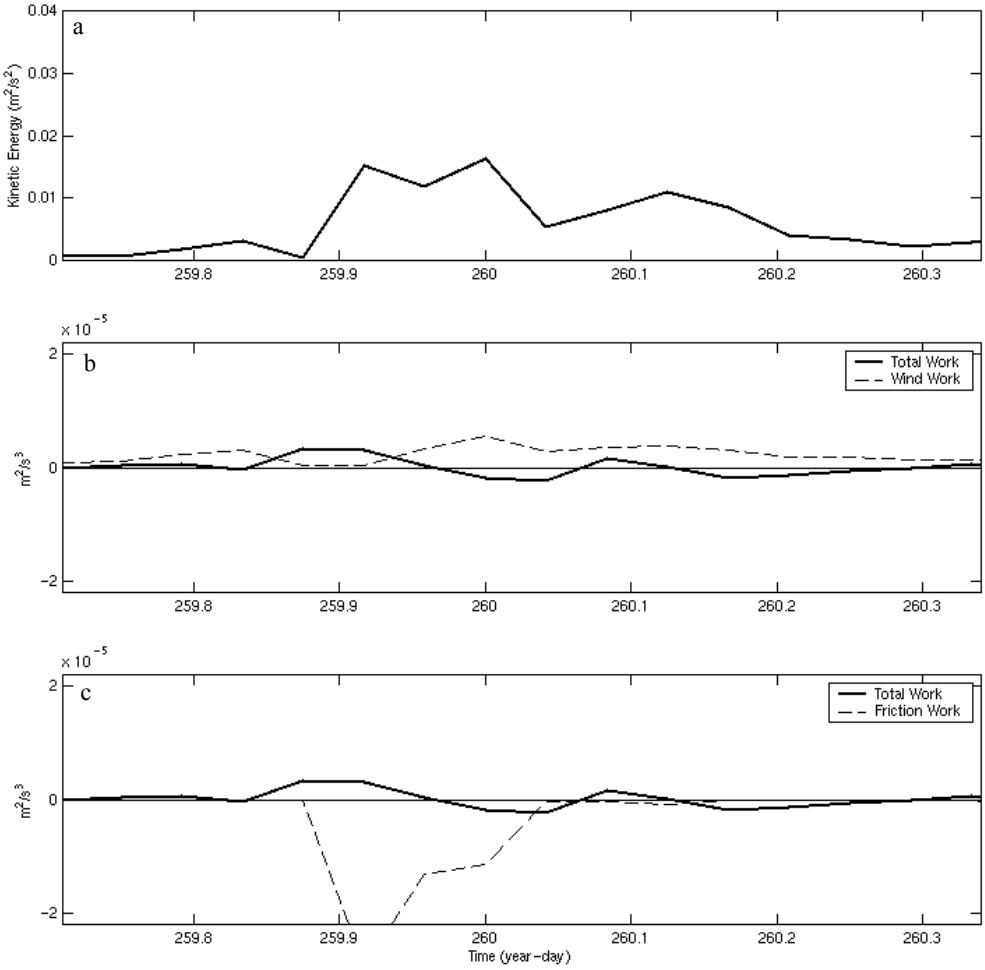

Figure 4.21. Cross-shore (a) kinetic energy, (b) work done by the wind, and (c) work done by bottom friction. The total work is quantified as the change in kinetic energy (equation 4.13).

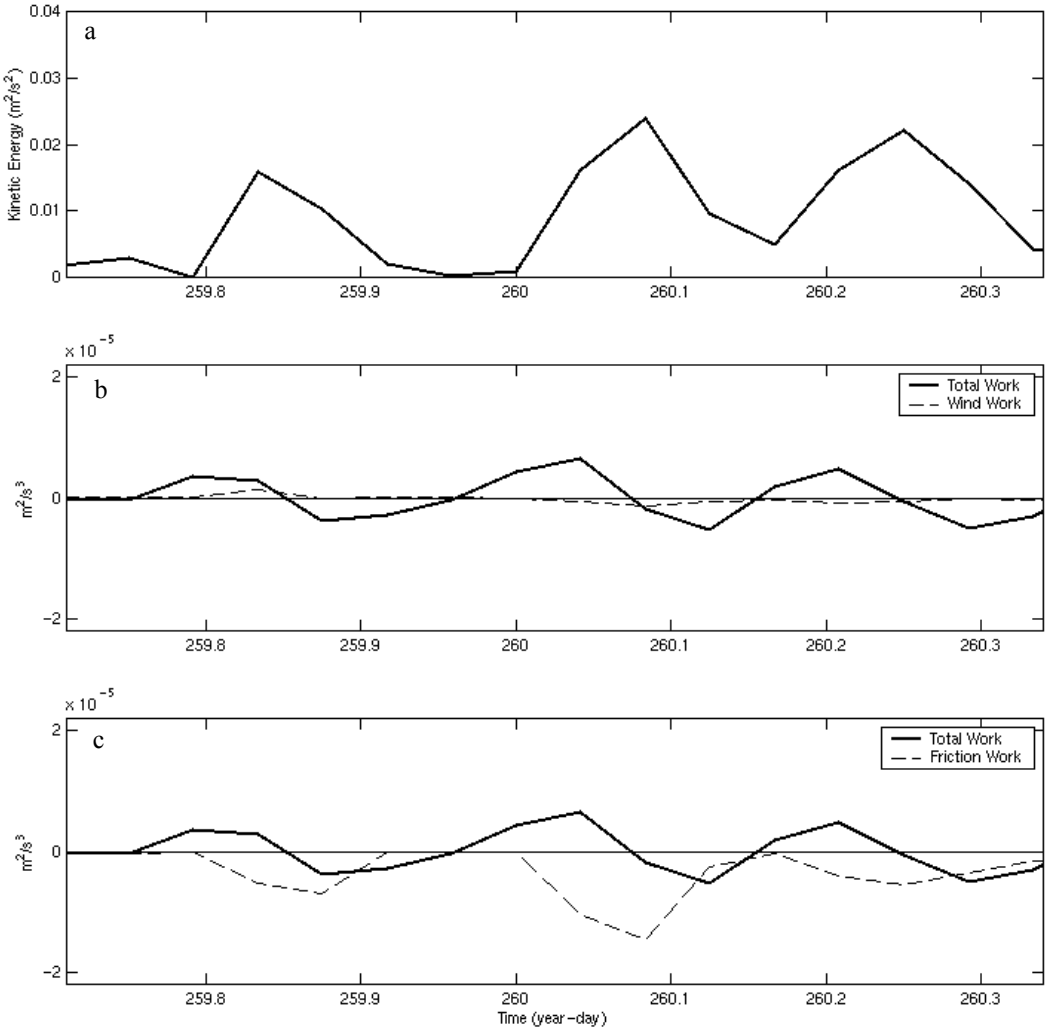

Figure 4.22. Along-shore (a) kinetic energy, (b) work done by the wind, and (c) work done by bottom friction. The total work is quantified as the change in kinetic energy (equation 4.14).

Along-shore Energetics. The along-shore currents are more energetic than that seen in the cross-shore balance (Figure 4.22a). Since the wind forcing during the storm is predominately in the cross-shore direction, the work done by the along-shore wind stress is very small throughout the study period (Figure 4.22b). During the storm, kinetic energy is added and taken away from the system with each oscillation observed in the previous section. Therefore the energy added to the system is from the changing sea-surface slope generated by the cross-shore winds and the storm surge. Like the cross-shore direction, a peak in bottom friction work follows each input of kinetic energy so that the energy put into the system by the oscillating pressure gradient is quickly taken out by bottom friction (Figure 4.22c).

Both the along-shore and cross-shore balances indicate the importance of the bottom friction. The energy put into the system by the cross-shore wind stress and propagating storm surge is quickly taken out by the bottom stress. In this shallow well-mixed ocean there is no time for the energy to propagate away before the bottom stress dissipates the energy. For this reason, the response to this storm is shorter relative to the modeled and observed responses of a deeper more strongly stratified ocean.

4.5 Conclusions

The shallow well-mixed response to the passing of tropical storm Floyd is a short episodic event. The effect of the storm perturbs the current structure for about 48 hours before the seasonal climatology returns. While there is energy in the near-inertial response, it is not the typical clockwise ringing seen with the baroclinic response of a deeper, stratified ocean. Instead the along-shore rectilinear response is representative of

the total detided response. Initially cross-shore winds are balanced by the pressure gradient, adding potential energy to the system. When the winds die, the potential energy turns into kinetic and the sea-surface slope flattens and reverses sign. This oscillating sea surface slope propagates up the coast with the storm. The moving surge forces an along-shore rectilinear response driven by the pressure gradient and balanced by bottom friction. In both components, bottom friction quickly dissipates the energy. Unlike the near-inertial response that propagates out of the system within several inertial periods, a balance between the barotropic pressure gradient and bottom friction drives this shallow water response.

5.0 SUMMARY AND CONCLUSIONS

The utility of HF radar as a tool to monitor the coastal ocean was presented here on both seasonal and event time scales. Using ADCP comparisons, system accuracy is shown to depend on the distortion of the measured pattern. This distortion, related to the interaction between the individual elements, is predominately the consequence of the local environment. In practice an ideal environment without interference is not common in the field. For that reason the antenna-based system must be calibrated with the measured antenna pattern. ADCP comparisons show that the calibrated data is more accurate when the pattern was distorted. The improved accuracy is related to the improved bearing estimate of the MUSIC algorithm. To maximize any HF radar's usefulness for scientific and operational coastal monitoring, the antenna patterns for each site must be measured and, if distorted, these patterns should be used to calibrate the surface current measurements for more accurate observations.

Long-term deployments of a calibrated HF radar system provide observations of coastal variability on seasonal scales. The most significant seasonal signal observed off the coast of New Jersey is between the summer stratification and winter mixed seasons. Stratification has been shown to significantly influence the observed surface current response to local forcing over these longer scales. When the water column is stratified, the surface layer is separated from the bottom by a strong thermocline. This surface layer is significantly correlated with the local wind forcing with the highest correlated currents to the right of the wind. The vertical structure of the correlation indicates a two-layer system in approximate Ekman balance with a surface layer that flows to the right of the wind and the bottom layer that flows to the left. The along-shore forcing and strong

stratification lead to frequent upwelling/downwelling events that are characterized with a relatively steady flow. The shear of this steady response has horizontal correlation scales dependent on both local topography and stratification.

In contrast, the mixed regime response tends to be aligned with the coast and less dependent on the local wind forcing. Since the water column is mixed through much of the year and the mean stratified response is close to zero, the mixed mean resembles the annual mean having a general flow toward the southwest with perturbations around the local topography. The vertical structure of the correlation indicates that the highest wind correlated current is to the left of the forcing with a slight rotation further left with depth. This rotation is an indication that the entire water column is acting as a single frictional layer influenced by bottom and surface stresses. As a single layer, the surface response is steered by local topography on several scales. At the larger 20 km scale, the alongshore topography orients the major axis of the variability along the coast. The general alongshore response is further modified within the HF radar grid by the smaller-scale topography on the order of 5 km.

Over seasonal scales, stratification clearly influences the response of the surface currents to local forcing. The surface layer of the stratified water column, strongly correlated with the wind, has complicated horizontal shears linked to local topography. The surface of the mixed water column is no longer separated from the bottom by a strong thermocline and is significantly influenced by the underlying topography, especially where the depth gradients are maximum.

Within this seasonal climatology, strong events like tropical storms can temporarily change the expected current structure. It is shown that tropical storm Floyd

perturbs the seasonal current structure for about two days before the mixed regime climatology returns. The short-lived response is not the typical baroclinic ringing observed in deeper more stratified oceans. Instead the barotropic response is rectilinear with a time scale of the same order as the passing storm. Energy is added to the system by both the cross-shore winds and the storm surge associated with the atmospheric pressure field. This sets up an initial surge followed by a significant drop in sea level that moves up the coast with the storm. The oscillating sea-surface associated with this moving surge forces an along-shore rectilinear response driven by the pressure gradient and balanced by bottom friction. Within 36 hours of the initial storm forcing the event is dissipated by bottom friction and the current structure returns to that observed throughout the mixed regime.

The calibrated surface current observations have shown that the seasonal scale response to local forcing, driven by stratification and local topography, can be interrupted by short energetic events like tropical storm Floyd. The spatial HF radar time series data provided the observations necessary to characterize the spatial and temporal structure of the event scale response within the context of the longer seasonal scale variability.

REFERENCES

Austin, J.A., 1999: The role of the alongshore wind in the heat balance of the North Carolina inner shelf. *J. Geophys. Res*., **104**, 18187-18203.

Barrick, D.E, 1972: First-order theory and analysis of mf/hf/vhf scatter from the sea. *IEEE Trans. Antennas Propag*, **AP-20**, 2-10.

-----, M.W. Evens and B.L. Weber, 1977: Ocean surface currents mapped by radar. *Science*, **198**, 138-144.

----- and B.J. Lipa, 1986: Correcting for distorted antenna patterns in CODAR ocean surface measurements. *IEEE J. Ocean. Eng*, **OE-11**, 304-309.

----- and B.J. Lipa, 1996: Comparison of direction-finding and beam-forming in hf radar ocean surface current mapping. Phase 1 SBIR final report. Contract No. 50-DKNA-5-00092. National Oceanic and Atmospheric Administration, Rockville, MD.

----- and B.J. Lipa, 1997: Evolution of bearing determination in hf current mapping radars. *Oceanography*, **10**, 72-75.

----- and B.J. Lipa, 1999: Radar angle determination with MUSIC direction finding. United States Patent, No. 5,990,834.

Barth, J. A., 1994: Stability of a coastal upwelling front, 2, model results and comparisons with observations. *J. Geophys. Res*., **99,** 10857-10883.

Beardsley, R.C. and W.C. Boicourt, 1981: On estuarine and continental-shelf circulation in the Middle Atlantic Bight. *Evolution in Physical Oceanography*, B. A. Warren and C. Wunsch, Eds., The MIT Press, 198-233.

-----, ----- and D. V. Hansen, 1976: Physical oceanography of the Middle Atlantic Bight. *Limnology and Oceanography, Special Symposium,* **2,** 20-34.

----- and D. B. Haidvogel, 1981: Model studies of wind-driven transient circulation in the Middle Atlantic Bight, part1: adiabatic boundary conditions. *J. Phys. Oceanogr.,* **11**, 355-375.

----- and S. J. Lentz, 1987: The Coastal Ocean Dynamics Experiment collection: an introduction. *J. Geopys. Res.,* **92**, 1455-1463.

----- and C. D. Winant, 1979: On the mean circulation in the Mid-Atlantic Bight. *J. Phys. Oceanogr.,* **9**, 612-619.

Bigelow, H. B., 1933: Studies of the waters on the continental shelf, Cape Cod to Chesapeake Bay. I. The cycle of temperature. *Papers in Physical Oceanography and Meteorology* 2:4, 135pp.

----- and M. Sears, 1935: Studies of the waters on the continental shelf, Cape Cod to Chesapeake Bay. II. Salinity. *Papers in Physical Oceanography and Meteorology* 4:1, 94pp.

Bjorkstedt, E. and J. Roughgarden. 1997: Larval transport and coastal upwelling: an application of HF radar in ecological research. *Oceanography*, **10**, 64-67.

Breivik, O. and O. Sætra, 2001: Real time assimilation of hf radar currents into a coastal ocean model. *J. Marine Systems*, **28**, 161-182.

Brink, K. H. 1997: Observational coastal oceanography. National Science Foundation OCE Workshops.

-----, 1998: Wind-driven currents over the continental shelf. The Sea: The Global Coastal Ocean Processes and Methods (ed. K. H. Brink and A. R. Robinson). 3-20.

----- , D. Halpern, and R. L. Smith, 1980: Circulation in the Peruvian upwelling system near 15° S. *J. Geophys. Res*., **85**, 4036-4048.

Brooks, D. A., 1983: The wake of hurricane Allen in the western Gulf of Mexico. *J. Phys. Oceanogr*., **13**, 117-129.

Burke, G. J. , 1992: Numerical Electromagnetics Code -- NEC-4, UCRL-MA-109338, Parts I & II, Lawrence Livermore National Laboratory, Livermore, CA.

Chapman, D. C. and R. C. Beardsley, 1989: On the origin of shelf water in the Middle Atlantic Bight. *J. Phys. Oceanogr.*, **19**, 384-391.

Chapman, R.D. and H.C. Graber, 1997: Validation of hf radar measurements. *Oceanography*, **10**, 76-79.

-----, L.K. Shay, H.C. Graber, J.B. Edson, A. Karachintsev, C.L. Trump and D.B. Ross, 1997: On the accuracy of hf radar surface current measurements: intercomparisons with ship-based sensors. *J. Geophys. Res*, **102**, 18,737-18,748.

Chant, R. J., 2001: Evolution of near-inertial waves during an upwelling event on the New Jersey inner shelf. *J. Phys. Oceanogr.*, **31**, 746-763.

Crombie, D.D., 1955: Doppler spectrum of sea echo at 13.56 Mc/s. *Nature*, **175**, 681-682.

Davis, R. E. and P. S. Bogden, 1989: Variability on the California shelf forced by local and remote winds during the Coastal Ocean Dynamics Experiment. *J. Geophus. Res.*, **94**, 4763-4783.

Dean, R. G. and R. A. Dalrymple, 1991: Storm Surge. *Water Wave Mechanics for Engineers and Scientists.* P. L. Liu, Ed, World Scientific,157-163.

Ekman, V. W., 1905: On the influence of the earth's rotation on ocean currents. *Ark. Mat. Astron. Fys*. **2**, 1-53.

Fernandez, D.M., H.C. Graber, J.D. Paduan and D. E. Barrick, 1997: Mapping wind direction with hf radar. *Oceanography*, **10**, 93-95.

----- and J.D. Paduan, 1996: Simultaneous CODAR and OSCR measurements of ocean surface currents in Monterey Bay. Proceedings, IEEE IGARSS '96, Lincoln, Neb, **3**, 1746-1750.

Fairall, C. W., E. F. Bradley, D. P. Rogers, J. B. Edson and G. S. Young, 1996: Bulk parameterization of air-sea fluxes for TOGA COARE. *J. Geophys. Res.,* **101**, 3747-3764.

Fandry, C. B. and R. K. Steedman, 1994: Modelling the dynamics of the transient, barotropic response of continental shelf waters to tropical cyclones. *Cont. Shelf Res.*, **14**, 1723-1750.

Forristall, G. Z., R. C. Hamilton and V. J. Cardone, 1977: Continental shelf currents in tropical storm Delia: observations and theory. *J. Phys. Oceanogr.*, **7**, 532-546.

Furukawa, K. and M.L. Heron, 1996: Vortex modeling and observation of a tidally induced jet. *Coastal Engineering*, Japan Society of Civil Engineering, **43**, 371-375.

Geernaert, G. L. and S. E. Larsen, 1998: Air-sea interaction in the coastal zone. The Sea: The Global Coastal Ocean Processes and Methods (ed. K. H. Brink and A. R. Robinson), 89-112.

Glenn, S.M., W. Boicourt, B. Parker and T.D. Dickey, 2000: Operational observation networks for ports, a large estuary and an open shelf. *Oceanography*, **13**, 12-23.

-----, M. F. Crowley, D. B. Haidvogel and Y. T. Song, 1996: Underwater observatory captures coastal upwelling events off New Jersey. *EOS*, **77**, 233-236.

-----, T.D. Dickey, B. Parker and W. Boicourt, 2000: Long-term real-time coastal ocean observation networks. *Oceanography*, **13**, 24-34.

Graber, H.C., B.K. Haus, L.K. Shay and R.D. Chapman, 1997: Hf radar comparisons with moored estimates of current speed and direction: expected differences and implications. *J. Geophys. Res*, **102**, 18,749-18,766.

----- and M.L. Heron, 1997: Wave height measurements from hf radar. *Oceanography*, **10**, 90-92.

----- and C. B. Limouzy-Paris, 1997: Transport patterns of tropical reef fish larvae by spin-off eddies in the straits of Florida. *Oceanography*, **10,** 68-71.

Grassle, J.F., S.M. Glenn and C. von Alt, 1998: Ocean observing systems for marine habitats. *OCC '98 Proceedings*, Marine Technology Society, November, 567-570.

Halpern, D., 1976: Structure of a coastal upwelling event observed off Oregon during July 1973. *Deep Sea Res*., **23,** 495-508.

-----, 1977: Description of wind and of upper ocean currents and temperature variation on the continental shelf off Northwest Africa during March and April 1977. *J. Phys. Oceanogr*., **7,** 422-430.

Haus, B. K., H. C. Garber, and L. K. Shay, 1997: Synoptic measurements of dynamic ocean features. *Oceanography*, **10,** 45-48.

Hicks, D. C. and J. R. Miller, 1980: Meteorological forcing and bottom water movement off the northern New Jersey coast. *Estuarine and Coastal Science*. **II**. 563-571.

Keen, T. R. and S. M. Glenn, 1995: A coupled hydrodynamic-bottom boundary layer model of storm and tidal flow in the Middle Atlantic Bight of North America. *J. Phys. Oceanogr.*, **25**, 391-406.

----- and -----, 1999: Shallow water currents during hurricane Andrew. *J. Geophys. Res.,* **104**, 23443-23458.

Kohut, J. T., S. M. Glenn and D. E. Barrick, 1999: SeaSonde is Integral to Coastal Flow Model Development. *Hydro International,* **3**, 32-35.

-----, S.M. Glenn and D.E. Barrick, 2001: Multiple hf-radar system development for a regional longterm ecosystem observatory in the New York bight. *American Meteorological Society: Fifth Symposium on Integrated Observing Systems*, 4-7.

Kosro, P.M., J.A. Barth and P.T. Strub, 1997: The coastal jet: observations of surface currents over the Oregon continental shelf from hf radar. *Oceanography*, **10**, 53-56.

Kundu, P. K., 1984: Generation of coastal inertial oscillations by time-varying wind. *J. Phys. Oceanogr.*, **14**, 1901-1913.

-----, 1986: A two-dimensional model of inertial oscillations generated by a propogating wind field. *J. Phys. Oceanogr.*, **16**, 1399-1411.

Laws, K., D.M. Fernandez and J.D. Paduan, 2001: Simulation-based evaluations of hf radar ocean current algorithms. *J. Oceanic Engin.*, **25**, 481-491.

Lipa, B.J. and D.E. Barrick, 1983: Least-squares methods for the extraction of surface currents from CODAR cross-loop data: application at ARSLOE. *IEEE J. Ocean. Engr.*, **OE-8**, 226-253.

----- and D.E. Barrick, 1986: Extraction of sea state from hf-radar sea echo: mathematical theory and modeling. *Radio Sci*, **21**, 81-100.

Magnell, B. A., S. L. Spiegel, R. I. Scarlet, and J. B. Andrews, 1980: The relationship of tidal and low frequency currents on the north slope of Georges Bank. *J. Phys. Oceanogr.,* **10,** 1200-1212.

Mayer, D. A., H. O. Mofjeld and K. D. Leaman, 1981: Near-inertial waves observed on the outer shelf in the Middle Atlantic Bight in the wake of hurricane Belle. *J. Phys. Oceanogr.*, **11**, 87-106.

Miller, A. R., 1952: A pattern of surface coastal circulation inferred from surface salinity-temperature data and drift bottle recoveries. *W.H.O.I. Technical Report 52-28*, Woods Hole Oceanographic Institution, Woods Hole, Massachusetts, 14 pp.

Moores, C. N. K., J. Fernandez-Partagas and J. F. Price, 1976: Meteorological forcing fields of the New York Bight (first year's progress report). Tech. Rep. TR76-8, Rosenstiel School of Marine and Atmospheric Science, University of Miami.

Münchow, A. and R. J. Chant, 2000: Kinematics of inner shelf motions during the summer stratified season off New Jersey. *J. Phys. Oceanogr.*, **30**, 247-267.

Narimousa, S. and T. Maxworthy, 1987: Coastal upwelling on a sloping bottom: the formation of plumes, jets and pinched-off cyclones. *J. Fluid Mech.,* **176,** 169-190.

Oke , P.R., J.S. Allen, R.N. Miller, G.D. Egbert and P.M. Kosro, 2000: Assimilation of surface velocity data into a primitive equation coastal ocean model. *J. Geophys. Res*. In Press.

Ou, H. W., R. C. Beardsley, D. Mayer, W. C. Boicourt and B. Butman, 1981: An analysis of subtidal fluctuations in the Middle Atlantic Bight. *J. Phys. Oceanogr.*, **11**, 1383-1392.

Paduan, J.D., D.E. Barrick, D.M. Fernandez, Z. Hallok and C.C. Teague, 2001: Improving the accuracy of coastal hf radar current mapping. *Hydro International*, **5**, 26-29.

-----, L.K. Rosenfeld, S.R. Ramp, F. Chavez, C.S. Chiu and C.A. Collins, 1999: Development and maintenance of the ICON observing system in Monterey Bay. *Proceedings, American Meteorological Society's Third Conference on Coastal Atmospheric and Oceanic Prediction and Processes*, New Orleans, LA, 3-5 November, 226-231.

----- and M.S. Cook, 1997: Mapping surface currents in Monterey Bay with CODAR-type hf radar. *Oceanography*, **10**, 49-52.

----- and H.C. Graber, 1997: Introduction to high-frequency radar: reality and myth. *Oceanography*, **10**, 36-39.

----- and L. K. Rosenfeld, 1996: Remotely sensed surface currents in Monterey Bay from shore-based HF-radar (CODAR). *J. Geophys. Res*., **101**: 20669-20686.

-----, R. A. De Szoeke and R. A. Weller, 1989: Inertial oscillations in the upper ocean during the Mixed Layer Dynamics Experiment (MILDEX). *J. Geophys. Res.*, **94**, 4835-4842.

Pollard, R. T., 1980: Properties of near-inertial oscillations. *J. Phys. Oceanogr.*, **10**, 385-398.

----- and R. C. Millard, 1970: Comparison between observed and simulated wind generated inertial oscillations. *Deep Sea Res.*, **17**, 813-821.

Prandle, D. 1997. tidal and wind-driven surface currents from OSCR. *Oceanography,* **10**, 57-59.

Robinson, A. R. and S. M. Glenn, 1999: Adaptive sampling for ocean forecasting. Naval Research Reviews, **52**(2): 26-38.

Schmidt, R.O., 1986: Multiple emitter location and signal parameter estimation. *IEEE Trans. Antennas Propag*, **AP-34**, 276-280.

Schofield, O., T. Bergmann, W.P. Bissett, F. Grassle, D Haidvogel, J. Kohut, M. Moline and S. Glenn, 2001: The long term ecosystem observatory: an integrated coastal observatory. *IEEE J. Ocean. Engin*., **27**, 146-154.

Shay, L. K. and S. W. Chang, 1997: Free surface effects on the near-inertial ocean current response to a hurricane: a revisit. *J. Phys. Oceanogr.*, **27**, 23-39.

-----, S. W. Chang and R. L. Elsberry, 1990: Free surface effects on the near-inertial ocean current response to a hurricane. *J. Phys. Oceanogr.*, **20**, 1405-1424.

----- and R. L. Elsberry, 1987: Near-inertial ocean current response to hurricane Frederic. *J. Phys. Oceanogr.*, **17**, 1249-1269.

-----, H.C. Graber, D.B. Ross and R.D. Chapman, 1995: Mesoscale ocean surface current structure detected by hf radar. *J. Atmos. Ocean. Tech*, **12**, 881-900.

Shulman, I., C.R. Wu, J.K. Lewis, J.D. Paduan, L.K. Rosenfeld, S.R. Ramp, M.S. Cook, J.D. Kindle and D.S. Ko, 2000: Development of the high resolution, data assimilation numerical model of the Monterey Bay. In Estuarine and Coastal Modeling, Spaulding, M.L. and H. Lee Butler, eds., 980-994.

Smith, J. D. and C. E. Long, 1976: The effect of turning in the bottom boundary layer on continental shelf sediment transport. *Mémoires Société Royal des Sciences de Liége*, 6^{e} série, **X**, 369-396.

Song, Y. T., D. B. Haidvogel and S. M. Glenn, 2001: Effects of topographic variability on the formation of upwelling centers off New Jersey: a theoretical model. *J. Geophys. Res.*, **106**, 9223-9240.

Stewart, R.H. and J.W. Joy, 1974: Hf radio measurement of surface currents. *Deep-Sea Res.*, **21**, 1039-1049.

Svedrup, H. U., M. W. Johnson and R. H. Fleming, 1942: The oceans: their physics, chemistry, and general biology. Prentice-hall, 1087pp.

Teague, C.C., J.F. Vesecky and D.M. Fernandez, 1997: Hf radar instruments, past to present. *Oceanography*, **10**, 40-44.

Walford, L. A. and R. I. Wicklund, 1968: Monthly sea temperature structure from the Florida Keys to Cape Cod. American Geophysical Society. *Serial Atlas of the Marine Environment* Folio 15.

Wyatt, L.R., 1997: The ocean wave directional spectrum. *Oceanography,* **10**, 85-89.

Yankovski, A. E. and R. W. Garvine, 1998: Subinertial dynamics on the inner New Jersey shelf during the upwellinf season. *J. Phys. Oceanogr.*, **28**, 2444-2458.

Curriculum Vita

Joshua Todd Kohut

Education:

1997 B.S. with honors in Physics, College of Charleston, Charleston, South Carolina, USA (Cum Laude)
1997 Minor in Mathematics, College of Charleston, Charleston, South Carolina, USA

Employment:

1997-Pres Graduate Assistant, Rutgers University, New Brunswick, New Jersey

Professional Societies:

Member, American Geophysical Society

Publications:

Kohut, J.T., S.M. Glenn and D.E. Barrick, 1999. SeaSonde is integral to coastal flow model development. *Hydro International,* 3, 32-35.

Kohut, J.T., S.M. Glenn, and D. Barrick, 2000. Multiple HF-Radar system development for a regional Longterm Ecosystem Observatory in the New York Bight. *American Meteorological Society: Fifth Symposium on Integrated Observing Systems*, pp. 4-7.

Schofield, O., T. Bergmann, J. Kohut, S. Glenn, 2001. A coastal ocean observatory for studying nearshore coastal processes. *Backscatter,* 12, 34-37.

Schofield, O., T. Bergmann, J. Kohut, S.M. Glenn, W.S. Pegau, E. Boss, C. Davis, W. Snyder, J. Bowles, M. Kappus, B. Arnone, A. Weidemann, W. P. Bissett, M.A. Moline, E. L. Heine, J. Case and C. Herron. 2002. Adaptive sampling of a "red river" in the coastal waters using a coastal observatory, *EOS,* submitted.

Schofield, O., T. Bergmann, W.P. Bissett, F. Grassle, D. Haidvogel, J. Kohut, M. Moline and S. Glenn. 2002. Linking regional coastal observatories to provide the foundation for a national ocean observation network. *IEEE J. of Ocean. Eng*., 27(2), 146-154.

Kohut, J. T. and S. M. Glenn. 2002. Calibration of HF radar surface current measurements using measured antenna beam patterns. *J. Atmos. Ocean. Tech.*, Submitted.

Kohut, J. T., S. M. Glenn, D. E. Barrick. 2002. A multi-system HF radar array for the New Jersey Shelf Observing System (NJSOS). Oceanology International Meeting Proceedings. Submitted.